FREE FORMING OF LOCALLY INDUCTION HEATED SPECIMENS

A THESIS SUBMITTED TO
THE GRADUATE SCHOOL OF NATURAL AND APPLIED SCIENCES
OF
MIDDLE EAST TECHNICAL UNIVERSITY

BY

OYA OKMAN

IN PARTIAL FULFILLMENT OF THE REQUIREMENTS
FOR
THE DEGREE OF MASTER OF SCIENCE
IN
MECHANICAL ENGINEERING

MARCH 2005

Approval of the Graduate School of Natural and Applied Sciences

_____

Prof. Dr. Canan ÖZGEN
Director

I certify that this thesis satisfies all the requirements as a thesis for the degree of Master of Science.

_____

Prof. Dr. S. Kemal İDER
Head of Department

This is to certify that we have read this thesis and that in our opinion it is fully adequate, in scope and quality, as a thesis for the degree of Master of Science.

_____

Prof. Dr. A. Erman TEKKAYA
Supervisor

Examining Committee Members

Prof. Dr. S. Engin KILIÇ (ME, METU) _____

Prof. Dr. A. Erman TEKKAYA (ME, METU) _____

Prof. Dr. Zafer DURSUNKAYA (ME, METU) _____

Assoc. Prof. Dr. C. Hakan GÜR (METE, METU) _____

Asst. Prof. Dr. Suat KADIOĞLU (ME, METU) _____

I hereby declare that all information in this document has been obtained and presented in accordance with academic rules and ethical conduct. I also declare that, as required by these rules and conduct, I have fully cited and referenced all material and results that are not original to this work.

Oya OKMAN

ABSTRACT

FREE FORMING OF LOCALLY INDUCTION HEATED SPECIMENS

Okman, Oya
M.S., Department of Mechanical Engineering
Supervisor: Prof. Dr.-Ing. A. Erman Tekkaya

March 2005, 169 pages

Hot forming is highly utilized in manufacturing of complex shapes. Relatively low flow stresses of materials at elevated temperatures provide ease of manufacturing. On the other side, the current trend is to replace hot forming with cold forming due to the superior mechanical properties and higher dimensional accuracy of the products and less energy consumption. However, cold forming requires high tooling costs and forming loads. In this study, a new process is proposed for production of complex shaped products where the disadvantages of both of the alternatives are tried to be minimized. The basic idea is to control the mode of deformation by heating the specimen locally prior to forming. Electromagnetic induction is used for local heating. Numerical simulations are carried out by finite element method (FEM) for further investigation on the effect of parameters. Thermo-mechanical analysis of heat diffusion and upsetting is supported by electromagnetic analysis of induction heating. The failure modes and operational window of the novel process is established. Conclusions are drawn on the applicability of the process and the effect of process parameters on the efficiency.

Keywords: Metal Forming, Local Heating, Induction Heating, Finite Element Method.

ÖZ

İNDÜKSİYON İLE BÖLGESEL OLARAK ISITILAN PARÇALARIN ŞEKİLLENDİRİLMESİ

Okman, Oya
Yüksek Lisans, Makina Mühendisliği Bölümü
Tez Yöneticisi: Prof. Dr. A. Erman Tekkaya

Mart 2005, 169 sayfa

Sıcak şekillendirme işlemi, kompleks şekilli parçaların üretiminde sıklıkla kullanılmaktadır. Malzemenin yüksek sıcaklıklarda görece düşük akma gerilimlerine sahip olması, şekillendirmeyi kolaylaştırmaktadır. Bununla birlikte, soğuk şekillendirilmeyle üretilen parçaların üstün mekanik özellikleri ve işlemin düşük enerji gereksinimi, soğuk şekillendirmenin sıcak şekillendirme işlemlerinin yerini almaya başlamasına sebep olmaktadır. Öte yandan soğuk şekillendirme işlemleri yüksek maliyet ve yüksek şekillendirme kuvvetleri gerektirmektedir. Bu çalışmada, karmaşık şekilli parçaların üretimi için, soğuk ve sıcak şekillendirmenin olumsuz yönlerinin en aza indirildiği yeni bir işlem öngörülmektedir. İşlemin temel fikri, parçaların bölgesel olarak ısıtılarak şekillendirmenin kontrol altına alınmasıdır. Isıtmada elektromanyetik indükleme yöntemi kullanılmıştır. İşlem parametrelerinin etkilerinin analiz edilebilmesi için sonlu eleman yöntemi kullanılmıştır. Isıtma ve şekillendirme işlemlerinin termo-mekanik analizi indüksiyonla ısıtma işleminin elektromanyetik analizi ile desteklenmiştir. İşlemin uygulanabilirliği ve parametrelerin verimliliğe etkisi ile ilgili sonuçlara varılmıştır.

Anahtar Kelimeler: Metal Şekillendirme, Bölgesel Isıtma, İndükleme ile Isıtma, Sonlu Eleman Yöntemi

To My Family

ACKNOWLEDGEMENTS

I would like to express my deepest gratitude and appreciation to my supervisor Prof. Dr.-Ing. A . Erman Tekkaya, who inspired, encouraged and supported me for this study.

I would like to thank to my colleague Murat Özmen, for his support and help in this study and for being such a great friend.

I would like to thank my colleagues Ursula Weidig, Hansruedi Huwiler, Christian Schelle and Tiziano Minghetti for their great support and valuable contribution.

I would like to thank to Prof. Dr. Zafer Dursunkaya for his kind help, valuable ideas, which lead me to a different point of view, and for his great contribution.

The support provided by the RUAG Components for this research study is greatly acknowledged.

I would like to thank Ahmet Kurt, Kürşat Kayatürk and Ercenk Aktaş, who have helped and supported me with great patience.

I would like to thank to Prof. Dr. H. Bülent Ertan and Levent Burak Yalçıner for their suggestions and comments.

My best wishes to Femlab members Mete, Muhsin, Özgür, Bahadır, Nagihan, Çağrı, Erkan, Muin, Alper, Koray, Çağlar and my roommate Erge for their friendship.

To Behzat for enliving my life.

To my mum and dad whose love has always given me strength and confidence. To my brother Erman, for his love, patience and endless support. You are loved deeply.

TABLE OF CONTENTS

LIST OF TABLES

LIST OF FIGURES

CHAPTER 1

INTRODUCTION

1.1 An Overview of the Metal Forming Processes

Manufacturing processes are the set of actions carried out to produce solid bodies with the required geometry and properties. The classification of manufacturing processes according to DIN 8530 is given in Table 1.1 [1].

Table 1.1 Classification of manufacturing processes [1]

<table>
<tr><td>Creation of Cohesion</td><td>Maintenance of Cohesion</td><td>Destruction of Cohesion</td><td colspan="2">Increase of Cohesion</td></tr>
<tr><td rowspan="5">1. Primary Forming
(Form generation)</td><td colspan="3">Shape (Form) Modification</td><td rowspan="5">5. Coating</td></tr>
<tr><td>2. Deforming</td><td>3. Separating</td><td>4. Joining</td></tr>
<tr><td colspan="3">6. Changing Material Properties</td></tr>
<tr><td>Rearrangement of particles</td><td>Removal of particles</td><td>Addition of Particles</td></tr>
</table>

Metal forming, which is classified under “Deforming” processes in Table 1.1, is one of the main production processes. It is defined by DIN 8580 as “manufacturing of a shape while retaining its mass and material cohesion”. Processes of this kind are also classified as non-material removal processes. [2]

Metal forming processes provide various advantages to the manufacturer. In terms of efficient utilization of material, these processes have superior characteristics. They provide high productivity in short production times. The dimensional accuracy of the final product is high within certain tolerances. The mechanical properties of the product are good, especially under dynamic loading conditions [1]. Because of the advantages mentioned above, this manufacturing technique is commonly utilized in industry.

Metal forming processes can be classified regarding various criteria. One of those criteria is the starting temperature of the workpiece during the process. Regarding this criterion, the three main groups of processes are cold forming, warm forming and hot forming (Figure 1.1).

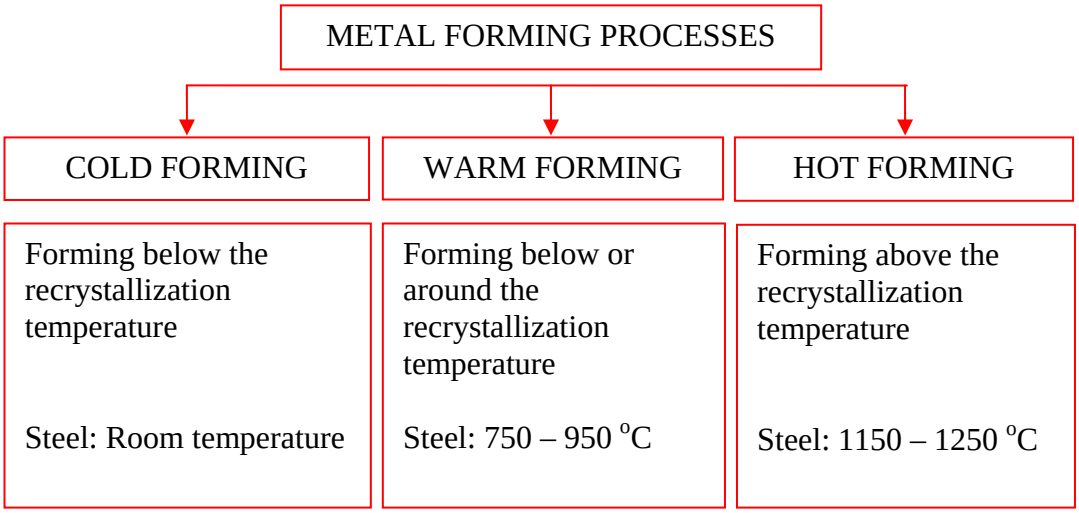

Figure 1.1 Classification of metal forming processes [1].

Hot forming is the forming of metal workpieces above their recrystallization temperature. At elevated temperatures, metals soften and become more ductile providing ease of manufacturing of large and complex shaped workpieces. Beside those favorable properties, hot forming process has some disadvantages. The dimensional tolerances are hard to control due to contraction of the workpiece after

cooling. Surface quality of the final product is not as good as in cold forming. Heat energy supplied increases the cost of the operation.

Cold forming is performed under recrystallization temperature of the workpiece. The tendency is to replace hot forming and some other alternative manufacturing processes with cold forming. The main advantages of the process are high strength of the products, better dimensional precision and surface finish and less waste of material. Near-net shape and net-shape products can be manufactured by this method. On the other side, cold forming processes require high forming loads and formability of the material is limited at low temperatures [1].

When forming is conducted around the recrystallization temperature of the workpiece, it is called warm forming. Warm forming is preferred to achieve a good balance between the required forces, ductility, formability and the final product properties. Better surface finish and strength can be obtained than that achieved from higher temperature operations. This process has become more feasible with the advancements in forming technology, since control of temperature and its distribution and choice of working temperature can be precisely followed [3].

1.2 Open Die Forging

Open die forging is a specialized type of forming processes, in which deformation of a workpiece is provided by means of tools which move toward each other and which conform to some level to the shape of the workpiece. According to DIN 8583, this specialized process is categorized as a type of “forming under compressive loads” [2].

The general aim is to achieve a desired mass distribution or shape before the successive operations. One of the main advantages is that simple tools are sufficient for the process [1].

Upsetting process is one of the most widely used open die forging processes (Figure 1.2). In this process, workpiece is clamped between flat die and formed under compressive forces. Mechanical and hydraulic presses are used in this process.

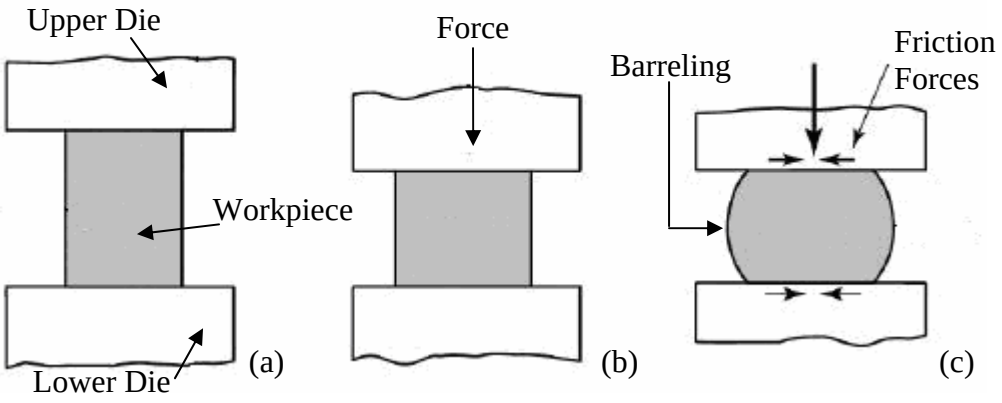

Figure 1.2 Schematic representation of the upsetting process [1].

Upsetting process will be investigated in this study. Low number of constraints imposed by the tool geometry makes the process suitable for investigation of effect local heating on the material flow under compressive loads. Also, it may be possible to utilize the process together with heating, in manufacturing of complex shapes, which are conventionally produced by closed die forming with high tooling costs.

1.3 Aim and Scope of the Study

Today, many components are being produced by either cold or hot working processes. Open die forging is preferred in manufacturing of simple, axisymmetric products. Either hot or cold forming is preferred regarding the nature of the workpiece material and the economical aspects of the process. As the complexity of the geometry of the final product increases, closed die forging is preferred and

range of the working temperatures decreases. Need for complicated tools increase the cost of the process.

Hot forming is usually employed in conventional metal forming applications due to high formability of materials at high temperatures. However, this process is usually not environmental friendly since utilization of soaking furnaces and graphite lubrication on workpieces pollutes air and water. Also, the heating costs are high. Due to this fact, today, there is a trend of switching from casting to metal forming and furthermore from hot forming to cold forming [4]. Local heating can also be a good alternative for reducing the energy consumption, leading to decreases in process costs and environmental pollution.

An innovative method has been proposed for manufacturing of complex shaped products by utilizing simpler tools. The process is visualized by a schematic representation in Figure 1.3. The idea is to control the flow of material during a simple open die forging process by increasing the temperature gradient locally on the regions, where local deformation is desired to take place.

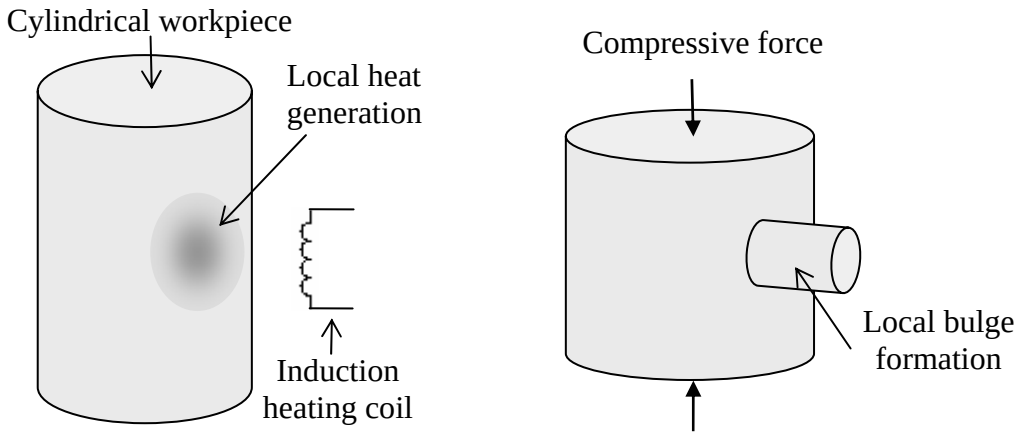

Figure 1.3 Schematic representation of free forming of locally heated specimens.

One of the main motives of the idea is that formability of the metals increase with increasing temperature. When compressive force is applied, the heated volume of

the workpiece will behave in a different way than the material in the cooler parts. The products produced in a process, in which local heating is followed by simple free forming, will not be axisymmetric. An appropriate temperature distribution within the workpiece before upsetting may result in desired complex shape of the process.

In this study, the applicability and effectiveness of the proposed process, namely “free forming of locally heated specimens” is investigated. The main parameters and their effects on the final shape and properties of the product are examined.

Induction heating is chosen as the heating method, because of its common utilization in industry. Cylindrical workpieces with hollow and solid geometries are selected. The parameters to be investigated throughout the study are as follows:

- Heating parameters (Energy supplied in induction heating, frequency of heating, etc.)
- Geometry of the workpieces (Outer diameter and wall thickness of the cylindrical specimens)
- Material of the workpiece

In the first part of the investigation, experiments are designed and conducted. The experimental procedure is summarized in Figure 1.4. The steps followed throughout the experiments can be given as such:

- Cylindrical workpieces are clamped between the flat dies.
- Induction heating coil is placed at a certain distance from the workpiece.
- Induction heating unit is turned on and workpiece is heated for a certain time. Temperature data on a specific point in the surface is recorded.
- Induction heating is terminated and coil is removed manually.
- Workpiece is free formed in the hydraulic press.
- After forming is completed, workpiece is taken away and cooled.

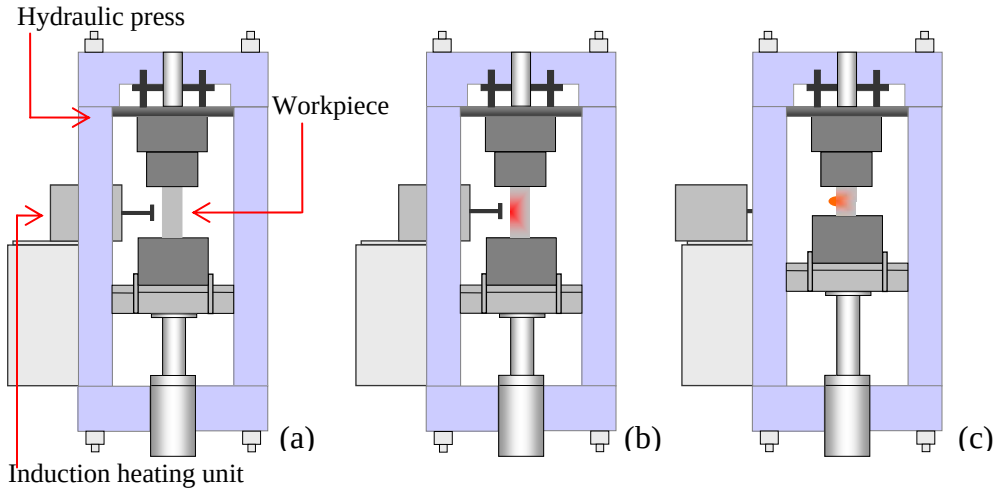

Figure 1.4 Schematic representations of the process steps: Positioning of the workpiece (a), induction heating (b), free forming (c).

The second part of the study consists of further analysis of the nature of the process by utilizing finite element analysis (FEA). MSC.SuperForm is used as software. The limits of the process are examined and conclusions on the applicability and effectiveness of the process are presented.

1.4 Content of the Thesis Report

This thesis report consists of nine chapters. The overview of the process and aim of the study is presented in the first chapter. Second chapter consists of previous studies on the subject. Some theoretical background of induction heating is given in the third chapter. In Chapter Four a general overview of the nonlinear finite element analysis is given. The first part of investigation, which consists of the experimental studies, is explained in the fifth chapter. The observations and results are included in this section. A further analysis of the experimental specimens is presented in Chapter Six, in the “Metallurgical Investigation” section. The second part of the study, namely, numerical analysis of the process, is explained in detail in Chapters Seven and Eight. Chapter Seven is dedicated to numerical analysis of induction heating since it is a quite detailed procedure. The comments and results

of numerical simulation of forming are presented separately in the eighth chapter. The discussions, conclusions and further recommendations are given in the last chapter of the thesis report.

CHAPTER 2

LITERATURE SURVEY

2.1 Introduction

In this chapter, the theoretical aspects of the induction heating are explained. Some studies on forming of locally heated workpieces are presented. Some applications of this study are shown and their results are mentioned.

2.2 Utilization of Induction Heating in Industry

Induction heating is a widely used heating method in industry. The environmental issues constitute a reason for utilizing induction heating. Conventional heating apparatus such as burner heating furnaces require more energy than the induction heating equipment. Employing induction heating systems in hot-forging plants therefore reduces air and water pollution [4].

Induction heating is used in heating thin strips of sheets, which proceed with constant velocity in the production lines. The special name *Transverse Flux Induction Heating* (TFH) is used for this kind of processes. This method has taken place of the conventional methods like gas-fired or electrical resistance heating techniques, especially in automotive industry. It can be used with great flexibility and efficiency in both ferrous and non-ferrous materials [5].

In induction heating process, the heat generation in the workpiece is concentrated near the surface area. The resulting high temperature gradient between the surface and the inner portions provides surface hardening. High frequency induction heating is used extensively in hardfacing applications. The complex thermal strains and phase transformation lead to residual stresses. The microstructure near the surface area can be controlled by proper heating applications [6].

2.3 Utilization of Local Heating in Metal Forming Applications

Local heating is utilized in metal forming applications, where high formability is required. A new process suggested for deep drawing of Magnesium alloys [7]. In spite of its desirable physical properties, magnesium alloys are less formable. The new process idea is to heat the workpiece flange locally, where large deformation takes place during forming (Figure 2.1). On the other side, strength of the workpiece is increased by cooling the drawn cup locally, in order to prevent the cracks at the die shoulder part [7].

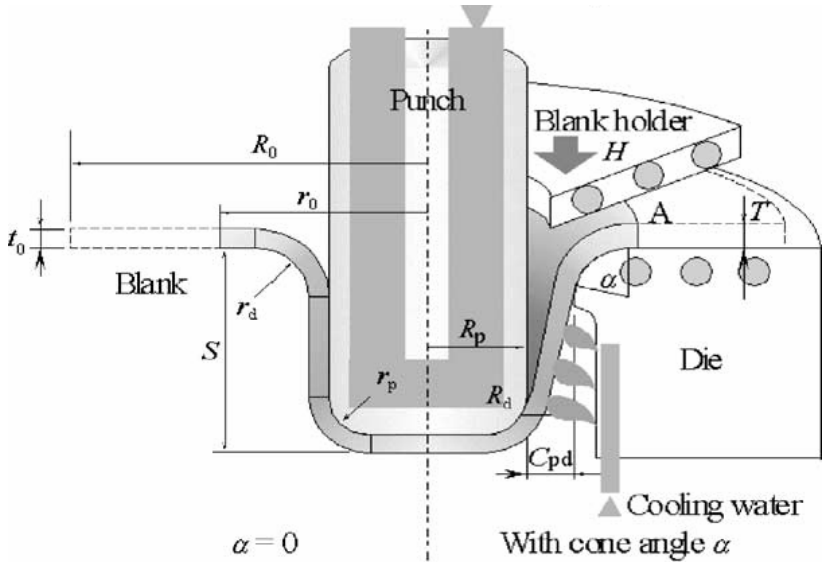

Figure 2.1 Local heating of the flange during deep drawing [7].

Recently, new processes are being proposed, where the effects of local heating replace the conventional tools in some metal forming operations. Bending of plates by laser line heating is an example of those procedures [8]. In this thermo-mechanical forming technique, plastic deformation is realized by local heating of a metal plate by moving the laser beam on an appropriate path and then cooling it (Figure 2.2). When one side of the plate is heated fast, the high temperature gradient between the upper and the lower surface generates different expansion across the thickness of the plate. As a result the plate is bended. Due to high temperature on the area just below the heat source, flow stress is decreases on that portion, resulting in plastic deformation.

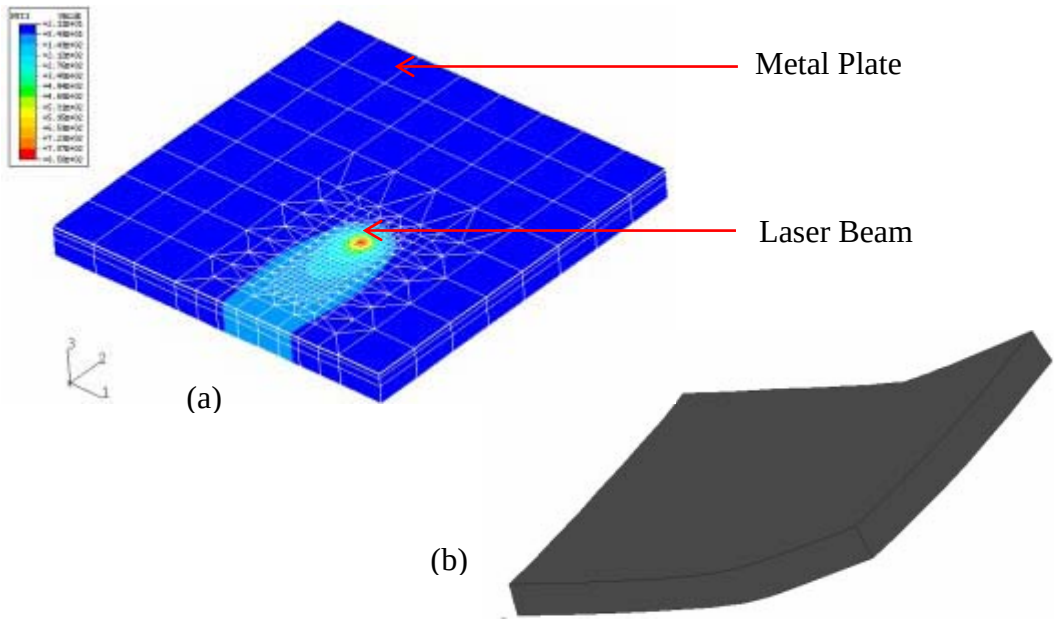

Figure 2.2 (a) Numerical simulation model of laser heating of the metal plate. (b) The deformed geometry of the plate due to line heating [8].

Local induction heating is utilized in bending of pipes [9]. The schematic representation of the process is shown in Figure 2.3. The bending is realized with proper application of local heating and cooling of the pipe. This is an advanced process, which is used in bending of pipes with small bending radius and large

diameter. It is used in many fields such as power transportation and chemical industries since it requires lower costs and high quality products.

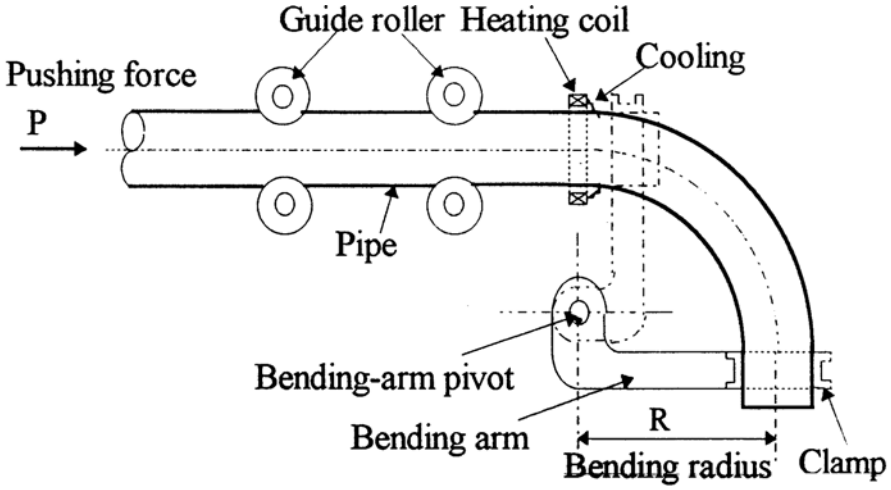

Figure 2.3 Utilization of local heating in bending of pipes [9].

2.4 Utilization of Local Heating in Forging

The idea of utilizing cold and hot forging simultaneously in a single forming step has been previously proposed for processes, where local deformation of the workpiece is desired. The aim is to discard the disadvantages of cold forming, such as high forming forces, necessity of complicated tools and high number of deformation step and at the same time avoiding the difficulties in hot forming, such as scaling, poor surface quality and necessity for high heating energy.

A typical example of utilization of local heating in metal forming applications is electro-upsetting [1]. The schematic representation of the process steps is seen in Figure 2.4.

In electro-upsetting process, a cylindrical rod is fed between an anvil and a guiding electrode by means of a punch (Figure 2.4(a)). The part of the material that lies between the two electrodes is heated by applying electric current. The temperature

of this part of the material increases. Formability of the heated section of the rod becomes higher than the cooler regions. Therefore, deformation is localized in the heated part of the cylindrical rod. The diameter increase of the heated portion is seen in Figure 2.4(b). The cooler section of the rod is transferred to the gap between the electrodes without experiencing a buckling problem. As seen in Figure 2.4(c), the diameter of the rod between the electrodes is enlarged, whereas the rest of the rod does not deform. In this application, buckling problem that usually occurs during height reduction of workpieces with high length to diameter ratios is discarded. Larger diameter workpieces can be produced efficiently by electro upsetting method.

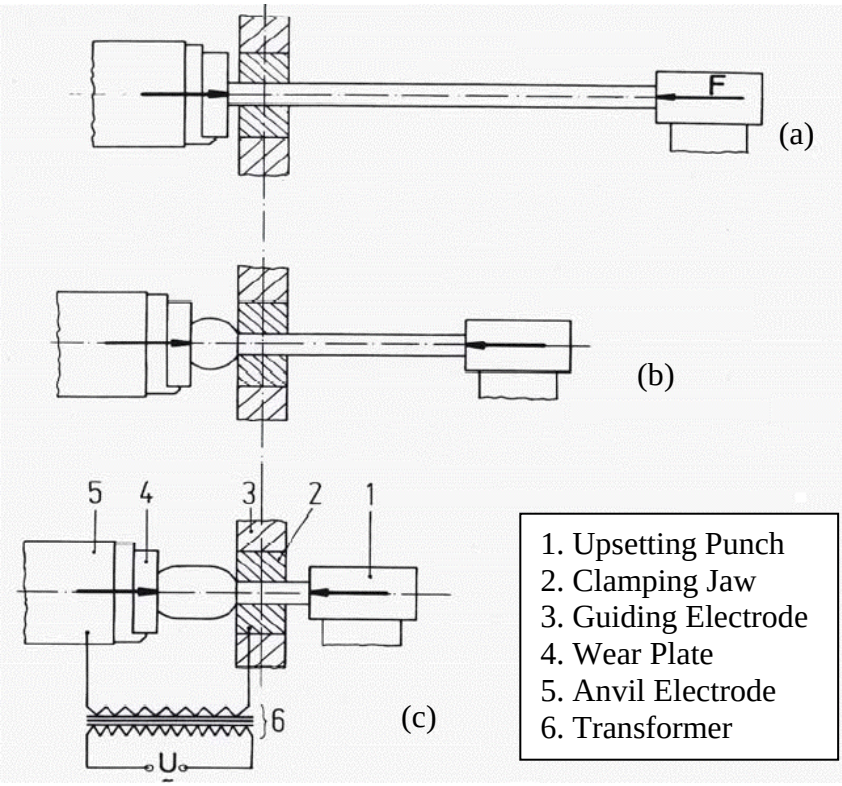

Figure 2.4 Schematic representation of electro-upsetting [1].

Previous studies on this subject have shown that variation of yield stress within the material affects the mode of deformation of the workpiece. Some complex shapes can be manufactured by simple upsetting method, in place of successive forging operations or closed die forming [10].

Local heating is suggested to provide yield stress variation within the specimen. Induction heating is used. Small cylinders with 25 mm diameter and 12.7 mm height are assembled together to form a billet of 38.1 mm height. The cylinder in the middle is heated above 900^{o}C in a muffle furnace before the deformation takes place. At the end of upsetting process an axisymmetric shape is obtained with a local bulge in the middle. Deformation takes place where flow stress is lower due to high temperature. Similar results are obtained when solid cylinders are heated locally by induction heating (Figure 2.5). Deformation was largest at the heated section [10].

Figure 2.5 Part is heated locally by induction and formed by upsetting [10].

Oxyacetylene burner is employed to provide direct localized heating on a small portion on the workpiece [10]. Cylindrical specimens that are deformed in simple upsetting process provided shapes with local bulges (Figure 2.6(a)).

Localized heating of more than one section of the surface can be simulated by using compound billets. Variation of yield stress is provided by using two different materials within the workpiece volume [10]. Cylindrical workpieces made of aluminium are drilled perpendicular to the centerline (Figure 2.6(b)). The holes are filled with plasticine, which simulates the softening of the material. Local deformation is observed in the end of simple upsetting process. Those studies have shown that with the application of fast, local heating, various profiles could be produced quickly with simple tools [10].


(a)
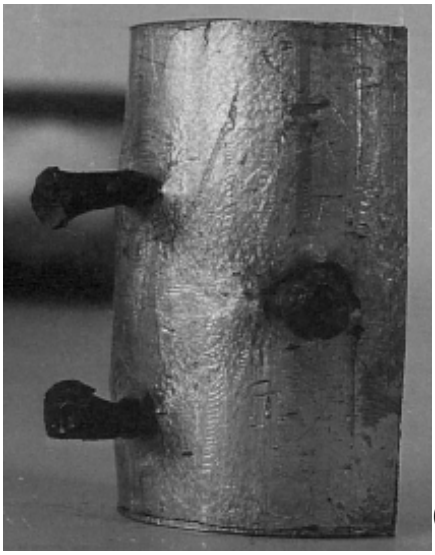
(b)

Figure 2.6 (a) Local heated and free formed workpiece. (b) Local heating of the workpiece is simulated by filling the drilled holes with plasticine [10].

Local induction heating is utilized in production of axisymmetric geometries [11, 12]. In place of heating the whole volume of the workpiece, only the region, where most of the deformation takes place, is heated by means of an induction coil (Figure 2.7). Hollow and solid products are produced effectively by this method, in case sufficient punch load, heat energy is supplied and appropriate workpiece dimensions are selected.

The process of induction heating and upsetting is simulated by means of finite element method (Figure 2.8). Successful results can be obtained by carrying out a coupled thermo-mechanical analysis [11, 12]. In the first step of the analysis, temperature distribution at the end of the heating stage is obtained. A high value of temperature is assigned as an initial condition to the nodes in heated region and heat conduction in a certain time interval is simulated. The temperatures at the nodes are calculated. This stage provides a smooth temperature gradient on the heated volume. The calculated temperature values are compared with experimental data at some points. Afterwards, upsetting is simulated and final shape of the workpiece is obtained. The results of the numerical simulations have shown good correspondence with the experimental results.

(a)

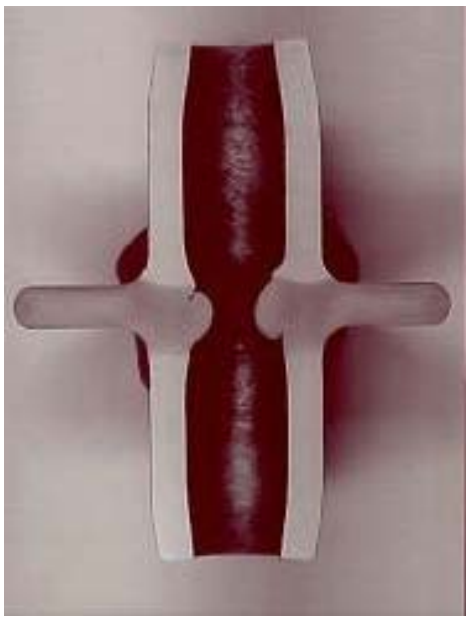

(b)

Figure 2.7 (a) Heating of the workpiece by means of induction coil. Symmetry of heating is provided by rotation of the workpiece. (b) The cross sectional view of a cut hollow specimen after upsetting [11, 12].

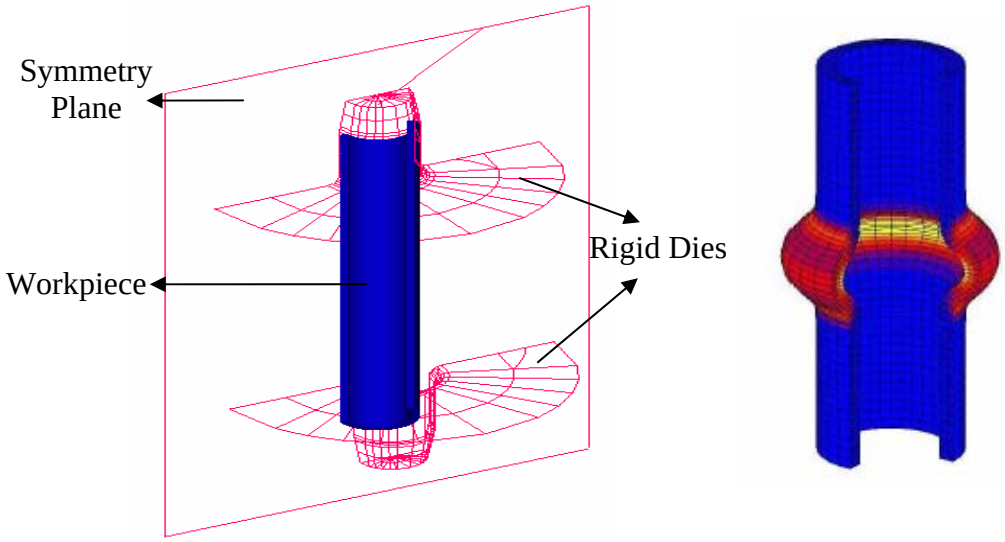

Figure 2.8 Numerical modeling of upsetting of locally heated specimens [11, 12].

CHAPTER 3

THEORY OF INDUCTION HEATING

3.1 Introduction

In this chapter, the theoretical aspects of the induction heating are explained. The physics of the process and the some process parameters, which have crucial importance in local heating, are investigated.

3.2 The Mechanism of Induction Heating

Induction heating is a method of generating heat energy in a specimen by inducing eddy currents and hysteresis loses in that specimen due to an external alternating magnetic field. The field is established by means of coils that are placed around the specimen or held parallel to it [13].

An alternating voltage is applied to an induction coil, which will result in development of an alternating current within the coil. A time variable magnetic field is induced in the surroundings and this field has the same frequency with the current [14]. In a changing electromagnetic field, an electromagnetic force is induced in any conductive material. If current flow is allowed along a complete path within the material, the induced force produces a current along this path. Due to the resistance of the material *Joule Effect* is observed; in other words, heat is generated proportional to I^2R, where I is the magnitude of current and R is the

resistance of material [13]. For steady current, resistance of a piece of homogeneous material that has a uniform cross section is defined as

$$R = \frac{\rho l}{A} \tag{3.1}$$

where, ρ is resistivity, l is the length of the material along the direction of current and A is the cross sectional area normal to the current flow [15]. Induction heating is based on development of the Joule effect on the materials in the close neighborhood of the coil. The schematic representation of heat generation in a specimen that is placed in a magnetic field is shown in Figure 3.1.

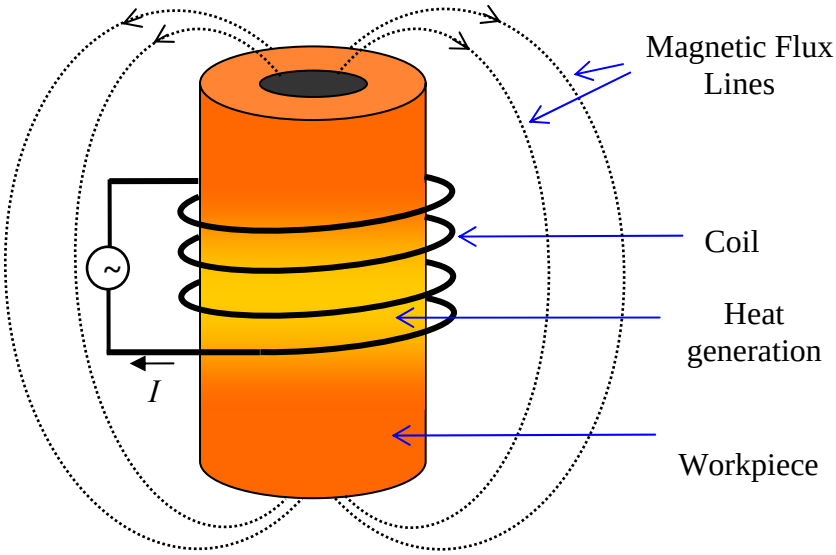

Figure 3.1 Heat generation on a workpiece due to the magnetic field created around a current carrying coil.

3.3 Electromagnetic Properties of Metals

All of the materials in nature show magnetic behavior. Some materials, which show considerably weak magnetic effects, are often considered as nonmagnetic. However, a vacuum is the only nonmagnetic medium. There are various quantities

by which the magnetic characteristics of the materials are explained. However, only the relative permeability (μ_r) and electrical resistivity (ρ) will be discussed in this report, since they are the most critical quantities.

3.3.1 Relative Permeability

Magnetic permeability is one of the most important characteristics of a material when its magnetic properties are considered. It expresses the relative decrease or increase in the resultant magnetic field inside a material compared to the magnetic field around the material. It is also defined as the ratio of the magnetic flux density inside the material to the strength of the magnetic field strength. The definition of relative permeability is given by Eq. 3.2.

$$\mu = \frac{\mathbf{B}}{\mathbf{H}} \tag{3.2}$$

where μ is magnetic permeability in Henry per m (H/m), $\mathbf{B}$ is magnetic flux density in Tesla (T) and **H** is magnetic field strength in Amperes per meter (A/m) [15]. It is more convenient to speak of the ratio of permeability of a material (μ) to the permeability to that of vacuum (μ_0). This ratio is defined as *relative permeability* and is given as

$$\mu_r = \frac{\mu}{\mu_0} \tag{3.3}$$

where μ_r is relative permeability of the material and μ_0 is permeability of vacuum and the value of μ_0 is $4\pi \times 10^{-7}$ H.m^{-1} [15].

The materials are divided into three groups regarding their magnetization ability; namely, paramagnetic, diamagnetic and ferromagnetic. Paramagnetic materials have a relative permeability value slightly greater than 1, whereas for diamagnetic

materials, this value is slightly less than 1. When induction heating is considered those materials are simply called nonmagnetic materials. Copper, aluminum, titanium and tungsten are some examples of this type. On the other side, ferromagnetic materials have high μ_r values. Iron, cobalt and nickel are some examples, which exhibit ferromagnetic behavior at room temperature [14]. The relative permeability values of some selected materials of different types are given in Table 3.1.

Table 3.1 Relative permeability values of some selected materials [16].

Substance	**Type**	**Relative Permeability**
Bismuth	Diamagnetic	0.99983
Air	Paramagnetic	1.0000004
Aluminum	Paramagnetic	1.00002
Ferroxcube 3 (Mn-Zn-ferrite powder)	Ferrimagnetic	1500
Mild Steel (0.2 C)	Ferromagnetic	2000
Iron (0.2 impurity)	Ferromagnetic	5000
Purified iron (0.05 impurity)	Ferromagnetic	200000

Relative permeability values of different materials show different characteristics. The relative permeability of diamagnetic and paramagnetic substances does not vary in the existence of an external magnetic field. On the other side, the relative permeability of the ferromagnetic materials shows considerable variations for different applied magnetic fields. Maximum may occur at different values of applied field for different materials [16]. For magnetic steels that are frequently used in induction heating, the relative permeability can vary from small values (2 or 3) up to more than 500, depending on the temperature and magnetic field intensity. An example of the variation of relative permeability with respect to the magnetic field is given in Figure 3.2. The magnetic permeability of the specimen in three different values of magnetic field strength, H_1, H_2 and H_3, is presented. As seen in Figure 3.2, the relative magnetic permeability decreases as the temperature

is increased. The decreasing trend becomes more pronounce at temperatures above 500°C. At about 750°C the value of μ_r becomes zero. This temperature value is called the *Curie Point,* at which ferromagnetic materials become nonmagnetic [14].

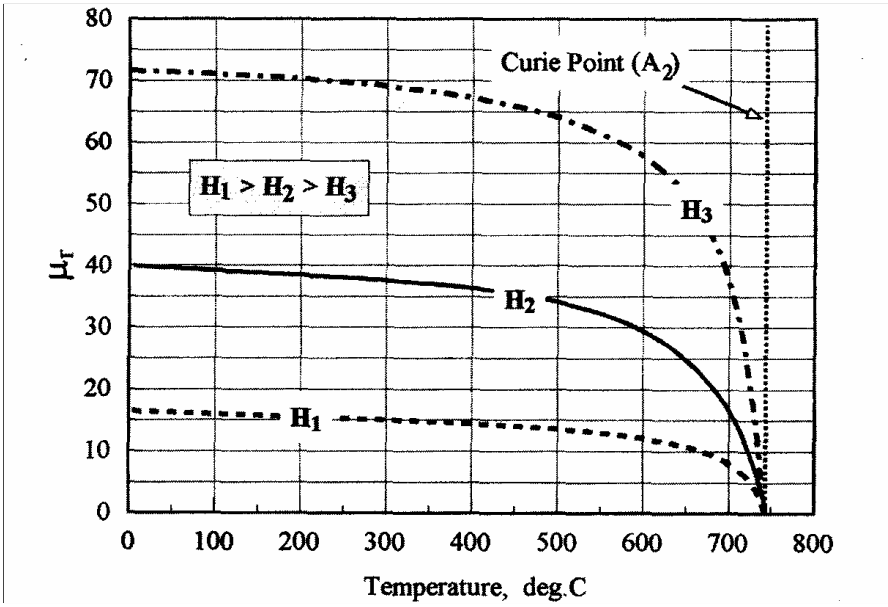

Figure 3.2 Effect of temperature and field intensity on relative permeability of medium carbon steel [14].

The B-H curve, which is also called the magnetization curve, is usually non-linear. The maximum value of μ_r is obtained at a specific value of magnetic field, H_{cr}. Magnetic permeability increases with H when $H<H_{cr}$ and decreases when $H> H_{cr}$.

During induction heating, the magnetic field intensity varies within the workpiece. Like the current distribution, H also decreases exponentially as going from the surface to the core. This fact results in a variation of μ_r within the workpiece. In applications, where the magnetic field intensity is greater than H_{cr} on the surface of the workpiece, relative permeability increases until it reaches its maximum inside the workpiece and then to decrease [14].

3.3.2 Electrical Resistivity

Electrical resistivity defined as “a measure of materials resistance to the passage of electric current” [17]. It is the reciprocal of *electrical conductivity*, in Siemens per meter (S/m).

Electrical resistivity plays a critical role in induction heating. The amount of heat generation is directly proportional to the electrical resistivity, due to the Joule Effect. The distribution of current and heat within the workpiece is also dependent on this quantity. The effects of electrical resistivity on induction heating process will be discussed further in this chapter.

3.4 Electromagnetic Effects

3.4.1 Skin Effect

When direct current flows through a workpiece, the current distribution on the cross section will be uniform. However in case of application of alternating current, the distribution of current within the workpiece is strongly dependent on the frequency. The current tends to flow on the outer surface of the specimen. This phenomenon is known as the *skin effect* [14]. The skin effect is schematically shown in Figure 3.3. In induction heating, eddy currents at a certain frequency are produced within the workpiece. Due to the skin effect, the eddy current distribution will be non uniform. This distribution has a critical role on the temperature distribution. Considering the fact that the aim of the process may either be through heating or local heating, it is clear that the skin effect has an important role in effectiveness of the process.

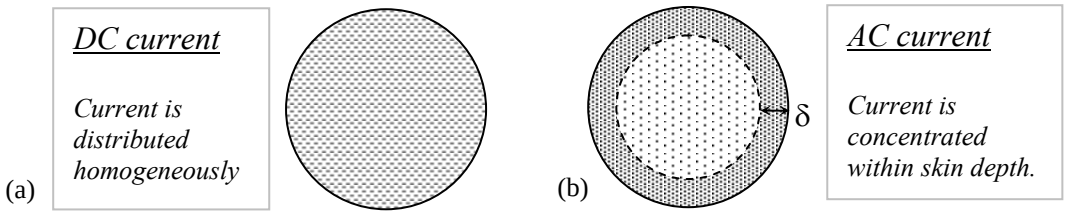

Figure 3.3 Illustration of skin effect.

The current distribution decreases exponentially from the outer surface to the core of the conductor. 86% percent of the total generated power is concentrated on a certain depth from the surface, which is defined as the *skin (penetration) depth (δ)*. It is the distance from the surface of the conductor to its core, in which the current and the power density drop to "1/*e*" and "1/e^2" of their surface values, respectively [14]. Skin depth is formulated as follows [15]:

$$\delta = \sqrt{\frac{\rho}{\pi f \mu_r \mu_0}} \tag{3.4}$$

where *f* is the frequency of the current. As clearly seen in Eq. (3.4), the skin depth is dependent on some material properties such as electrical resistivity and relative permeability as well as a process parameter, frequency. In high frequency applications or heating of large diameter workpieces the skin effect becomes much more critical. The heat generation is limited to a narrow volume near the surface.

The skin depth is strongly dependent on temperature. During heating, skin depth may increase significantly due to increase of resistivity. Therefore, during induction heating applications, it may be hard to implement the skin depth equation to the actual state. Due to the variation of temperature within the workpiece, the relative magnetic permeability will show considerable variations in the workpiece at a specific instant. Theoretically, different skin depth values can be calculated for a workpiece. However, in engineering applications, the value of μ_r at the surface on the specimen is used in determination of skin depth [14].

Skin depth varies drastically in induction heating applications. In the first stages of heating the depth of penetration increases both due to the increase of resistivity and decrease of relative permeability. When the Curie point is reached, the relative magnetic permeability drops suddenly to unity, resulting in a sudden jump in skin depth. In case of further heating, the skin depth will rise slightly due to increase of electrical resistivity (Figure 3.4).

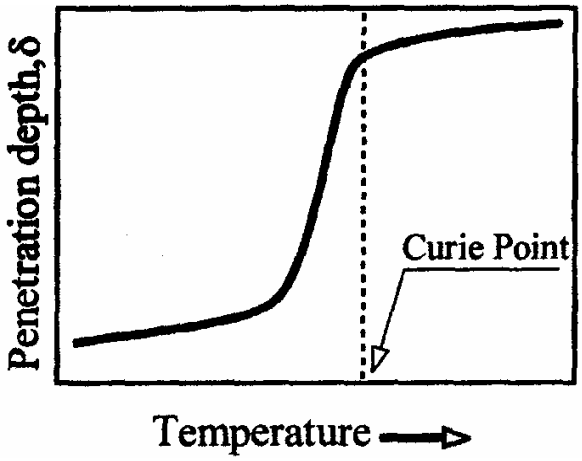

Figure 3.4 Typical variation of skin depth during induction heating of a carbon steel workpiece [14].

In literature, it is generally assumed that the distribution of current along the radius of the workpiece is exponentially decreasing, which is also stated previously in this study. However, in reality this assumption is valid only for nonmagnetic homogeneous specimens with constant electrical resistivity. Eq. (3.4) cannot be used in many cases, since in majority of induction heating applications high thermal gradients are present (in surface hardening, etc.). Electrical resistivity and relative permeability varies considerably with temperature. Beside the temperature distribution, the non uniform distribution of magnetic field intensity also causes variation of μ_r. In those complicated applications, the current distribution shows a wave-shaped form along the radius [14].

3.4.2 Magnetic Proximity Effect

The previous discussions on the distribution of current in conductors are developed on the assumption that there are no other disturbing magnetic fields in the surrounding. However, this is usually not the case in reality.

When two current carrying conductors are placed next to each other, the current in each of them will redistribute. If the currents in the bodies flow in opposite directions then the current in each conductor will be concentrated on the surface facing to the other body. If the current flows are in the same direction, then the current will concentrate on the opposite sides of the conductors.

The resulting magnetic field will also be affected by the presence of a second conductor. In case of current flows in opposite directions, magnetic field intensity in the gap between the two conductors will increase. However, the field intensity on the area surrounding both of the conductors will decrease. If the current flows are in the same direction, then the field intensity in the gap will be decreased whereas it will be increased in the surrounding area.

In induction heating process, eddy currents in the workpiece create also a magnetic field in the opposite direction to that of the coil. The distance between the induction coil and the conductor has a great importance in effectiveness of induction heating. When the conductor and the workpiece are held together with a small gap in between, the localization of the eddy currents induced in the workpiece will be highly effected by the coil current. They will be localized in a narrow volume just opposite to the coil. There will be an intense heat generation on a narrow volume within the workpiece extending below the surface area. If the distance between the two bodies is increased, the strength of the proximity effect will decrease. Eddy current distribution will be more even on a wider area on the surface of the workpiece. The depth of heat generation will decrease [14].

3.4.3 Electromagnetic Ring Effect

The distribution of current on the coil cross section is effected by the geometry of the coil. If the current carrying straight bar is bended into a ring, then the magnetic field lines inside of the ring will be intensified whereas the flux lines in the surrounding area will be disseminated. This fact causes the current to be concentrated on the inside surface of the ring shaped coil. In induction heating applications, where the workpiece is surrounded by the induction coil, electromagnetic ring effect increases the efficiency of the process [14].

3.5 Mathematical Modeling of the Electromagnetic Field

The fundamental principle of induction heating relies on transportation of energy by means of waves that are produced due to presence of a time varying electromagnetic field. A changing magnetic field produces an electric field or vice versa. Before proceeding into presentation of equations for time varying fields some fundamental definitions of the electrostatic model are given.

For a linear and isotropic media, the following relation is valid between the electric field (**E)** and the electric field (**D)**, where ϵ is the absolute permittivity of the medium and measured in farads per meter (F/m).

$$\mathbf{D} = \epsilon\, \mathbf{E} \tag{3.5}$$

The relationship between the magnetic flux density and the magnetic field intensity is described by the formula, where μ is the absolute magnetic permeability of the material.

$$\mathbf{B} = \mu \mathbf{H} \tag{3.6}$$

Within a conducting material, the conduction of currents is a result of the drift motion of charge carriers due to the presence of an electric field. This phenomenon is formulized by the *Ohm's Law,* given below.

$$\mathbf{J} = \frac{1}{\rho}\mathbf{E} \tag{3.7}$$

In this formula, **J** represents the volume current density, **E** is the electric field and ρ is the electrical resistivity of the material. Under time varying conditions, an electromagnetic model should be constructed, which relates the magnetic field vectors **B** and **H** to the electric field vectors **E** and **D**. The set of equations used to describe the electromagnetic field are called the *Maxwell's Equations*.

$$\nabla \times \mathbf{E} = -\frac{\partial \mathbf{B}}{\partial t} \tag{3.8}$$

$$\nabla \times \mathbf{H} = \mathbf{J} + \frac{\partial \mathbf{D}}{\partial t} \tag{3.9}$$

$$\nabla \times \mathbf{D} = \rho_v \tag{3.10}$$

$$\nabla \cdot \mathbf{B} = 0 \tag{3.11}$$

Eq. (3.8) is known as the *Faraday's law* and is accepted as the fundamental postulate of electromagnetic induction. It is the quantative representation of the experimental observation that magnetic flux change in a medium will result in induction of current in a conducting loop that is linked to it. The physical interpretation of Eq. (3.9) is that whenever there is a time varying electric field in a medium a magnetic field is induced, even in the absence of free current flow. The Eq (3.10) is the divergence relation between the electric field and the distribution of free charges in a medium. It is a fundamental governing equation for electrostatics in any medium. The symbol ρ_v denotes the volume density of free charges [15].

CHAPTER 4

REVIEW OF NONLINEAR FINITE ELEMENT ANALYSIS

4.1 Introduction

In solution of complex engineering problems, application of the conventional analytical methods may be impossible or impractical. The engineering approach in these cases is to approximate the solution of the problem by replacing the continuum with an appropriate model with finite degrees of freedom (DOF). This is the main motive of the finite element analysis. By this method, the exact solution can be approximated with acceptable degree of inaccuracy and in a reasonable time.

The process of local heating and upsetting is analyzed by using finite element method. The commercial software MARC SuperForm2002r2 is used for the thermo-mechanical simulation of the process. For simulation of induction heating, electromagnetic calculations are carried out by using ANSYS 7.0. In this section, a general review of the nonlinear finite element method (FEM) is presented.

4.2 The Basic Procedure of FEM in Solid Mechanics

The analysis procedure should start with a detailed identification of the physics of the problem; i.e. determination of the constraints, the quantity of interest and the necessity of FEM. The general procedure is composed of seven main steps [18].

Idealization: The continuum is divided into finite number of *elements*, which can be described as the parts of the actual structure and capable of reflecting the local response of the system to an excitation.

Discretization: The infinite number of unknowns (DOF) is reduced to a finite number in this step.

Determination of the Stiffness: In this step, the response of the elements to an excitation is determined. In solid mechanics, the relationship between unknown displacements and the known loads is established and it is indicated by Eq. (4.1).

$$\{f\} = [k].\{u\} \tag{4.1}$$

where, $\{f\}$ is the *load vector*, $\{u\}$ is the *displacement vector* and $[k]$ is the *element stiffness matrix*.

Assembly of the Element Stiffness to Discretize the Whole Continuum: The assembly process is realized by formulation of the conditions of compatibility. The first condition is the equality of the nodal displacements of the coinciding nodes. It is a necessary condition to satisfy the continuity within a solid body. The second condition is the equilibrium of nodal forces that act at a single node. Application of these two conditions to the system nodes ends up with a set of equations for the whole system, which is expressed as

$$[K].\{u\} = \{F\} \tag{4.2}$$

Where, $[K]$ is the *overall* or *global* system stiffness matrix.

Introducing Boundary Conditions: In this step, the known constraints on the nodes are introduced. External forces and displacements are inserted to Eq. (4.2).

Solution of the System Equations: The unknown quantities (displacement in Eq (4.2)) are determined by using standard methods like Gauss elimination, etc.

Computation of the Dependent Variables: The quantities defined for the problem are solved. In solid mechanics, they are the stresses and strains.

4.3 Finite Element Approach for Large Plastic Deformation

The metal forming applications require solution of complicated problems with large displacement, plastic deformation and friction. In this kind of applications, solution is usually nonlinear. In solid mechanics, the nonlinearity in finite element analysis can simply be defined as the dependence of the stiffness matrix to displacement and/or force. There may be three main reasons of nonlinearity.

Geometric nonlinearity may be observed in various situations. Large rotation and displacement of the system with small strains causes geometric nonlinearity. The distribution or magnitude of the applied forces may also be altered as a result of shape changes. Nonlinearity may also be observed in case of relatively small displacements, where the displacements exceed the dimension of the deforming body as in the case of thin sheet metals [19].

Material Nonlinearity is describes as the nonlinear relationship between the strains and stresses. Among many possible causes, it is observed in metal forming applications when the material starts to flow plastically under the applied loads. Some hyper elastic materials may exhibit nonlinear behavior in the elastic region.

Contact Nonlinearity is observed when the portions of the deforming body come gradually in contact with the tools, during the process. Also, friction may be a cause of contact nonlinearity.

Two main approaches are available in the solution of these problems, namely the elastic-plastic and the rigid-plastic procedures [20].

In the elastic-plastic approach, the elastic deformations on the material are included in the solution. In the rigid-plastic approach, the effects of elasticity are not included. It is widely used in applications, in which plastic deformation occurs and the elastic strains are not considered. The computation time decreases since the formulation does not require consideration of elastic strains. Furthermore the computer implementation is simple and the numerical solution is robust and reliable. Besides the advantages, the rigid plastic formulation, have some disadvantages. Physical behaviors that depend on elasticity, such as spring back or residual stresses, cannot be observed in the solution. The exact final shape and characteristics of the specimen may not fulfill the accuracy requirements. Furthermore, the regions that deform within the elastic range are regarded as rigid and this may lead incorrect results.

In the study, the deformation is localized in some portions of the workpiece. Therefore, it is highly probable that some regions on the specimen deform within the elastic range. In order to reflect the characteristics of the process accurately, the elastic-plastic approach is used.

4.4 Types of Formulation Regarding the Coordinate Frame

There are two main types of formulations to define the kinematics of deformation, namely the Eulerian and the Lagrangian approaches. In the Eulerian approach, the coordinate frame is fixed in space. The material flows through the mesh. It is suitable in cases, where the process is steady state. In Lagrangian approach, the mesh is considered to be attached to the body and displaces in space with the material [19]. The Lagrangian formulation is appropriate for the study.

The Lagrangian formulation is grouped into two types, namely, the total Lagrangian and the updated Lagrangian method. In the total Lagrangian approach the initial state of the body serves as a reference state, whereas in the updated Lagrangian approach the reference state is altered considering the current configuration. The updated Lagrange procedure is applicable to problems of plastic deformation with large strains. Therefore, the updated Lagrange procedure is used in analysis of upsetting.

4.4.1 The Updated Lagrangian Approach

The Lagrangian approach is used in applications, in which the initial coordinate frame has a little physical significance due to the nature of the problem because in an increment the reference frame is redefined in each iteration [20].

In the updated Lagrangian approach, the principal of virtual work is used to define the equilibrium condition.

$$\int_{V_0} S_{ij}\delta E_{ij}dV = \int_{V_0} b_i^0 \delta\eta_i dV + \int_{A_0} t_i^0 \delta\eta_i dA \qquad (4.3)$$

where S_{ij}: Second Piola-Kirchhoff stress tensor

E_{ij} : Green-Lagrange strain tensor

b_i^0 : Body force in the reference configuration

t_i^0 : Traction vector in the reference configuration

η_i : Virtual displacements.

The second Piola-Kirchhoff stress tensor (S_{ij}) is expressed by the relation [21]:

$$\mathbf{S}=J\mathbf{F}^{-1}.\boldsymbol{\sigma}.\mathbf{F}^{-T} \quad \text{or} \quad S_{ij}=JF_{ik}^{-1}.\sigma_{kl}.F_{lj}^{-T} \qquad (4.4)$$

The Green-Lagrange strain tensor is defined by [4]

$$E_{ij} = \frac{1}{2}\left(\frac{\partial u_i}{\partial X_j} + \frac{\partial u_j}{\partial X_i} + \frac{\partial u_k}{\partial X_i}\frac{\partial u_k}{\partial X_j} \right) \tag{4.5}$$

The Cauchy stress tensor is formulated in Eq. (4.6)

$$\sigma_{ij} = \frac{1}{J} F_{im} S_{mn} F_{jn} \tag{4.6}$$

where F is the *deformation gradient*, which is an important parameter used in characterization of deformation. The deformation gradient **F** is the Jacobian matrix of the motion described by **Φ**(**X**,t) [21]. It is expressed as

$$F_{ij} = \frac{\partial \Phi_i}{\partial X_j} \equiv \frac{\partial x_i}{\partial X_j} \tag{4.7}$$

The deformation gradient is used to describe an infinitesimal line segment $d\mathbf{x}$ in the current configuration that corresponds to a line segment in d**X** in the reference configuration. This is expressed as

$$d\mathbf{x} = \mathbf{F} \cdot d\mathbf{X} \quad \text{or} \quad dx_i = F_{ij} dX_j \tag{4.8}$$

J denotes the Jacobian of the deformation defined gradient and defined by

$$J = \det(\mathbf{F}) \tag{4.9}$$

In the updated Lagrangian approach, the direct linearization of left hand side of Eq. (4.3) yields

$$\int_{V_0} dS_{ij} \delta E_{ij} dV = \int_{V_{n+1}} \nabla^S \eta_{ij} L_{ijkl} \nabla^S (\Delta u_{kl}) dv \tag{4.10}$$

In the updated Lagrangian approach, the reference state is the current state; therefore the following set of equations is valid:

$$F_{ij} = \delta_{ij} \quad , \quad \delta E_{ij} = \delta d_{ij} \quad , \quad \frac{\partial}{\partial X_i} = \frac{\partial}{\partial x_i} \quad , \quad S_{ij} = \sigma_{ij} \tag{4.11}$$

where F is the deformation tensor and **D** is the rate of deformation. Hence,

$$\int_{V_{n+1}} \left[\sigma_{ij}^{\nabla T} \delta d_{ij} + \sigma_{ij} \frac{\partial v_k}{\partial x_i} \frac{\partial \delta \eta_k}{\partial x_j} \right] dv = \int_{V_{n+1}} \dot{b}_i \, \delta \eta_i dv + \int_{A_{n+1}} \dot{t}_i \, \delta \eta_i da \tag{4.12}$$

where b_i represents the body force and t_i represents the surface traction at the current configuration. The Truesdell stress rate that appear in Eq. (4.12) is defined as [21]

$$\sigma_{ij}^{\nabla T} = \frac{D\sigma_{ij}}{Dt} - \frac{\partial v_i}{\partial x_k} \sigma_{kj} - \sigma_{ik} \frac{\partial v_j}{\partial x_k} + \sigma_{ij} \frac{\partial v_k}{\partial x_k} \tag{4.13}$$

If a rigid body rotation is applied to the body, the usual material rate does not vanish but the Truesdell rate vanishes. Therefore, it has a crucial importance in solution of problems, in which large rotations are present. The constitutive equations can be written in terms of the Truesdell rate of Cauchy stress as:

$$\sigma_{ij}^{\nabla T} = L_{ijkl} D_{kl} \tag{4.14}$$

where L_{ijkl} is the material moduli tensor in the current configuration in terms of material moduli tensor in the reference configuration. On the other hand, in the small strain problems, the classical elasto-plastic modulus is used. It is used to describe the Jaumann rate of Cauchy stress tensor as given in Eq. (4.15).

$$\sigma^{\nabla J} = L_{ijkl}^{ep} D_{kl} \tag{4.15}$$

The Jaumann rate of the Cauchy stress tensor is defined as:

$$\sigma_{ij}^{\nabla J} = \frac{D\sigma_{ij}}{Dt} - W_{ik}\sigma_{kj} - \sigma_{ik} W_{kj}^{T} \tag{4.16}$$

where **W** is the spin tensor given by

$$W_{ij} = \frac{1}{2}\left(\frac{\partial v_i}{\partial x_j} - \frac{\partial v_j}{\partial x_i} \right) \tag{4.17}$$

Substituting using the Eq. (4.15),(4.16) and (4.17), the Truesdell rate of Cauchy stress tensor is written in term of the Jaumann rate:

$$\sigma_{ij}^{\nabla T} = \sigma_{ij}^{\nabla J} - D_{ik}\sigma_{kj} - \sigma_{ik}D_{kj} + \sigma_{ij}D_{kk} \tag{4.18}$$

Thus the relation between the large strain moduli and the classical elastic-plastic moduli is

$$L_{ijkl} = L_{ijkl}^{ep} - \delta_{il}\sigma_{kj} - \sigma_{il}\delta_{kj} + \delta_{ij}\sigma_{kl} \tag{4.19}$$

The last term in Eq. (4.20) does not satisfy the usual symmetry relation. This is not relevant for material plasticity problems since the deformations are approximately incompressible [20]. Hence, Eq. (4.20) may be approximated by

$$L_{ijkl} = L_{ijkl}^{ep} - \delta_{il}\sigma_{kj} - \sigma_{il}\delta_{kj} \tag{4.20}$$

The nonlinear equation Eq. (4.22) is obtained by spatial discretization.

$$\left[K(U)\right]\{\Delta U\} = \{\Delta F\} \tag{4.21}$$

4.5 The Solution Methods

The analyses of metal forming applications require solution of nonlinear equations. There are various techniques of solution, such as Euler method, self correcting Euler method, direct iteration method, Newton-Raphson method and modified Newton- Raphson method [22]. The Newton Raphson method is used in the study.

4.5.1 Newton Raphson Method

The Newton Raphson method is an iterative procedure. The displacement value is recalculated until a certain amount of accuracy is reached. For the nonlinear equation given by Eq. (4.22) the $\{u^{i-1}\}$ is calculated, which in turn yields a residual force defined by Eq. (4.23) [22].

$$[k(\{u\})]\{u\} = \{f\} \tag{4.22}$$

$$\{R(\{u^{i-1}\})\} = \{f\} - [k(\{u^{i-1}\})]\{u^{i-1}\} \tag{4.23}$$

The aim of the procedure is to minimize the value of residual at the end of a number of iterations. The residual force at the i^{th} iteration can be approximated at $\{u^{i-1}\}$ by means of Taylor series expansion Eq (4.24).

$$\{R(\{u^{i-1} + \Delta u^{i}\})\} = (R(\{u^{i-1}\})) + \left[\frac{\partial\{R(\{u\})\}}{\partial\{u\}}\right]_{\{u^{i-1}\}} \{\Delta u^{i}\} + \ldots \tag{4.24}$$

In the last iteration the residual force should approach to zero, therefore Eq (4.24) can be rewritten as

$$-\left[\frac{\partial\{R(\{u\})\}}{\partial\{u\}}\right]_{\{u^{i-1}\}} \{\Delta u^{i}\} = (R(\{u^{i-1}\})) \tag{4.25}$$

Defining tangent stiffness matrix k_t, Eq. (4.25) is rewritten as follows:

$$[k_t(\{u^{i-1}\})]\{\Delta u^{i}\} = (R(\{u^{i-1}\})) \tag{4.26}$$

The solution method is represented in Figure 4.1. The stability of the material depends on the initial guess. It has quadratic convergence properties; in other words the error decreases quadratically in each subsequent iteration. In the nonlinear problems, the Newton-Raphson method is useful, however it may require high computational effort in three-dimensional problems [19].

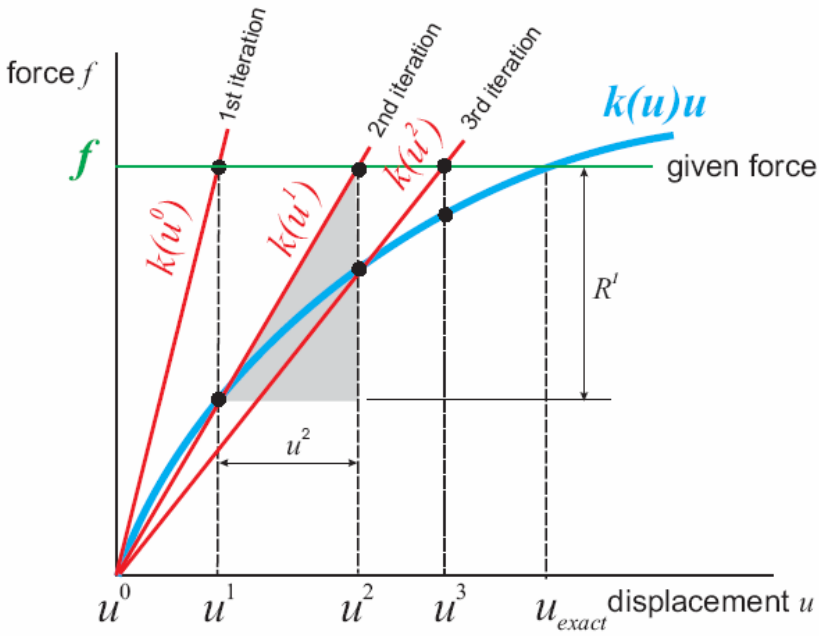

Figure 4.1 The Newton-Raphson method [22].

4.6 Convergence Controls

The convergence criteria are assigned in the calculations in order to conclude the iterations when a desired value of accuracy is reached. In MARC SuperForm, the convergence criteria base on either relative and/or absolute value of residual forces and/or displacements.

Using residual forces as a convergence criterion depends on minimization of the residual forces. Either the absolute value of the residuals or the ratio of the maximum residual load to the maximum reaction force is selected as the convergence criterion. The convergence is defined by the following equations

$$\frac{\left\|F_{residual}\right\|_{\infty}}{\left\|F_{reaction}\right\|_{\infty}} < Tolerance \tag{4.27}$$

$$\left\|F_{residual}\right\|_{\infty} < Tolerance \tag{4.28}$$

where $\|F\|_\infty$ denotes the force with the highest absolute value. The displacements may constitute a criterion for checking the convergence of the solution. The convergence is described by the following equations.

$$\frac{\|\delta u\|_\infty}{\|\Delta u\|_\infty} < Tolerance \tag{4.29}$$

$$\|\delta u\|_\infty < Tolerance \tag{4.30}$$

in which, Δu denotes the displacement increment vector, δu denotes the correction to the incremental displacement vector. In this method, convergence is satisfied if the maximum of the last iteration within an increment is small compared to the displacement change in the increment [19].

One or more of the convergence criteria described above can be used in the solution. If the tolerance intervals decrease the solution becomes more accurate, however the calculation time increases. There is a compromise between the accuracy of the solution and the time; therefore, the convergence criteria should be arranged carefully to obtain the sufficient accuracy in the least amount of time.

4.7 Modeling of Friction

The friction forces between two contacting surfaces depend on various parameters, such as surface roughness, temperature, normal stress and relative velocity. In the numerical modeling, the physics of friction is described by two distinct idealized methods, namely, the Coulomb and shear friction models.

The Coulomb friction model is defined by the following equation:

$$\sigma_{fr} \le -\mu_f \sigma_n \tag{4.31}$$

where σ_{fr} is the tangential (friction) stress, σ_n is the normal stress, μ_f is the friction coefficient. The tangential vector is defined as

$$t = \frac{v_{rel}}{|v_{rel}|} \tag{4.32}$$

in which, v_{rel} is the relative sliding velocity. In the contact problems, along a contact surface, the material flows in opposite directions in different portions of the surface. Therefore, the behavior of friction stress is a step function for a given normal stress. In order to avoid the numerical problems arose due to the discontinuity of the step function, the Coulomb model is relaxed by implementing a new coefficient to Eq. (4.31). The modified equation is given as

$$\sigma_{fr} \leq -\mu\sigma_n \frac{2}{\pi}\arctan\left(\frac{v_{rel}}{C}\right)t \tag{4.33}$$

The term C in Eq. (4.33) represents the value of velocity when sliding occurs. The modifications done on the friction force imposed by introducing relative sliding velocity are shown graphically in Figure 4.2. The value of C, determines how closely the step function is approximated. A large value of relative sliding velocity results in inaccurate representation of the actual case, whereas low value causes difficulties in convergence. It is recommended that the value of be C 1%or 10% of a typical relative sliding velocity, v_{rel} [19].

The frictional model based on the shear stress defines the frictional stress in terms of the equivalent stress in the material

$$\sigma_{fr} \leq -m\frac{\bar{\sigma}}{\sqrt{3}} \tag{4.34}$$

The shear model is appropriate for applications, where the contacting surfaces are at higher temperatures. In the study, the surfaces of the workpiece that have contact

with the dies are not expected to reach high temperatures. Therefore, the Coulomb friction model is used.

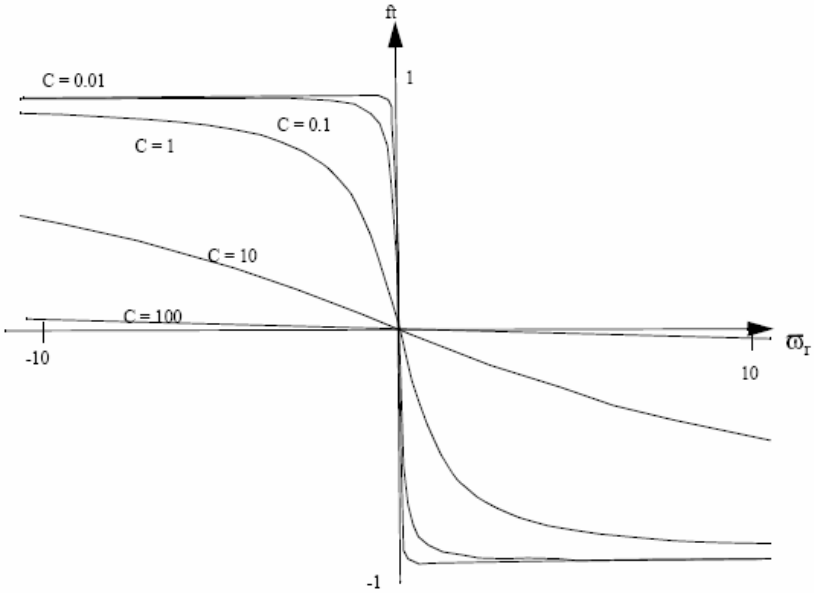

Figure 4.2 Modified modeling of friction (normal force = 1) [19].

4.8 Coupled Thermo-Mechanical Analysis

The thermo-mechanical analysis is utilized in the solution of the mechanical problems, where a temperature change occurs within the material during the process and the variation of properties of the materials due to this temperature change is significant. Also, the heat generation in a mechanical problem due to plastic work or an external heat source requires a coupled analysis. The thermal and mechanical analyses are carried out in each load/time increment [19].

The thermal strains are created within the body due to change of temperature. These are calculated by the following formula:

$$\Delta\varepsilon^{th} = \int \alpha \Delta T \tag{4.35}$$

where $\Delta\varepsilon^{th}$ is the strain increment, α is the coefficient of thermal expansion and ΔT is the temperature increment. The nodal forces due to thermal strains are then added to nodal force vector during solution.

In the general procedure of the coupled thermo-mechanical analysis, at a time step *t*, the mechanical equilibrium equations are solved using the flow curve corresponding to the temperature at the beginning of the time step. The geometry is updated at the next time step, $t+\Delta t$. A pure thermal analysis is carried out at $t+\Delta t$ and a new temperature distribution is calculated. The mechanical calculations are carried out by the using the updated temperature values. The flow diagram of the coupled process is given in Figure 4.3

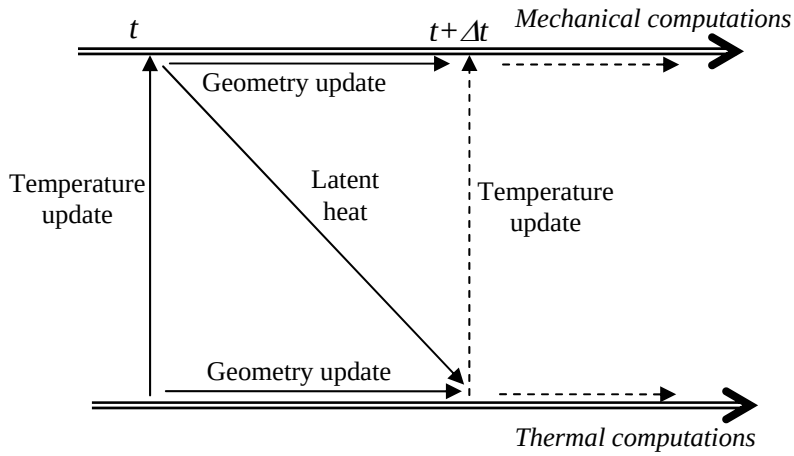

Figure 4.3 Flow chart of the coupled thermo-mechanical analysis.

4.9 Electromagnetic Field Analysis

Besides the solid mechanic applications, the calculations regarding the electromagnetic fields can be carried out by means of finite element method. In this study, the induction heating is simulated by FEM. ANSYS 7.0 is used as software in the calculations.

3-D harmonic magnetic analysis is used in analyzing magnetic fields caused by low frequency alternating current (AC). The field quantities are calculated by solution of the Maxwell's equations as explained in Section 3.2.5. The two possible alternatives of the analysis in ANSYS are the magnetic vector potential (MVP) formulation or the edge-based formulation. In the MVP formulation, the degree of freedom is associated with the element nodes, whereas in the edge based formulation it is associated with the element edges. The MVP formulation provides erroneous results at the interfaces of elements that have different magnetic permeability values. On the other side, the edge based formulation provides ease of modeling of components with different permeabilities and furthermore it is recommended in most 3D harmonic electromagnetic analyses [23]. Therefore the edge based formulation is used in the numerical simulation of induction heating.

In a harmonic analysis, the time dependence of the varying quantities, such as current, etc., is described by periodic functions. Any field quantity *q(r,t)* that is function of time and space, is defined as

$$q(r,t) = c(r)\cos(\omega t) - s(r)\sin(\omega t) \tag{4.36}$$

where, ω is the angular frequency of time change and *c(r)* and *s(r)* are the measurable field values at ωt = 0 and ωt = -90 degrees, respectively. In an electromagnetic analysis, *q*(*r*,*t*) can be the flux density {B}, the magnetic field {H}, the electric field {E}, the current density *J*, etc. Due to the complex nature of the solution, the calculated quantities are stored as two different sets of solutions. The *real* part of the solution gives the results for ωt = 0 whereas the *imaginary* part describes the solution at ω = -90. Some of the quantities, however, are expressed as time averaged values. For the Joule power denstiy, which is the main quantity to be obtained from electromagnetic field calculations, the time average value is calculated. It represents the average heat generation rate per unit volume. This quantity is formulated as

$$
\begin{aligned}
Q^j(t) &= J(t)E(t) \\
&= (J_r \cos(\omega t) - J_i \sin(\omega t))(E_r \cos(\omega t) - E_i \sin(\omega t)) \\
&= J_r E_r \cos(\omega t)^2 + J_i E_i \sin(\omega t)^2 - (J_i E_r + J_r E_i)\sin(\omega t)\cos(\omega t)
\end{aligned} \tag{4.37}
$$

where Q^j is the Joule power density per unit volume, J is the current density, E is the electric field. The time average of $\cos^2(\omega t)$ and $\sin^2(\omega t)$ terms is ½ whereas that of sin cos term is zero. Therefore the time average of joule heating density is

$$
Q^j = \frac{1}{2}(J_r E_r + J_i E_i) \tag{4.38}
$$

and the subscript r and i denote the real and imaginary parts of the solution, respectively. This quantity represents the average heat generation rate per volume in induction heating and is expressed as a function of space coordinates only. In order to simulate the temperature increase within the specimen, the time average value of Joule heating density is used in the thermo-mechanical calculations.

CHAPTER 5

EXPERIMENTAL STUDIES

5.1 Introduction

In the first part of the study, free forming of locally induction heated specimens is investigated experimentally. In the experiments, effects of heating parameters, geometry and material of the workpiece on the efficiency of the process are examined. In this chapter, the experimental studies and their results are presented.

5.2 Experimental Set Up

The experimental set up consists of a hydraulic press, an induction heating machine and a temperature measuring device (Figure 5.1). The units constituting the experiment set up are described below.

5.2.1 Hydraulic Press

The free forming process is realized by means of a hydraulic press. The hydraulic press used in the experiments, is a Bucher-Guyer type LS 150 press with four columns. Appropriate flat dies have been selected for the process and they were mounted on the press. The machine can supply a maximum press force of 150 N. The forging speed varies between 3.7 mm/s and 10 mm/s.

Lubricant is applied on the flat dies in order to reduce friction and tool wear. The GleitMetall-Paste of Techno Service GmbH is selected as the lubricant. It can be applied where the maximum working pressure does not exceed 2353 N/mm^2 and temperature range is between -180^{o}C and 1450^{o}C. It is resistant to water, oil and benzene.

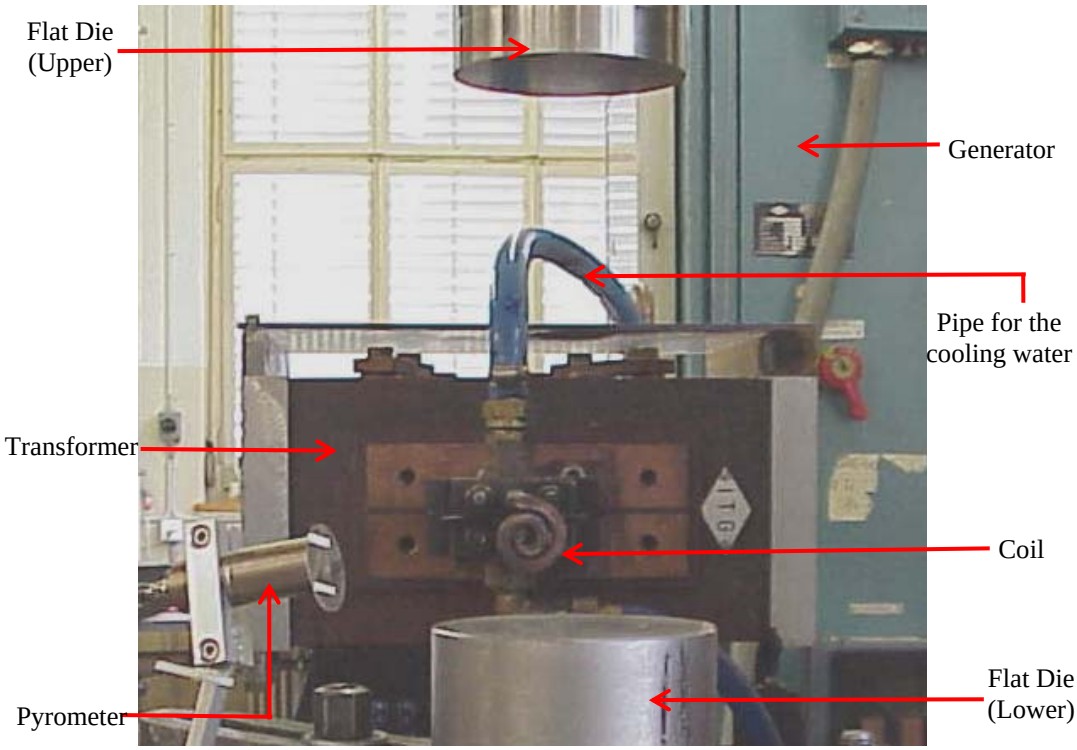

Figure 5.1 Experimental set up.

5.2.2 Induction Heating Unit

During the local heating of the specimens, a unit that is composed of a power supplier (or generator), a transformer, a helical coil and a water pump is used. The power supply is capable of supplying 80 kW energy to the system Figure 5.2(a). The alternating current supplied can have frequencies up to 10 kHz. It is connected to a transformer by which the magnitude of the current on the coil is regulated

(Figure 5.2(b)). The helical coil is mounted on the casing of the transformer. It is manufactured by bending a copper tube with square cross section into a helical shape. Water is pumped into the canal passing through the coil in order to avoid excessive heating of the coil. The cooling water comes from the city water line and enters a pump before it goes through the coil. The cooling rate of the coil is increased by means of the pump.

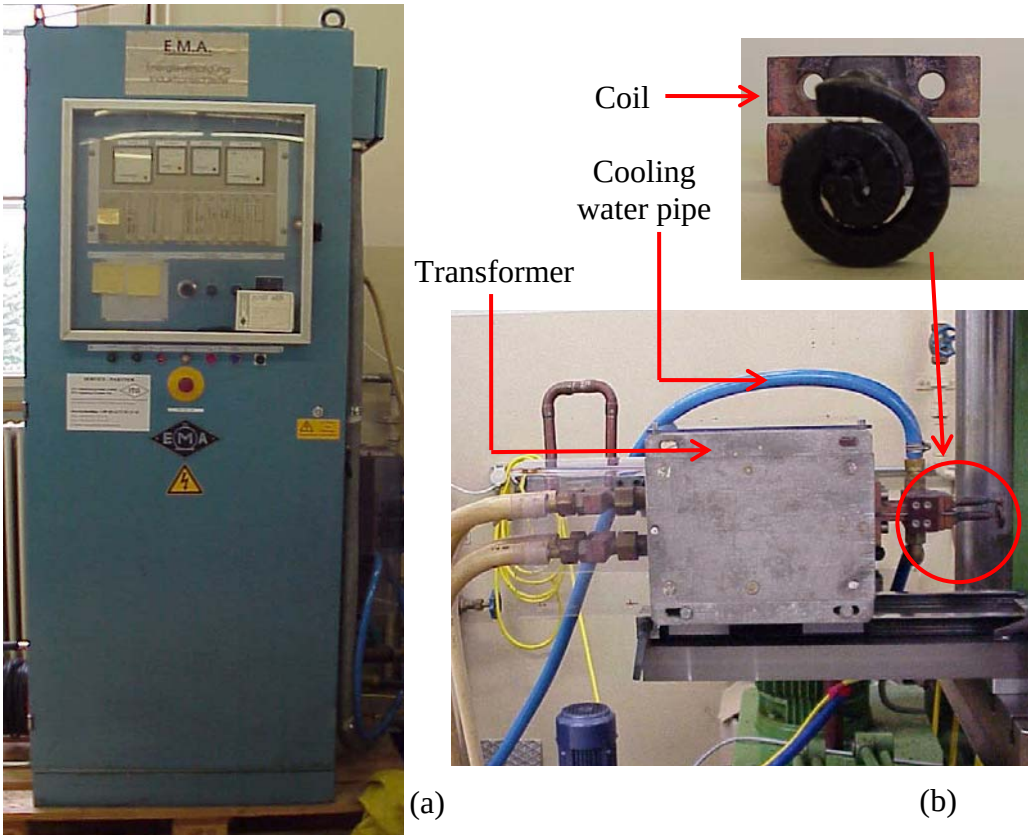

Figure 5.2 The induction heating unit. (a) Generator. (b) Transformer.

5.2.3 Pyrometer

The temperature on the surface of the workpiece is measured by a pyrometer. Two-color pyrometer KOTTONAU INFRATHERM IGAQ 10-LO is used in the experiments. It is a completely digital non-contact temperature measurement instrument with fiber-optics. Since the processing of the measured data is digital,

the readings are reliable. The measurement range of the device is between 349^{o}C and 1349^{o}C. The pyrometer head is aligned with the integrated laser-pilot-light [24]. The laser spot of the pyrometer, which indicates the exact location of temperature reading, is focused at a point on the surface of the specimen. The device records the maximum temperature reading within the area pointed by the laser spot. The laser spot should be adjusted such that the spot has the minimum possible area on the workpiece surface. The adjustment of the laser spot is critical in terms of accuracy of the pyrometer reading since this area is directly influenced by the distance and the angle between the pyrometer head and the workpiece surface.

5.3 Specimens

One of the major aims of the study is to investigate the effect of physical properties of the materials on the applicability of the process. Three different materials are selected from the available materials regarding the discrepancies in some of their physical properties. They are 16MnCr5, X5CrNi18 9 and Ti6Al4V.

16MnCr5 is an alloyed case hardening steel. It is mainly used where 800-1100 N/mm^2 of tensile strength is required. It has a good wearing resistance, and is commonly used for bolts camshafts, levers, pins, links, and some other components [25, 26].

X5CrNi18 9 is a type of austenitic Cr-Ni stainless steel. It has a high ductility and can be used in forming, spinning and drawing operations. It is essentially nonmagnetic, however becomes slightly magnetic when cold worked. It is used widely in manufacturing of chemical equipment, food processing equipment, marine equipment, kitchen equipment, pressure vessels, hospital surgical equipment and refrigeration [27].

Ti6Al4V is the most widely used titanium alloy in industry. It is used in both open die forgings, closed die forgings. Among the forgeable titanium alloys Ti6Al4V has an intermediate formability. It is not as good as ferrous alloys, regarding the flow stress and crack sensitivity; however can be easily forged when compared to nickel- and cobalt-base super alloys [28].

The physical properties of the selected materials are presented in Table 5.1. The material properties of 16MnCr5 and X5CrNi18 9 are obtained from the database of MARC. The properties of Ti6Al4V are taken from the material database MSC.DataMart.

Table 5.1 Material properties at room temperature.

	Units in SI	**16MnCr5**	**X5CrNi18 9**	**Ti6Al4V**
Young's Modulus	GPa	212	196	119
Poisson's Ratio	-	0,300	0,300	0,342
Mass Density	kg / m^3	7850	7850	4429
Thermal Expansion Coef.	1 / °C	1.15E-05	1.61E-05	9.40E-06
Thermal Conductivity	W / (m.K)	45,90	14,50	7,27
Specific Heat	J / (kg.K)	461	472	574
Thermal Diffusivity	m^2/s	1.270E-5	3.91E-6	2.86E-6

The flow stress curves of the materials are presented in Figure 5.3. The stress values of Ti6Al4V is plotted for a strain rate of 10 1/s. The strain rate for 16MnCr5 and X5CrNi18 9 is 8 1/s. The flow stress values of 16MnCr5 and X5CrNi18 9 are taken from the material database of MARC, which is supplied by the commercial software. The flow stress for Ti6Al4V is obtained from the material database MATILDA.

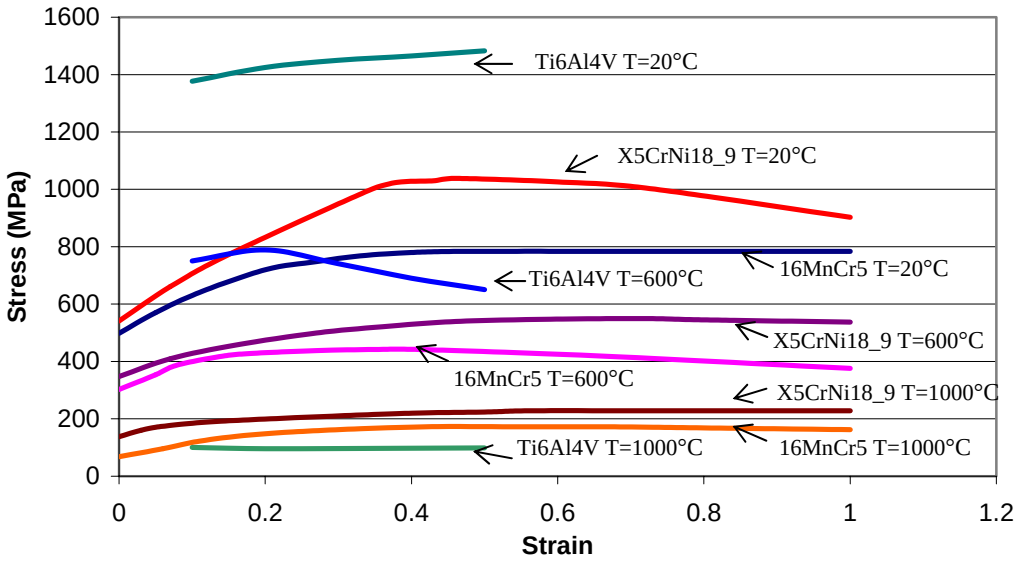

Figure 5.3 The flow stress values of the materials.

In the local heating process, the thermal diffusivity (α) of the materials plays an important role. Thermal diffusivity can be described as material's capability to conduct thermal energy relative to its capability to store this energy [29]. This quantity is defined as the ratio of thermal conductivity (k) to product of specific heat at constant pressure (c_p) and mass density (ρ). It is given as

$$\alpha = \frac{k}{\rho . c_p} \tag{5.1}$$

Thermal conductivity indicates how well heat energy is transmitted through the material. If heat is supplied only to a specific portion of a specimen, high thermal conductivity will cause heat energy to be diffused into the entire volume of the material. It will enhance through heating of the material and prevent localized accumulation of heat energy. Therefore, low thermal conductivity is desired in local heating applications.

The thermal diffusivity is inversely proportional to the product of c_p and ρ, which is also termed as "volumetric heat capacity". With a high heat capacity, the

material will store more of the supplied energy before it transmits heat further. High values of heat capacity will enhance local heating.

In all of the heat transfer processes, there will be a transient period, in which temperature distribution within the control volume changes. After a certain instant, most of those processes will turn to steady state. There will be no further change in the temperature of any point within the material. In the transient stage, both thermal conductivity and volumetric heat capacity effect the temperature distribution whereas in the steady state phase only the thermal conductivity has an effect.

In this study, heating process is terminated within the transient period; therefore thermal diffusivity should be taken into account when choosing materials. The change of thermal diffusivity values of the selected materials with temperature is presented in Figure 5.4. The temperature dependency of the mass density is neglected in the calculations. The materials show different characteristics. This will allow investigation of distinct temperature gradients on the effectiveness of the upsetting process followed by local heating.

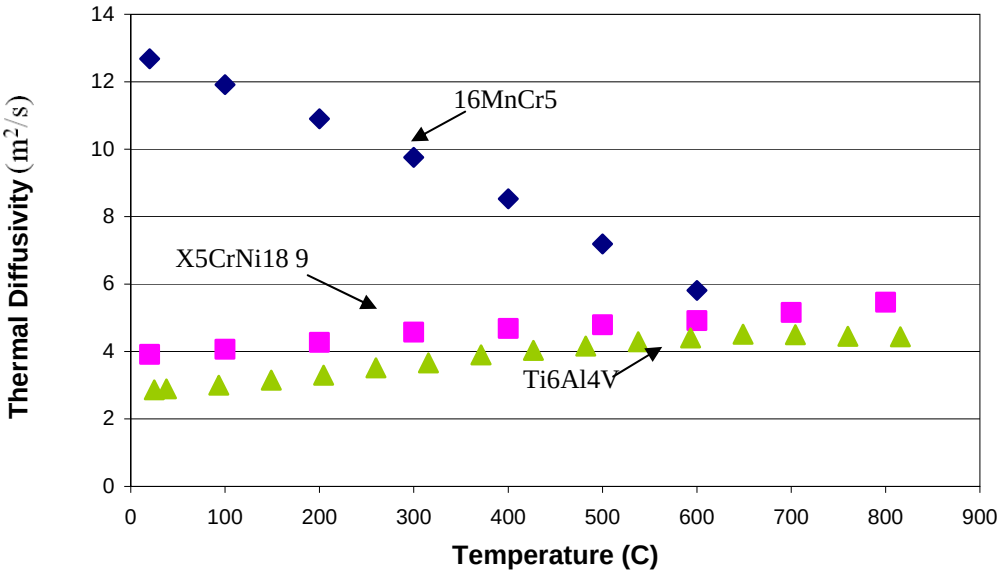

Figure 5.4 Comparison of the thermal diffusivities of the selected materials.

The dimensions of the test specimens are decided regarding the available material and limitations of the experiment set up. The dimensions of the specimens are given in Table 5.2. One of the most important parameters that affect the final shape of the forged specimen is its height to outer diameter ratio. The critical ratio for solid steel specimens is reported as 2.3 in single stroke upsetting [1]. On the other hand, the specimens are not allowed to be less than a certain length due to set up restrictions. During induction heating, the workpiece should be clamped between the flat dies, in order to avoid its movement due to the magnetic field. The current carrying coil therefore stays between the flat dies during heating (Figure 5.1). A distance of about 42 mm between the two dies would theoretically be sufficient for the coil to fit in the gap between them. However, as the coil – die distance decreases, the dies are heated more by electromagnetic induction. Therefore high gap distance is desirable to maintain tool quality. Regarding the buckling problem of the workpiece and heating problem of the dies, an optimum length of 60 mm is selected for the 30 mm diameter workpieces. The length to diameter ratio is 2, which remains below the critical limit for the solid specimens. Also, excessive heating of the dies are avoided. The workpieces with larger diameters are more favorable in terms of the problems stated above. However, for 60 mm diameter workpieces, the maximum press force is exceeded; therefore only hollow workpieces of this dimension are used.

Table 5.2 The geometrical specifications of the cylindrical specimens.

Material	Outer Diameter (mm)	Inner Diameter (mm)	Length (mm)
16MnCr5 Ti6Al4V X5CrNi18 9	30	0, 14, 16, 18, 20	60
	40	0, 21, 24, 27, 29	80
	50	0, 27, 30, 33, 37	100
	60	40, 44	120

The outer diameter of the specimens has 4 different values (Table 5.2). These values are limited by the dimensions of the available material and the power of the

press. The inner diameters of the hollow specimens are determined arbitrarily. For the specimens with different outer diameter values, the ratio of inner diameter to outer diameter is kept constant. Also, the ratio of length to outer diameter is kept as 2, for comparison at the evaluation stage.

5.4 Experimental Procedure

5.4.1 Preparation Stage

The workpieces are supplied as bars with 30, 40, 50, and 60 mm of outer diameters. They are cut and drilled to the desired dimensions on the lathe. The criteria of determining the dimensions are presented in Section 5.3.

As the first step, the residue of lubricant or dirt is removed from the die surfaces. Dies are cooled down to room temperature by means of an air gun if they are heated in previous experiments. The lubricant is applied on the upper and lower dies and on both of the flat surfaces of the cylindrical workpiece. The lubricant is also applied on the heated part of the specimen in order to prevent corrosion during heating. However, in the later stages of heating the lubricant on the heated surface melts down.

The workpiece is placed on the center of the lower die. The coil-workpiece distance is checked in each single experiment and it is ensured that this distance is 3 mm. The distance value is determined arbitrarily in preliminary heating trials.

Temperature data of a predetermined point on the surface of the specimen is recorded in the experiments. The location of the point is indicated schematically in (Figure 5.5). This point has been chosen arbitrarily, regarding the location and the ease of measurement. It is located on the heated portion, where most of the heat is generated in induction heating and therefore appears red during heating. By this

way, the discrepancies in heating characteristics of different experiments can be observed. The other factor that effects the selection of location of the point is the location of the pyrometer. The pyrometer head should be normal to the workpiece surface at the point, where the device takes the temperature data. The position of the pyrometer head is arranged by the help of a laser spot that originates from the head. It is focused on the surface and position of the head is arranged regarding the intensity and size of the small red spot at the point the laser beam hits the workpiece surface.

After the positioning of the specimen is completed, the workpiece is clamped between the dies.

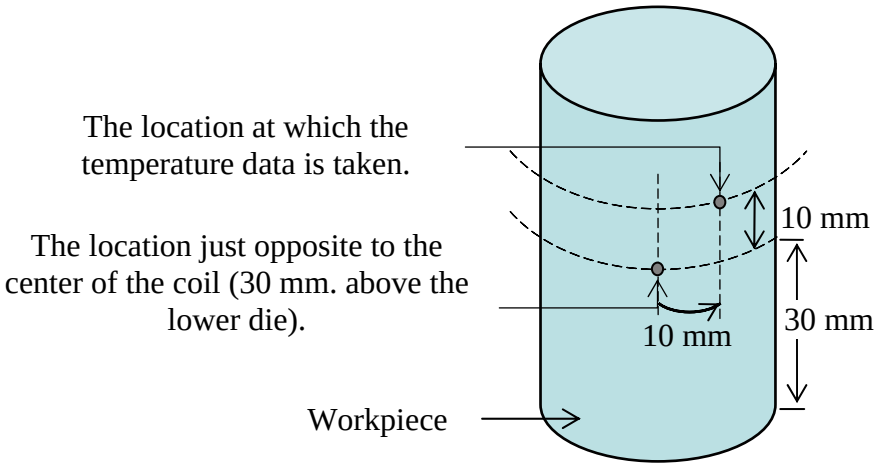

Figure 5.5 The location, where the temperature is recorded by a pyrometer.

5.4.2 Heating Stage

In each experiment, the specimen is heated to a desired temperature by means of an induction heating unit. A specimen is shown in the heating stage in Figure 5.6. The workpiece is held between the two dies and the coil is brought to the heating location. As the generator is switched on, current passes through the coil and a magnetic field is created. Due to this field current is induced on the workpiece. The

orange colored field seen in Figure 5.6 is the high temperature region, where most of the thermal energy is generated as a result of current flow. The pyrometer head that is focused on a single point, records the temperature data.

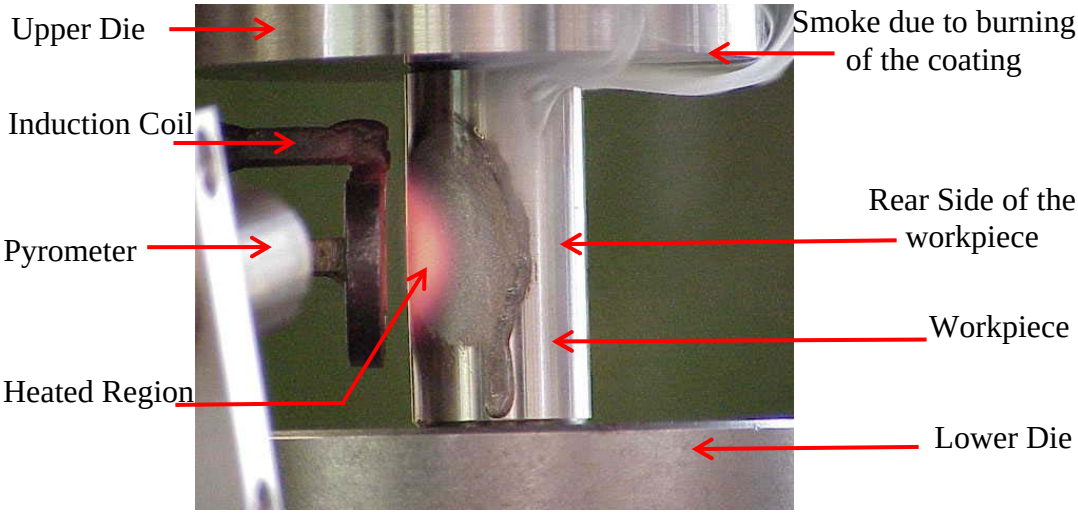

Figure 5.6 Heating stage of a standard experiment.

The oxidation of the workpiece is tried to be minimized by coating the surface. The coating burns at elevated temperatures; however it still supplies some protection in the early stages of heating and on the lower temperature regions.

Different heating parameters are tried during the experiments. The controlled and uncontrolled heating parameters are presented in Table 5.3. The voltage and current values of the current indicated in the table are the readings obtained from the generator unit and do not represent the values on the coil. These values are adjusted automatically by the induction heating unit depending on the *Mf Switch value* and the *gear ratio*. Heating stage is terminated after a certain period of time or after a predetermined temperature reading is reached. The generator is stopped and the transformer is pulled back manually on the slides.

Table 5.3 The parameters of the induction heating process.

Controlled Parameters						**Uncontrolled Parameters**
Specifications of the Induction Heating Machine					Coil - Workpiece Distance (mm)	Power Reading on the Induction Heating Machine (kW)
Voltage (V)	Current (A)	Frequency (Hz)	Mf Switch Value	Gear Ratio		
300, 350	120, 130, 140	7.8, 10.5	6, 6.5, 7	07:01, 09:01, 11:01	3	26 – 40

5.4.3 Forming Stage

Forging process is started after the heating stage. Press is turned on manually just after the transformer is pulled back. In order to prevent any damage, a security light is installed to the set up to inform the press operator about the position of the transformer. It is turned automatically to green when the transformer is pulled back and indicates that the press can safely be operated.

The workpiece is pressed between the flat dies with a speed of 3.7 mm/s. In most of the experiments, ratio of final length to initial length is 3/4. The press is stopped manually by the operator, when the lower die is displaced by the desired amount. After forging is completed, the workpiece is removed.

5.5 Interpretation of the Experiment Results

The experimental investigation of the process is includes determination of the effects of some parameters on the mechanism of deformation and on the shapes of the products. The conclusions are drawn by investigating more than 200 cases. A list of the experiments is given in Appendix A. The results shown below summarize the observations in the experiments. The cases shown in the text are denoted by the original name of the test, which is also indicated in Appendix A. Before investigating the effects of parameters, the typical formations observed on the products are presented.

A typical product obtained from a hollow workpiece is shown in Figure 5.7(a). On the heated region, a local bulge is obtained in most of the experiments. The material flow in localized on the heated portion, due to the increased formability of metals at elevated temperatures. In the hollow workpieces, a secondary bulge is also formed on the inner side of the heated wall of the workpiece. It is observed in the experiments that the shape and size of the two types of formations depend on the heating parameters and the initial geometry of the workpiece.

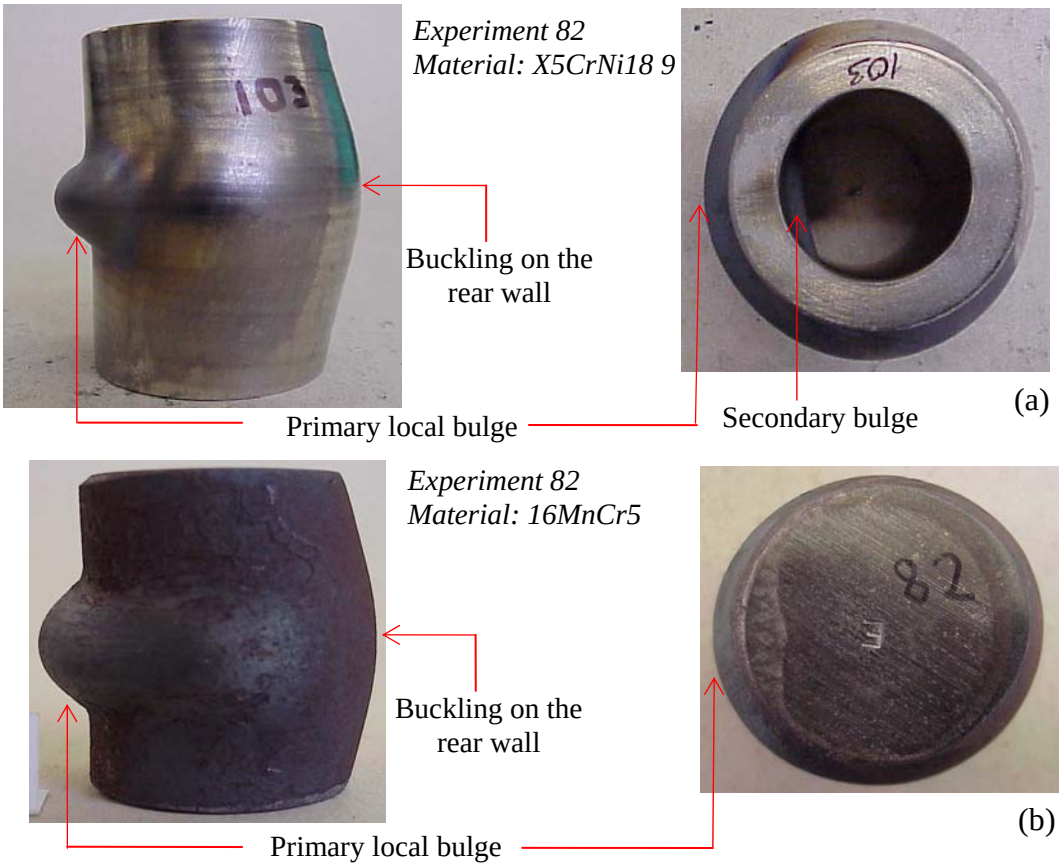

Figure 5.7 The hollow and solid specimens.

An example of a solid workpiece is shown in Figure 5.7(b). Local bulge formation is observed on the heated side of the workpiece. In both of the specimens, the rear wall of the specimen that has a lower temperature than the heated side has a barreled shape due to buckling. These cases show the typical products of the local

heating and free forming process. The details of the process and effects of some parameters on the product shape are discussed later in this chapter.

5.5.1 Effect of the Material

The important material properties that effect the temperature distribution in an induction heating process are the thermal diffusivity, electrical conductivity and the magnetic permeability. In the free forming stage, the product shape is dependent on the thermal diffusivity and the flow stress of the material. In principle, for investigation of the effect of a parameter, the other experiment parameters should be kept constant. However, in experimental investigation of the effect of material on the process, this is practically impossible. Therefore, the cumulative effect of the mentioned material properties is investigated in this section. For the comparison of different tests, the maximum temperature reading is kept constant in the subsequent experiments.

As explained in Section 5.3, the thermal diffusivity (α) of the materials has a significant effect on the effectiveness of the induction heating process. In a heat transfer process, the materials with higher α values reaches to steady state faster than the ones with lower α values. Therefore, through heating is observed within the specimen as α increases. In such cases, at end of the free forming process, the bulge is not localized; axisymmetric flange formation is observed around the circumference of the workpiece.

The sensitivity of the flow curve to temperature changes is also an important factor in the process. The rapid decrease of flow stress with temperature is expected to work in favor of local deformation. On the other side, the electrical conductivity and magnetic permeability are important since they determine the spatial heat generation pattern during induction heating.

The effect of material properties are observed on solid specimens. Three geometrically identical workpieces, made of 16MnCr5, X5CrNi18 9 and Ti6Al4V, are heated with the same parameters and their final lengths are identical at the end of forming. The products are shown in Figure 5.8. In all of the experiments, the maximum temperature reading of the pyrometer is about 850-900°C.

(a)

Experiment 81
Material: 16MnCr5
L_1/L_0: ¾
Heating Time: 30 s

(b)

Experiment 64
Material: X5CrNi18 9
L_1/L_0: ¾
Heating Time 52 s

(c)

Experiment 63
Material: Ti6Al4V
L_1/L_0: ¾
Heating Time 22 s

Figure 5.8 Specimens made of (a) 16MnCr5 (b) X5CrNi18 9 and (c) Ti6Al4V. Heat is induced on the left side of each of the specimens.

The heating times of the processes are different than each other. If the values of heat generation rate in the workpieces were identical, it is expected that the heating time to reach a specific temperature on the surface would be directly proportional to the thermal diffusivity of the material. However, in case of induction heating, the heat generation rate varies from material to material, although identical current is applied to the induction coil. Furthermore the spatial heat generation pattern is directly influenced by the material properties. Therefore, in those three cases, the process time does not increase with increasing thermal diffusivity of the material. In the 16MnCr5 specimen heat generation is concentrated on a narrower volume below the surface of the specimen than the other two specimens. Therefore, the target temperature is reached in a shorter time than on the stainless steel specimen even though the heat diffusion is much more pronounced in 16MnCr5 specimen due to high thermal diffusivity (Figure 5.4). On the other side, the total heat generation on the Ti6Al4V specimen is distributed on a wider volume below the surface compared to the other materials. However, the low thermal diffusivity of the materials compensates the effect of relatively low heat generation rate on the surface and results in rapid increase of temperature near the surface. The characteristics of heat generation in induction heating process are analyzed in detail in Chapter 7.

The apparent differences in shape of the local bulge in Figure 5.8, are due to the flow stress and the thermal diffusivity of the material. The main contribution of thermal diffusivity to the process is that it determines directly the temperature distribution. In case of low thermal diffusivity values, at a certain instant before the process reaches steady state, the temperature gradient between the surface and the inner portions of the workpiece, is steeper than a material with higher thermal diffusivity. In other words, the temperature distribution is more homogeneous if the thermal diffusivity is higher. This fact results in material flow to be localized in a smaller volume around the heated region for low thermal diffusivity cases. As seen in Figure 5.8, the ratio of bulge width to bulge height is relatively larger for the Ti6Al4V specimen. In other words, the deformation is restricted in a local area.

Another factor that affects the shape of the bulge is the dependence of flow stress on temperature. It is seen in Figure 5.3 that the flow stress of the titanium alloy is more sensitive to temperature changes when compared to the other two materials. This fact also works in favor of localization of bulge. Therefore, material flow is localized in the bulge region for the Ti6Al4V specimen. The effects of material properties on the process are discussed further in Chapter 8.

5.5.2 Effect of Heating Parameters

The heating parameters, such as heating time, heat flux and energy generation rate, have a direct influence on the final temperature distribution at the end of the heating stage. The desired temperature distribution can be obtained by many ways, i.e. using different combinations of the values of the mentioned parameters. In this section, discrepancies in product shape due to variation of total heating time are investigated. The other process parameters are kept constant in the following experiments.

As the heating time is increased, specimen is heated to elevated temperatures and heat diffuses into a wider volume along the diameter and the length of the workpiece. Since the yield strength of metals decreases with increasing temperature, the more volume of the material flows into the bulge area.

The temperature readings of the pyrometer during the heating stage for three different tests are given in Figure 5.9. The rate of temperature increase reduces as time proceeds and the heating process approaches to steady state. The most important reasons of this situation are the increase in rate of radiative and convective heat transfer rate on the surface.

The products of the three tests are given in Figure 5.10. The solid Ti6Al4V specimens are heated with the same heating parameters for different time intervals.

As a seen in the figure, the amount of material on the local bulge increases as heating time increases. In case of 53 s of heating the height of the bulge is about two times of the bulge obtained after 22 s of heating.

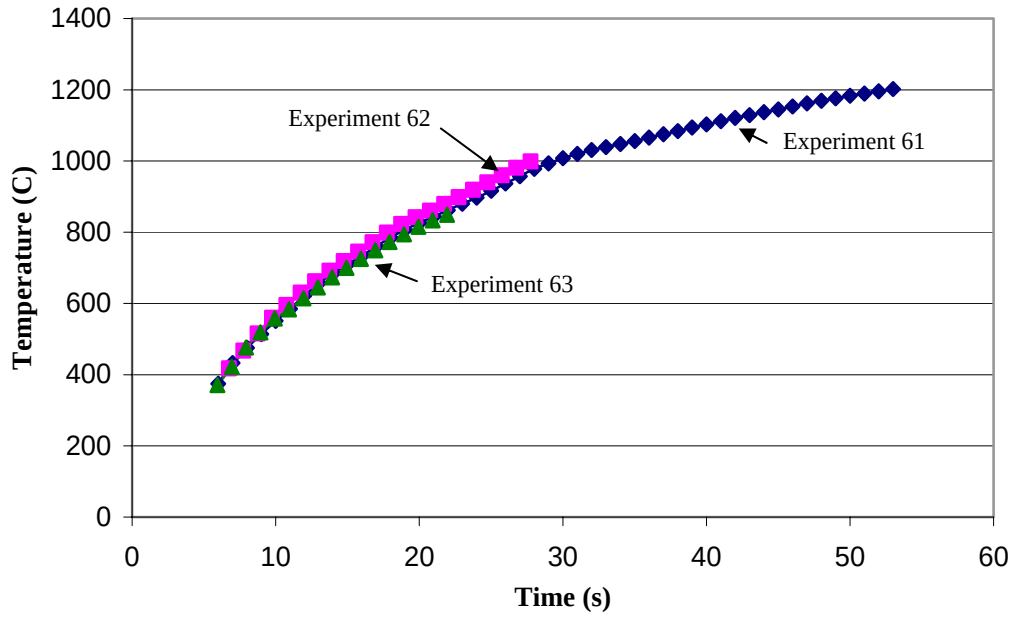

Figure 5.9 The experimental temperature data of the specified point.

Increase of heating time affects the final shape of the rear side of the specimen. As seen in Figure 5.10(a), the rear walls, which are below and above the relatively hot middle portion, maintain their vertical shapes. On the middle portion a bulge is observed that resembles the one on the heated side. Also, the diameter of bottom surface of the workpiece is 30.2 mm, which deviates about 0.7% from its initial value. In other words, deformation is localized on the middle portion, i.e. about half length of the workpiece from each of the dies. The specimens in Figure 5.10(b) and (c) are heated about 28 s and 22 s, respectively, prior to deformation. They show different characteristics compared to *Experiment 61*. The rear wall is shaped as an arc that extends from the lower die to the upper die. Deformation is not localized in the middle section.

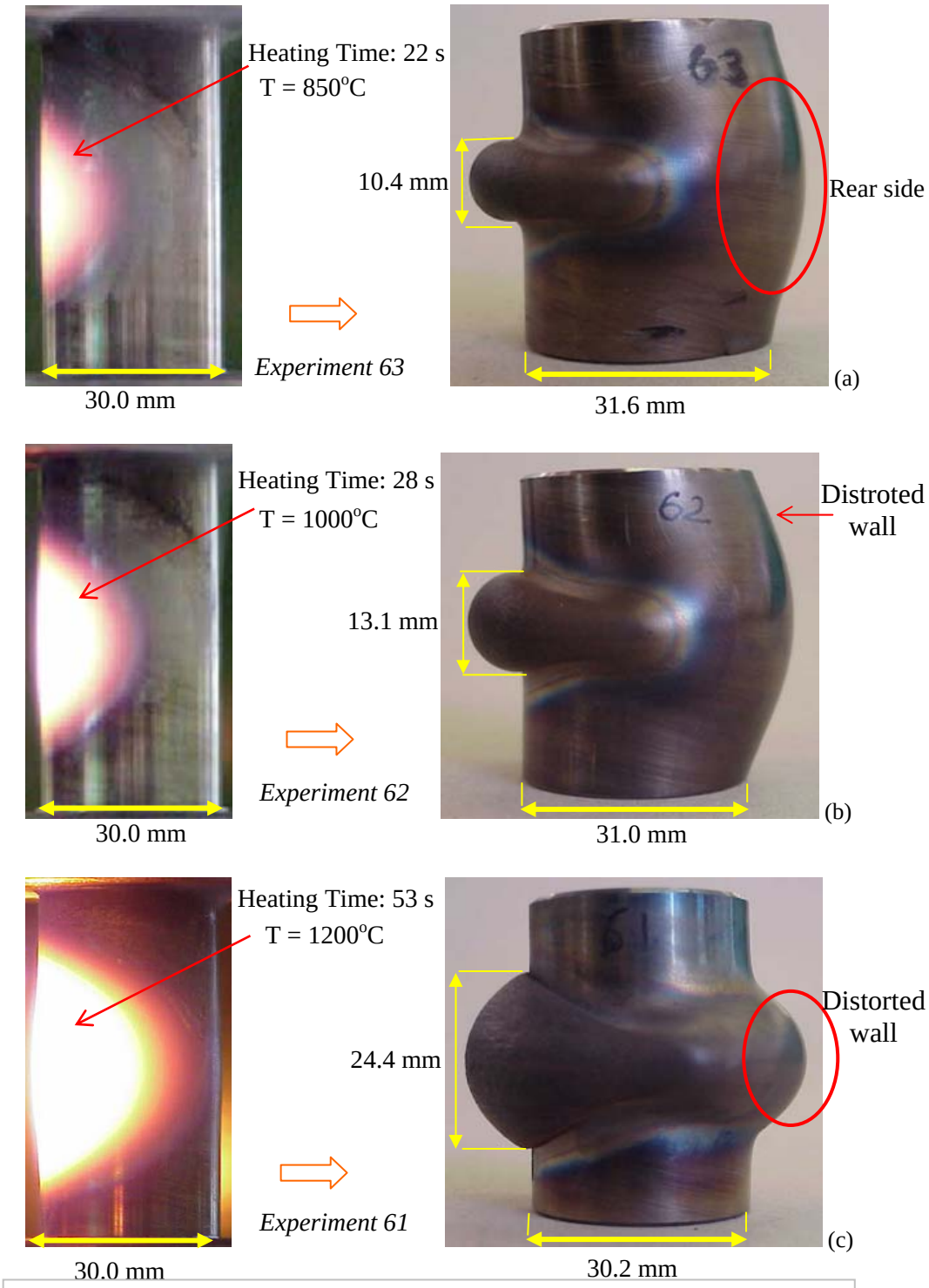

Figure 5.10 The initial and final shapes of the solid specimens are presented. Heat is given from the left side.

The discrepancies in the final shapes can be explained by temperature distribution within the workpiece. As time proceeds, the temperature increases and heat propagates in the radial direction. The heated material looses ability to resist the compressive loads, such that the whole body behaves as if there is a notch in place of the hot material. In other words, higher ratio of the press force is *carried* by the "cooler" rear portion. When the cross sectional area of this portion decreases; it tends to buckle under the load. The rear side formation in *Experiment 63* and *Experiment 62* in Figure 5.10 can be explained by this situation. In *Experiment 61*, a further stage of this fact is observed. On the middle portion, carrying capability of the material on the heated side is diminished due to higher temperature. The minimum temperature on the rear side is also increased. On the other side, due to the heat loss on the heated side of the specimen, on the middle section, the temperature gradient along the radius is lowered. In other words, final temperature distribution resembles a case of axisymmetric heating of the middle section. Therefore, the bulge formation on the rear side shows similar characteristics as the heated side. The workpiece behaves like a 3-layer workpiece that has a softer material in 2nd layer, rather than a specimen with a notch on the side wall.

As a supporting evidence of the described forming mechanisms, top views of the specimens are investigated Figure 5.11. In *Experiment 63* and *Experiment 62*, the workpiece tends to fold over the heated portion that is weak in terms of strength. Therefore, the part of the surface of the specimen loses contact with the die on the heated side. The specimen loses its vertical shape and bends over the heated region. Due to bending of the specimen, the side walls come into contact with the dies on the rear side and are pressed. A crescent shape formation is observed on the backside of the workpiece Figure 5.11(a) and (b). On the other hand, in *Experiment 61*, there is no such formation the top surface of the specimen Figure 5.11(b). As explained before, the side walls do not bend over the heated region. The portions of the specimen above/below the heated area move only on a hot 'pillow', as a rigid body.

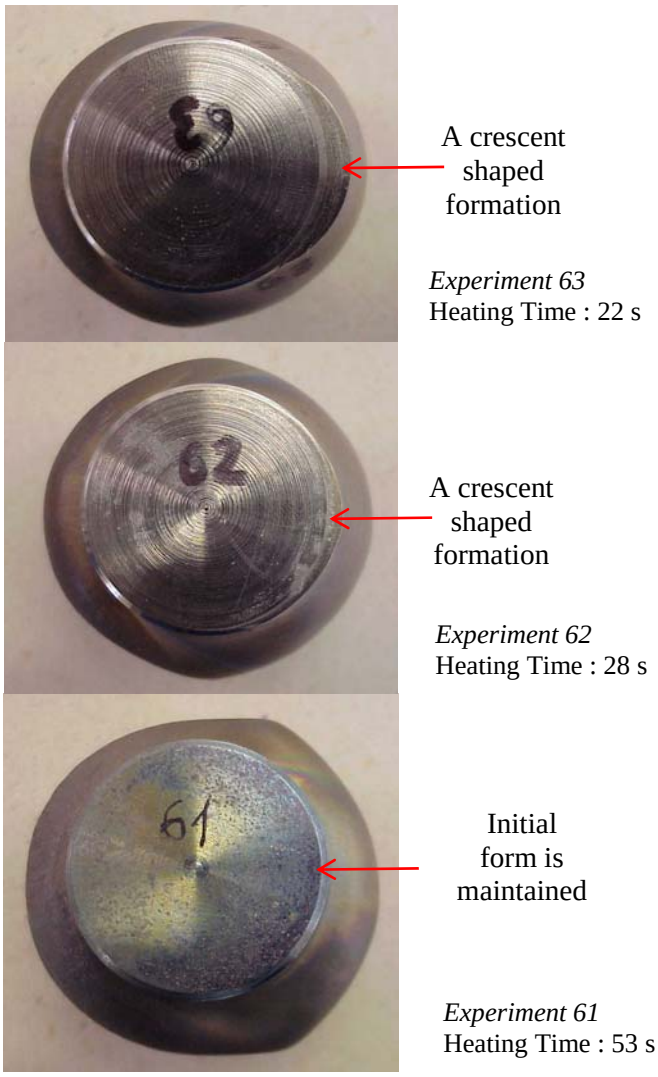

Figure 5.11 Top side view of *Experiment 61, 62* and *63*. Heat is generated on left.

Depending on the temperature, the wall of the specimen on the heated side of the specimens may lose its vertical orientation. The side walls of the cylinder above and below the heated part are extensions of the rear part of the specimen, which carries most of the forming load. Due to buckling of the specimen, the vertical shape of the walls is distorted. As seen in (Figure 5.12), as the overall temperature is increased and heat diffusion is enhanced by increasing the heating time, the deflection of the walls above and below the heated region is avoided. Those parts will move as a rigid body on the hot material, without being effected by folding of the rear wall of the specimen.

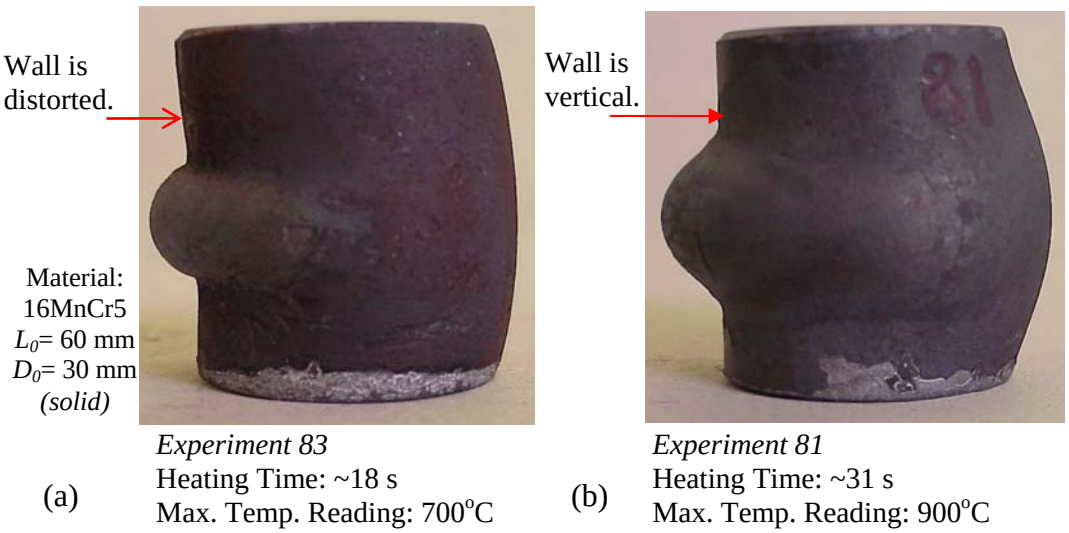

(a) *Experiment 83*
Heating Time: ~18 s
Max. Temp. Reading: 700°C

(b) *Experiment 81*
Heating Time: ~31 s
Max. Temp. Reading: 900°C

Figure 5.12 Effect of temperature on deflection on the heated side of the specimen.

5.5.3 Effect of Geometry

In the experiments, buckling is observed in most of the specimens. The distortion of shape due to buckling becomes more pronounced in hollow workpieces. Decreasing the ratio of length to diameter of the workpiece may avoid buckling. Due to the limitations of the experimental set up, length of the workpieces cannot be decreased; therefore large diameter workpieces are investigated.

The effect of wall thickness on product geometry can be visualized in Figure 5.13. The hollow workpieces that have outer diameter of 30 mm are compared to the ones with 40 mm of outer diameter. The ratio of inner to outer diameter is kept constant for the two types of workpieces. It is seen in Figure 5.13 that the width and height of the bulge does not vary considerably if the outer diameter is changed. The size of the bulge depends on the volume of the heated material, which is almost the same in both cases since the same coil is used in the experiments. On the other side, the rear wall of the large diameter specimens are distorted less. The width of the barreled shape is indicated in Figure 5.13. It is clearly seen that, the nominal values are almost the same for all of the specimens. However, diameter of

the workpiece is considered, it is seen that the ratio of width of the barreled to the diameter is less in the specimens with 40 mm of outer diameter. The discrepancies can be observed in Figure 5.13(e) and (f). The specimens with 40 mm outer diameter, the rear wall maintains its smooth shape.

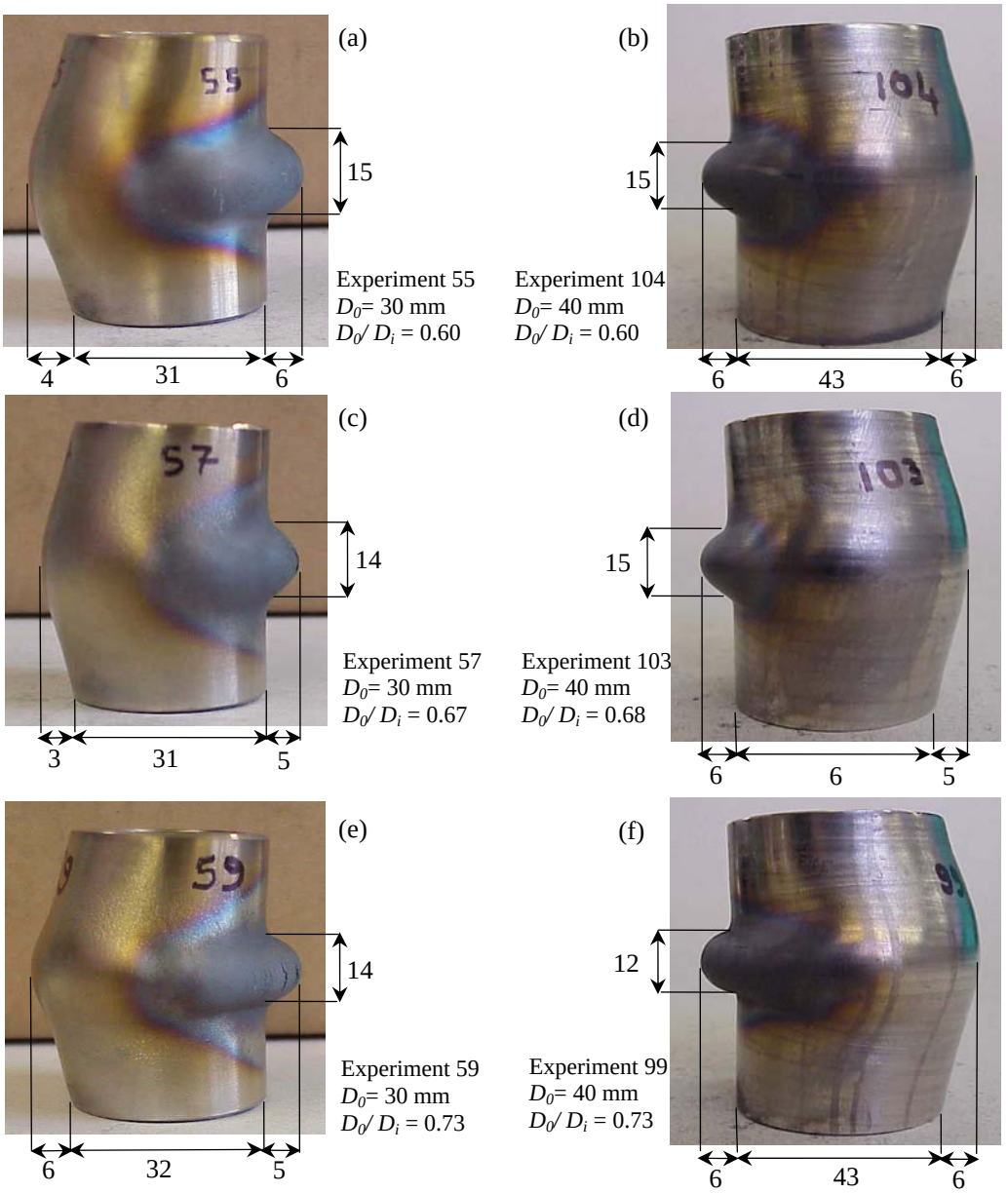

Figure 5.13 Comparison of hollow workpieces with different wall thicknesses.

If the ratio of workpiece diameter to coil diameter is increased, the locally heated area may behave like a plastic hinge. In Figure 5.14, the product of *Experiment 177* is shown. The workpiece tends to rotate around the soft material during forming. The walls of the workpiece adjacent to the heated area have a barreled shape due to the plastic hinge formation. In the workpieces that have 50 mm diameter, the temperature difference between the hottest point in the heated region and side walls is higher than in 30 mm diameter workpieces. Therefore the material does not flow from the side walls to the bulge region. The increase of diameter due to folding creates tensile forces on the bulge area, and hinders material flow outwards from the surface of the specimen. The regular shape of the bulge observed on the 30 mm diameter workpiece is distorted.

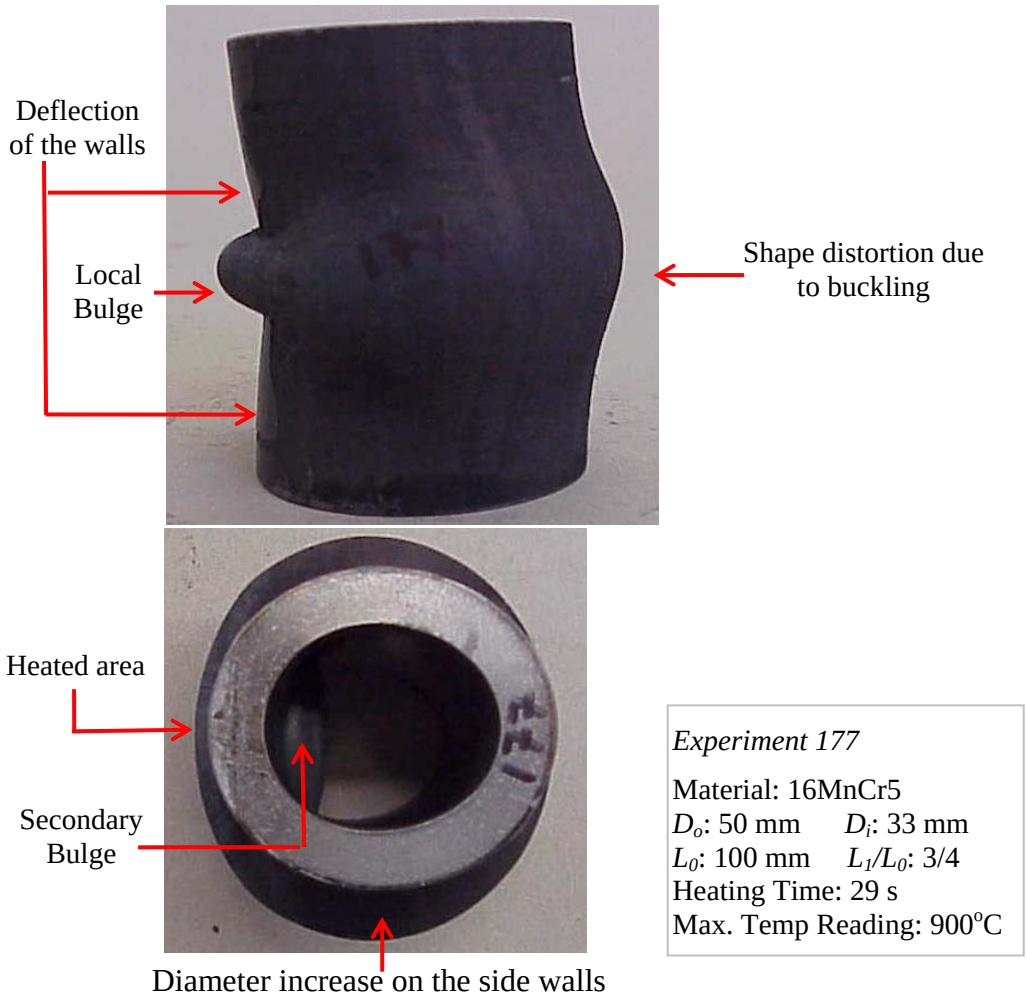

Figure 5.14 Local heating and free forming of workpieces with large diameters.

The workpieces with larger diameters could not be investigated since the press force is not enough to form these specimens.

5.5.4 Effect of Upsetting Ratio

The upsetting ratio is an important parameter of the process. In Figure 5.15, products of selected two experiments, namely *46* and *60*, are shown, which are cut longitudinally and their cross sectional area is etched to make the flow lines visible.

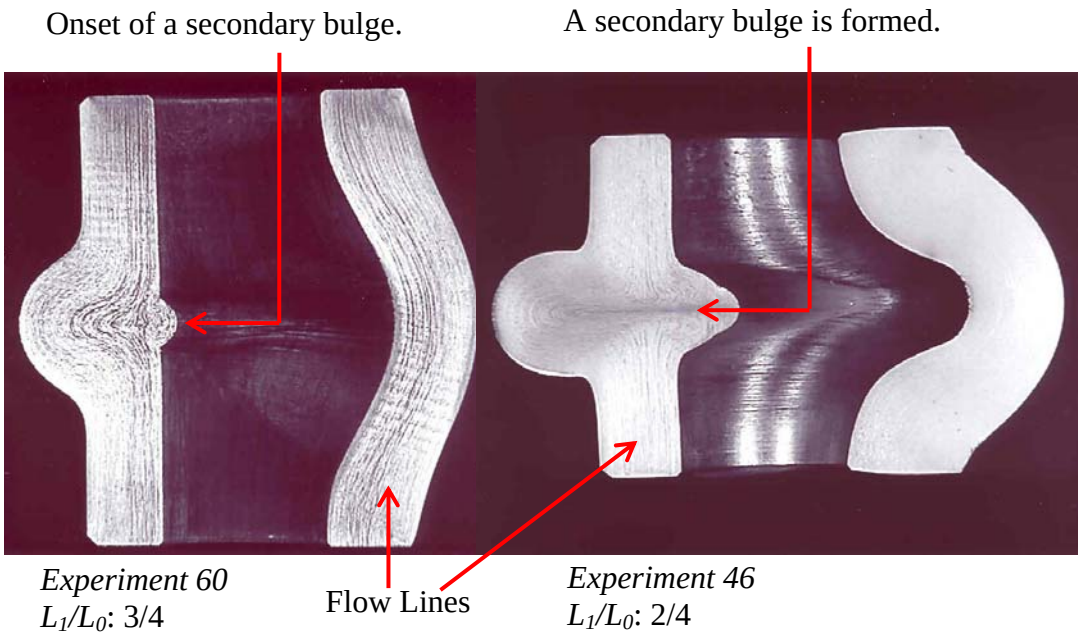

Figure 5.15 Results of *Experiment 60* (left) and *Experiment 46* (right). Heat is generated on the left side.

In those experiments, specimen dimensions and heating parameters are identical. The only difference between the two experiments is the ratio of initial to final length, which is ¼ for *Experiment 60* and ½ for *Experiment 46*. Therefore, *Experiment 60* can be regarded as an intermediate step of *Experiment 46*. As seen in the figure, in the earlier stages of upsetting, material flow on the neighborhood

of the heated zone is directed to the bulge area. The hot material tends to flow outwards, creating a bulge in this zone. Some of the material flows to inside of the hollow specimen. (Figure 5.15(a)). If the punch proceeds further, a second bulge, which is growing to the inside of the hollow specimen, appears (Figure 5.15(b)).

5.6 Failure Modes of the Process

During the process some undesired deformations and failures have been observed. In this section they will be classified and explained.

5.6.1 Buckling

Regarding the major aim of the project, a bulge-type formation is only desired on the heated side. Therefore, the formation of the rear side of the specimens and deflection of the side walls due to buckling can be regarded as a failure. The major causes of buckling and the resulting shape changes are explained in Section 5.5.2.

5.6.2 Crack Formation

In cold upsetting process at room temperature, Ti6Al4V specimens tend to show brittle behavior. As the temperature increases, formability of the material increases. In the local heating process, the unheated regions are relatively cooler than the heated area. As the heat flux increases, the temperature gradient between the surface and the inner parts increases. Also, the total time for the surface layer to reach the desired temperature will be decrease. Therefore, in some experiments, where the surface temperature increases rapidly, the temperature difference between the heated side and the rear side of the workpiece is high and rear side temperature remains close to the room temperature. In the poorly heated rear region

cracks are formed during the upsetting process (Figure 5.16). If through heating is enhanced by increasing the heating time, possibility of cracking will decrease.

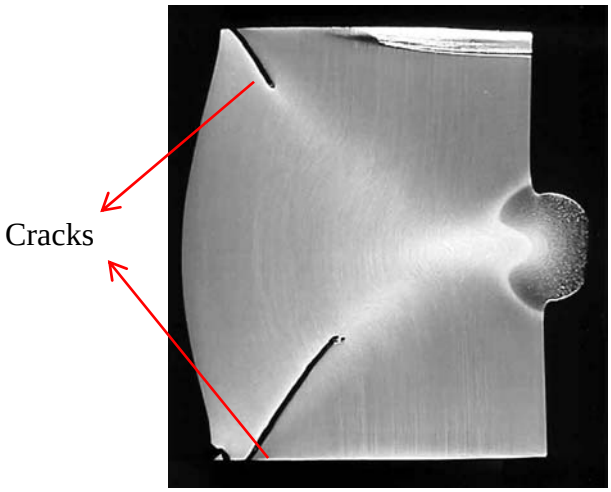

Experiment 140

Material: Ti6Al4V
Max. Temp. Reading: 850^{o}C
D_0= 30 mm L_0= 60 mm
(Solid)

Figure 5.16 Crack formations on Ti6Al4V specimens

At the end of the upsetting process, crack may be observed on the local bulge (Figure 5.17). These are in the vertical direction and formed usually as the workpiece cools down after upsetting.

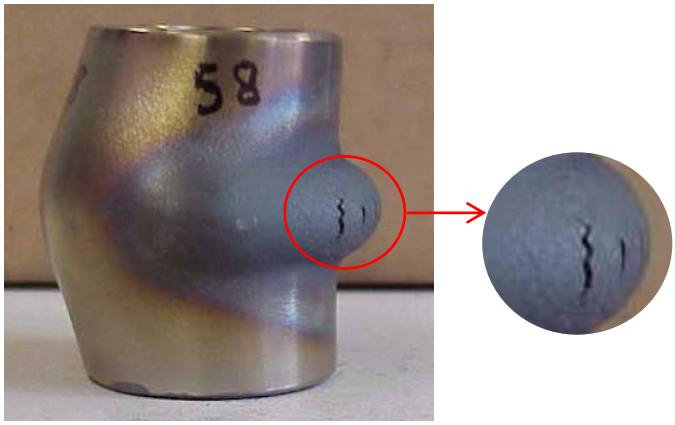

Experiment 58

Material: X5CrNi18 9

Max. Temp.
Reading: 1100^{o}C

Initial Dimensions
D_0= 30 mm
D_i= 20 mm
L_0= 60 mm

Figure 5.17 Surface cracks may be formed on the heated portion of the specimen, after the upsetting process is completed.

5.6.3 Distortion of the Bulge

The walls of the workpiece above and below the heated region may act as a rigid punch moving into the hot material. As the punch moves further, the walls tend to penetrate into the hot volume. This situation results in some undesired affects on the final shape of the bulge. The smooth shape of the bulge may be distorted (Figure 5.18).

Figure 5.18 The walls above and below the heated portion may interfere into the bulge area. Smoothness of the bulge shape is distorted.

The undesired deformation on the bulge area may enhance the possibility of cracking in this region. This situation becomes pronounced as the ratio of final to initial length decreases..

5.7 Conclusion

The experiments presented in this section describe the general aspects of free forming of locally induction heated specimens. The characteristic product shapes and the effect of some process parameters on the material flow are investigated.

It is observed that the heating parameters such as the duration of heating and the amount of heat generation rate have a major effect on the product shape. However,

in case of utilization of identical heating and forming parameters for different materials, completely different products are obtained. The thermal properties of the material play a crucial role in the mode of deformation. The heat diffusion capability determines the temperature gradient within the workpiece and, as a result, the shape and dimensions of the bulge. The investigation is focused on the cylindrical workpieces with 30 mm of outer diameter. However, larger diameter workpieces are also used in the experiments. In the workpieces that have an outer diameter of 40 mm, the distortion of the rear side wall is prevented to a degree, as expected. A systematic investigation of the workpieces with larger diameters could not be carried out due to the limitation of the maximum press force.

It is seen in the experiments that local heating provides ease of manufacturing of complex shapes even in the absence of complicated dies. A further investigation of effect of process parameter is presented in Chapter 8.

CHAPTER 6

METALLURGICAL INVESTIGATION

6.1 Introduction

The microstructure of a metal specimen determines the mechanical and physical properties of the material. The heat treatment procedures applied to the material have direct effect on the microstructure. Heating and successive cooling may introduce changes on the structure of the material. Therefore, it is important to investigate the microstructure of the products if the specimens are heated to elevated temperatures. In this section, the microstructure of the locally induction heated and formed specimens are investigated.

6.2 Investigation of Steel Specimens

6.2.1 Iron-Carbon System

The steels and cast irons are mainly iron carbon alloys. The constituents in the alloy are found as iron (Fe) and iron carbide (Fe_3C). The crystal structure of iron shows variation depending on the heat treatment applied. A portion of the iron-iron carbide phase diagram is shown on the Figure 6.1. In practice, the steels and cast irons have a carbon concentration less than 6.7%; therefore the portion of the phase diagram that lies between 0% to 6.7% carbon concentration is considered in the investigation.

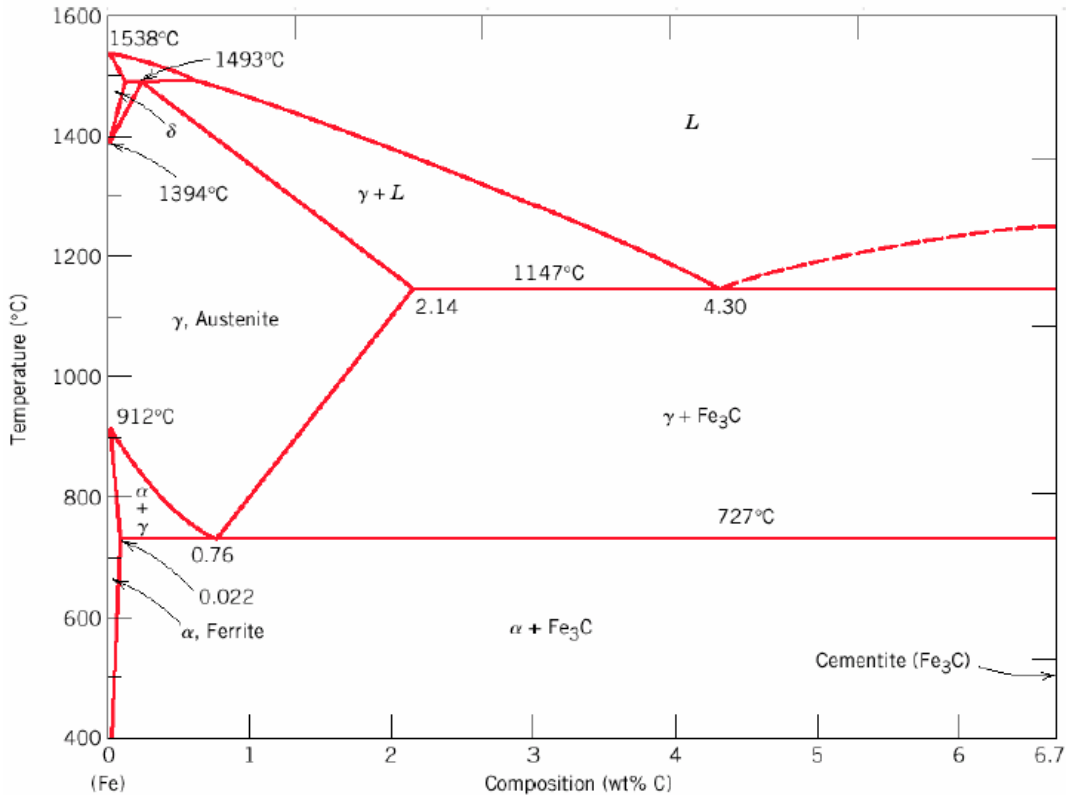

Figure 6.1 The iron-iron carbide phase diagram [17].

The horizontal axis on the phase diagram shows the percentage of carbon in the solution and the vertical axis shows the temperature. In the phase diagram, the cooling rate is slow such that at each temperature the solution is in equilibrium. Therefore, the microstructure of the alloy is dependent only on the concentration of the constituents. The phase change of pure iron is apparent on the left vertical axis of the diagram. The diagram extends to 6.7% of carbon content. At this concentration, the intermediate compound iron carbide (Fe_3C) or *cementite* is formed. The only constituent at this concentration is cementite. Between 0% and 6.7% of carbon concentration, different forms of iron appear, namely, austenite (γ), α ferrite and δ ferrite.

In most of the practical heat treatment applications, specimens are cooled continuously to room temperature. The total cooling time is a crucial parameter that determines the microstructure of the material under the eutectoid temperature. The

diagrams that show the time dependent transformation of the structure in continuous cooling process are the *continuous cooling transformation (CCT) diagrams*. A typical CCT diagram for a eutectoid steel is shown in Figure 6.2.

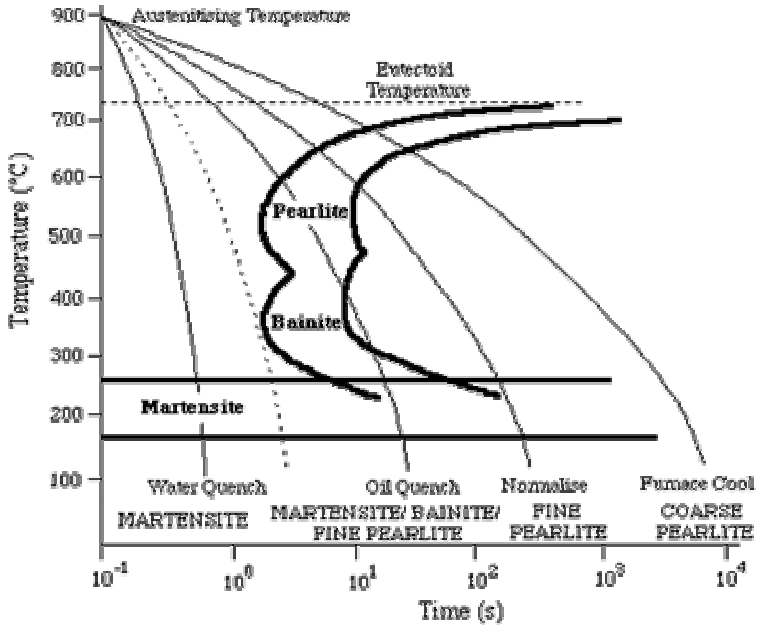

Figure 6.2 Typical CCT diagram for a eutectoid steel [30].

As seen in Figure 6.2, upon cooling of austenite below the eutectoid temperature, different forms of microstructures are formed depending on the concentration and the cooling rate. The iron-iron carbide eutectoid reaction is described by Eq. (6.1)

$$\gamma(0.76wt\%C) \underset{heating}{\overset{cooling}{\rightleftharpoons}} \alpha(0.022wt\%C) + Fe_3C(6.70wt\%C) \qquad (6.1)$$

Pearlite is one of the microstructural products formed during cooling of austenite below the eutectic temperature. It consists of alternating layers of the two phases, namely, ferrite (α) and cementite (Fe_3C). The thickness of the two phases influences the material behavior of the material. Fine pearlite is harder and stronger than the coarse pearlite. Ferrite-pearlite structure is shown in Figure 6.3(a).

Bainite, have a finer structure than that of the pearlite. It is formed in cases for which the isothermal transformation temperature is lower than that is needed for

formation of pearlite. It is harder and stronger than pearlitic structures. However, the strength and ductility of the material is appropriate in for many cases. Ferrite-bainite structure is shown in Figure 6.3(b).

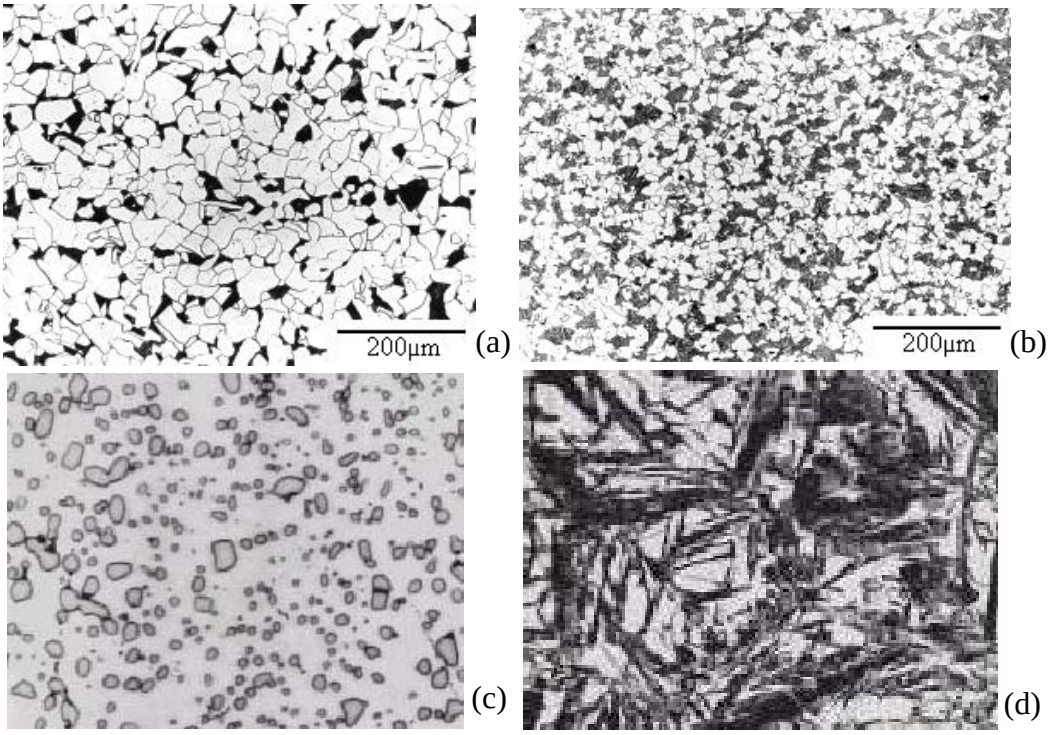

Figure 6.3 Photomicrograph of (a) ferrite-pearlite (b) ferrite-bainite [31] (c) spheriodite (d) martensite [17].

Spheriodite is obtained when either a pearlitic or bainitic structure is heated to a temperature below the eutectoid temperature and left at this temperature for a sufficiently long period of time. The structure is seen as sphere like particles of Fe_3C embedded in a continuous ferrite (α) matrix. Its strength and hardness is less than that of pearlitic structures. Its toughness is considerably higher than pearlite. Spheriodite structure is shown in Figure 6.3(c).

Martensite is formed as a result of rapid cooling of austenite to low temperatures. In formation of this structure, carbon is not diffused in the material since the process time is short. Martensite is obtained in case of high quenching rate. It is the

hardest, strongest and the most brittle of all the microstructures produced in a steel alloy. Martensite structure is shown in Figure 6.3(d).

6.2.3 Investigation of Experiment Specimens

The microstructural investigation of a 16MnCr5 specimen is presented in this section. The composition of the alloy is given in Table 6.1.

Table 6.1 Chemical composition of 16MnCr5 [32].

Element	C	Mn	Cr	Si	P	Fe
Weight (%)	0.16	1.15	0.95	0.25	0.035	BAL

The microstructure of the material is investigated in some critical sections. The structure is determined by using the continuous cooling diagram (CCT) and the comparing the appearance with the known structures. The CCT diagram for 16MnCr5 is given in Figure 6.4. In the CCT diagram, the Vickers hardness values and the percentage of constituents are also given for some cooling cases.

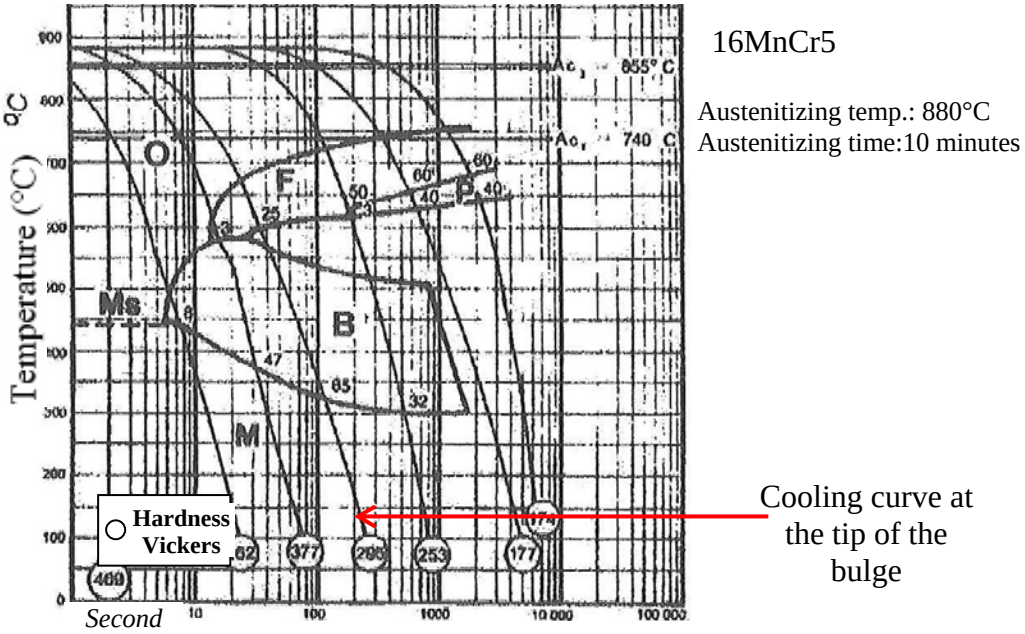

Figure 6.4 Continuous cooling diagram of 16MnCr5 [33].

The specific experiment selected for the investigation is *Experiment 84*. The cross sectional view of the local bulge and locations selected for microstructural investigation in the bulge area are shown in Figure 6.5.

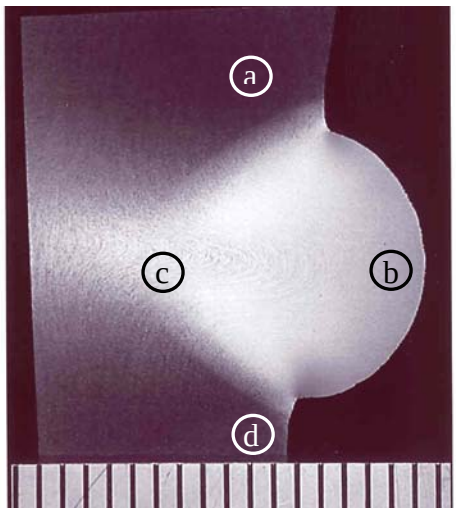

Figure 6.5 The local bulge of a solid16MnCr5 specimen.

The microstructure of the regions (a) and (d) are shown in Figure 6.6. The maximum temperature is this region is about 700°C. The structure in these regions is banded ferrite-pearlite. The presence of manganese in the composition causes the ferrite and pearlite phases appear in form of thin bands.

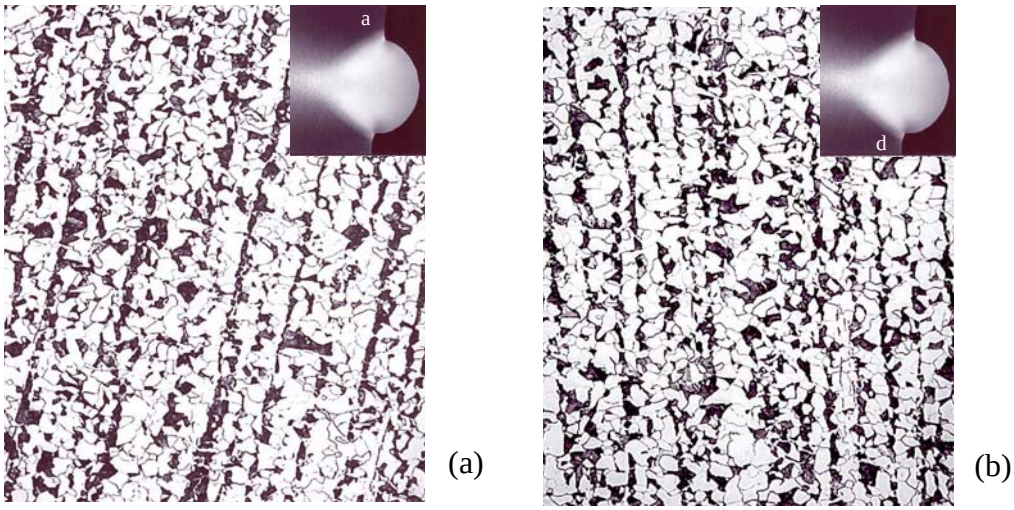

(a) (b)

Figure 6.6 The microstructure in regions (a) and (d) in 16MnCr5 specimen (x180).

The microstructure on the tip of the local bulge is presented in Figure 6.7(a). The hardness on the tip of the bulge is 297 VH/0.5. This value is very close the hardness value obtained in the cooling case indicated in Figure 6.4(a). The structure in this portion consists of bainite and ferrite. A fine structure is formed as a result of rapid cooling in this region due to convective heat transfer and conduction within the workpiece. The microstructure of the region represented as (c) in Figure 6.5 is shown in Figure 6.7(b). The grains in this region are elongated due to deformation. They are oriented in the direction of material flow. The microstructure in this region is ferrite-pearlite.

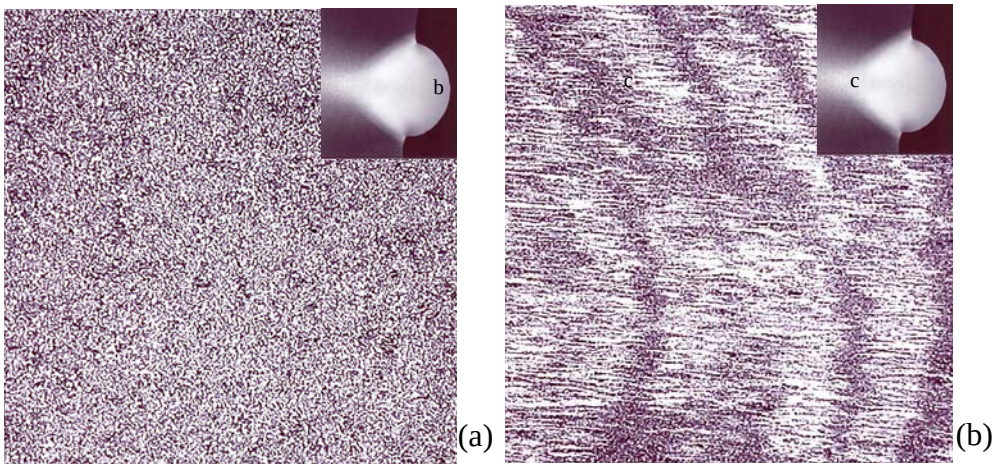

(a) (b)

Figure 6.7 The microstructure in regions (b) and (c) in 16MnCr5 specimen (x180).

The Vickers hardness measurements taken at the bulge area of the 16MnCr5 specimen is given in Figure 6.8. The values are recorded on two different paths around the bulge area. The maximum hardness value is recorded at the tip of the bulge. In this region, a finer structure is observed due to rapid cooling of the material and this structure has a higher hardness value as expected. A decreasing trend is observed in the hardness values on the path extending the radial direction. As seen in Figure 6.8(b), the hardness is higher around the bulge region compared to the regions above and below the heated region.

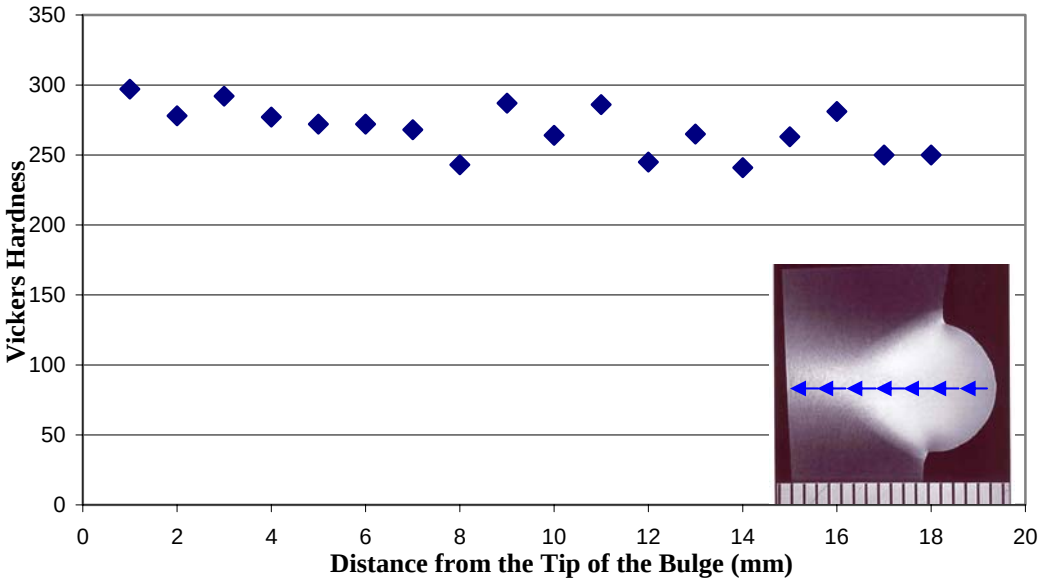

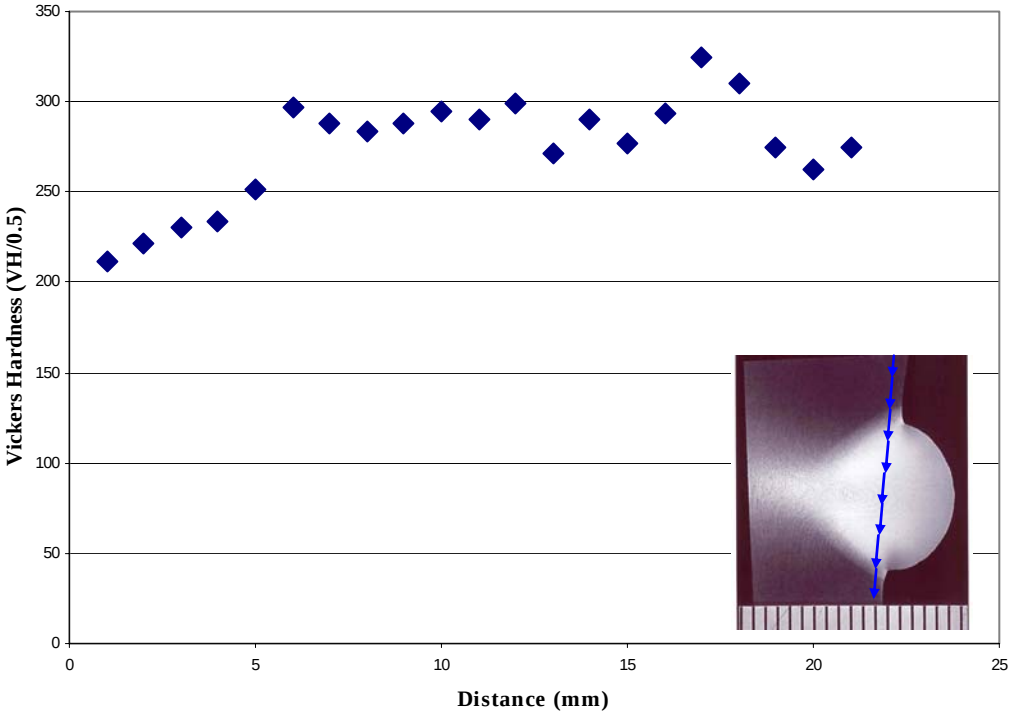

Figure 6.8 Hardness values of the cross section of the 16MnCr5 specimen.

6.3 Investigation of Ti6Al4V Specimens

6.3.1 Properties of Titanium and Titanium Alloys

Titanium and its alloys are used in many applications due to their resistance to corrosion and high strength to weight ratio. Purity of titanium ranges from 99.5 to 99.0%. The main alloying elements are O, Fe, C, N. The interstitials decrease toughness; therefore if low toughness is desired, alloy is produced with extra-low-interstitials (ELI).

Pure titanium has two allotropic forms, namely, α and β phases. The α phase has hexagonal close packed structure and is observed at temperatures below 883°C. This temperature is called the *Beta Transus Temperature*, above which value the material has a body centered cubic structure. This phase observed at elevated temperatures is called the β phase.

The alloying elements have effect on the transition temperature. The alloying elements are divided into two main groups regarding their effects of the beta transus temperature. They are the α stabilizers and β stabilizers. Addition of α stabilizers, such as Aluminum and Tin, to the alloy increase the β transus temperature. On the other side, β stabilizers, like Vanadium, Molybdenum, Chromium, and Copper, decrease the beta transus temperature. The titanium alloys are grouped as α alloys, β alloys and α+β alloys depending on the elements in the alloy [34].

Ti6Al4V is a type of α+β alloy, since it contains aluminum and vanadium, which are α and β stabilizers, respectively. The chemical composition of Ti6Al4Vn specimens used in the experiment is supplied by the manufacturer and is given in Table 6.2. It is the most widely used of all the titanium alloys. The heat treatment of Ti6Al4V is shown by three examples, in which the cooling starts from 1066°C, 945°C, and 843°C. The schematic representation of cooling is shown in Figure 6.9.

Table 6.2 Chemical composition of Ti6Al4V.

Element	C	Fe	O	N	H	Ti	Al	V
Weight (%)	<1	17	16	<1	1	BAL	615	412

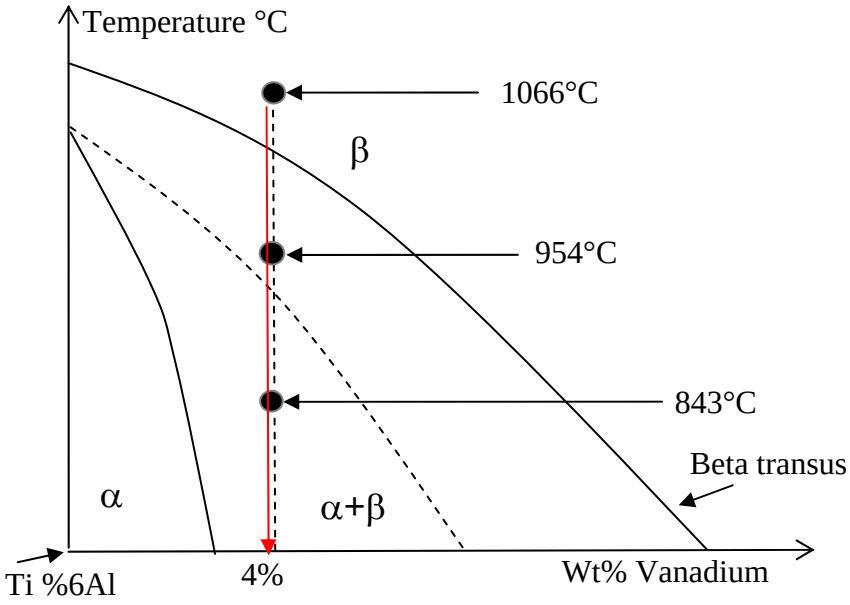

Figure 6.9 Schematic representation of heat treatment of Ti6Al4V. Cooling process starts from (a) 1066^{o}C (b) 954^{o}C (c) 843^{o}C [34].

Ti6Al4V exists in β phase at 1066°C. If the material is cooled slowly (furnace cooling), the resulting microstructure is a mixture of α and β phases. The alpha phase and the intergranular beta phase are seen in Figure 6.10(a). If fast cooling is applied at 1066°C (water quenching), the α' phase is formed, which is also called titanium martensite. The microstructure obtained is presented in Figure 6.10(b). The ultimate tensile strength of the titanium martensite and α+β phase are about 1100 MPa and 1030 MPa, respectively.

If cooling process is started from 945°C, the structure retains the alpha and beta structure in case of slow cooling (furnace cooling). If the faster cooling rate is applied such as water quenching, titanium martensite is formed together with alpha

(α) and beta (β) grains. The microstructures obtained in case of fast and slow cooling are presented in Figure 6.11.

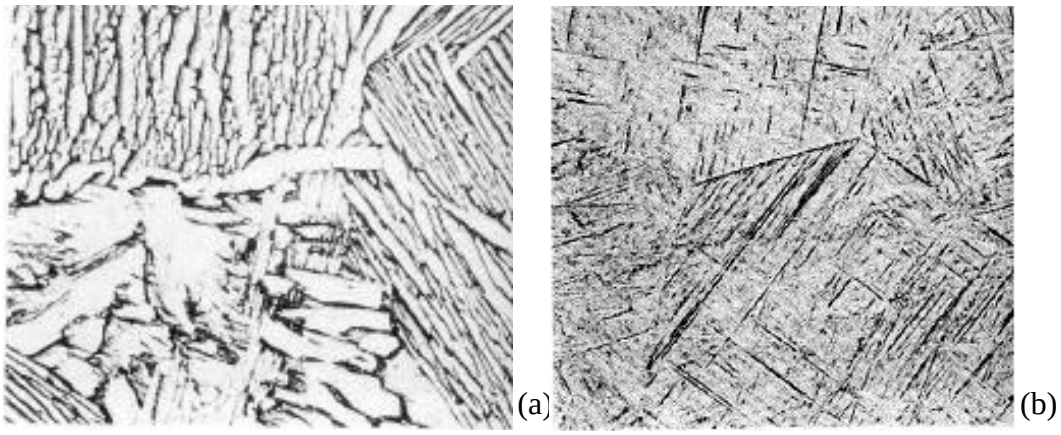

Figure 6.10 The microstructures obtained by cooling Ti6Al4V specimens from 1066°C by (a) furnace cooling (b) water quenching [34].

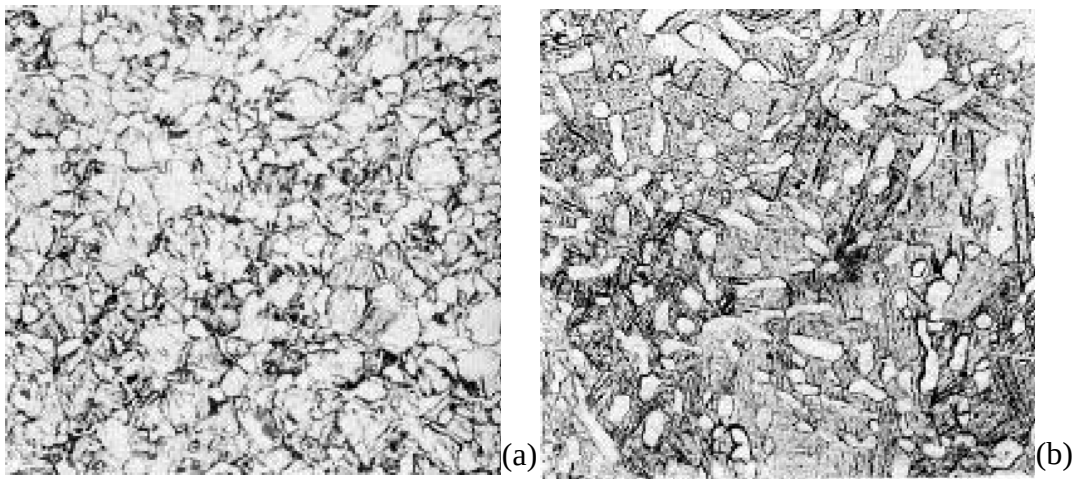

Figure 6.11 The microstructure obtained by cooling from 843^{o}C in case of (a) air cooling (b) water quenching [34].

The end product of cooling from 843^{o}C is a mixture of α and β phases as the initial stage. If the air cooling is applied, the primary α+β phase is preserved. In case of water quenching, the final structure is a composition of α and retained β phase. The microstructure obtained in case of water quenching is shown in Figure 6.12.

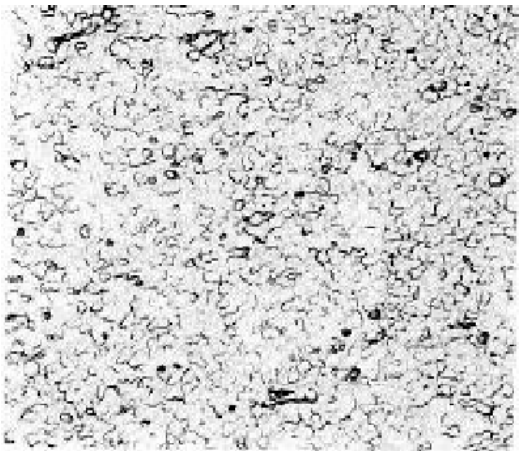

Figure 6.12 The microstructure obtained by water quenching from 843^{o}C [34].

6.3.2 Investigation of Experiment Specimens

The specific experiment selected for the investigation is *Experiment 140*. The magnified view of the bulge area is presented in Figure 6.13. The investigation zones are selected from the relatively less heated parts above and below the heated section (region (a) and (d)), on the tip of the bulge (region (b)) and inside the specimen behind the local bulge, in which the high amount of deformation takes place (region (c)).

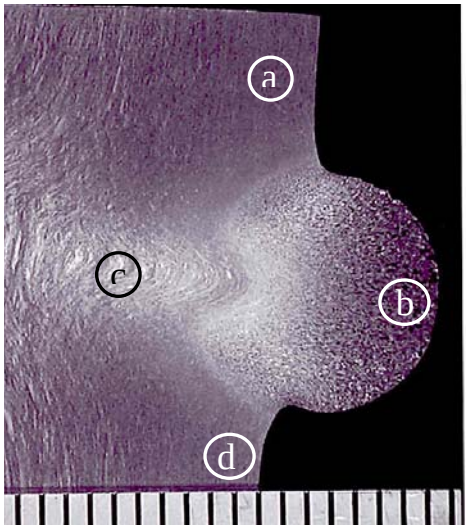

Figure 6.13 The local bulge of a solid Ti6Al4V specimen.

The microstructure of the regions (a) and (d) are shown in Figure 6.14. The structures in these regions are is alpha-beta phase. The maximum temperature in these regions is 750°C and no phase transformation occurs during the process.

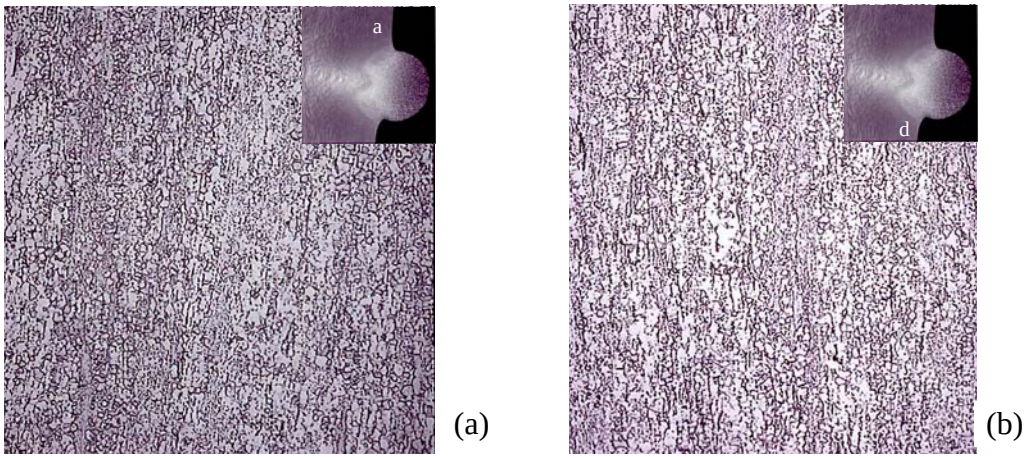

(a) (b)

Figure 6.14 The microstructure in regions (a) and (d) in the Ti6Al4V specimen.

The microstructure of the region (b) is shown in Figure 6.15(a). The tip of the bulge reaches to about 900°C during heating and experiences rapid cooling during due to air convection and conduction within the workpiece. The structure in this region looks similar to titanium martensite (α'). However, since the specimens are air cooled, it is more probable that titanium martensite is not formed.

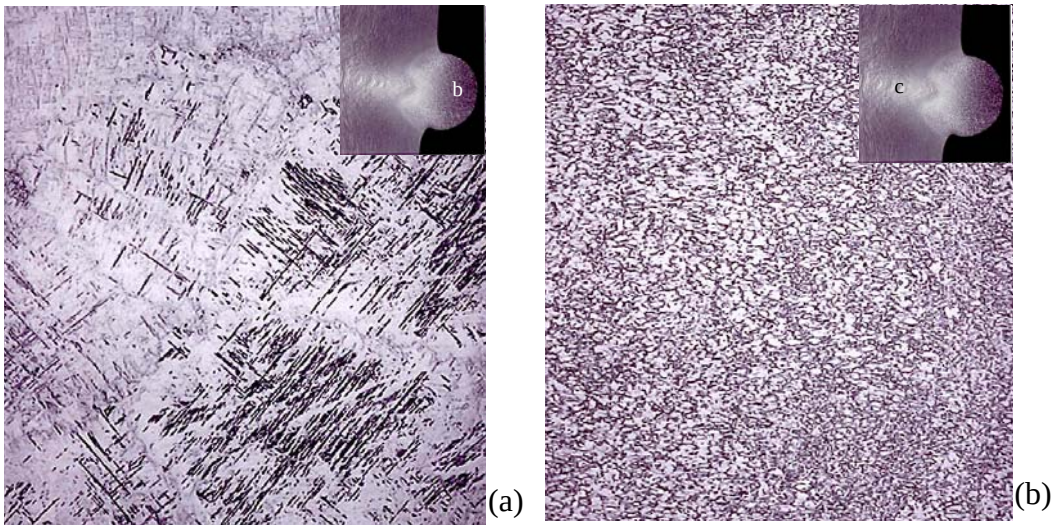

(a) (b)

Figure 6.15 The microstructure in regions (b) and (c) in Ti6Al4V specimen (180x).

The microstructure on the region (c) is shown in Figure 6.15(b). The structure in this region is alpha beta. At the end of heating, the average temperature in this region is between 250°C and 300°C. The shape of the grains in this region is slightly elongated and they are directed toward the local bulge.

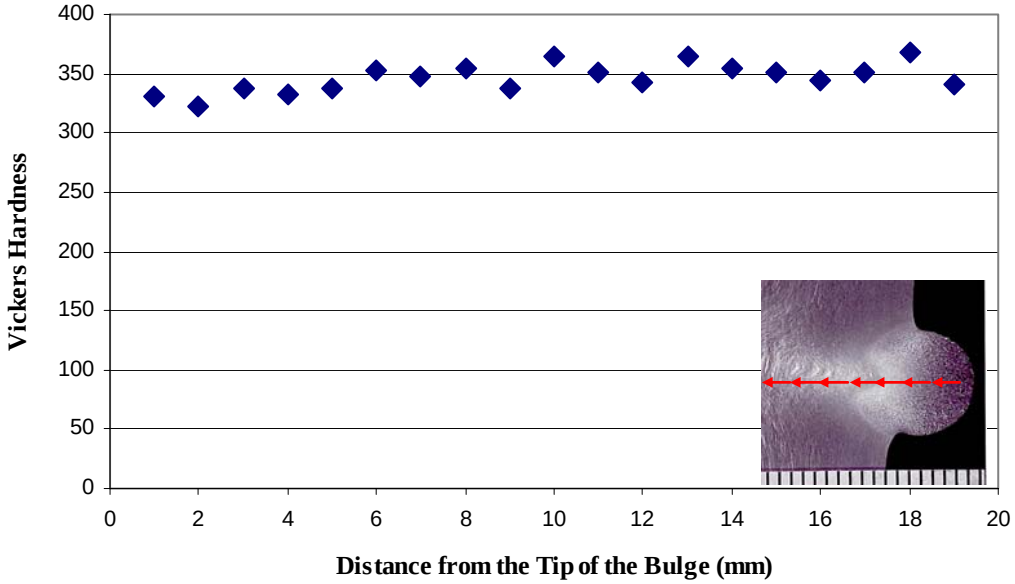

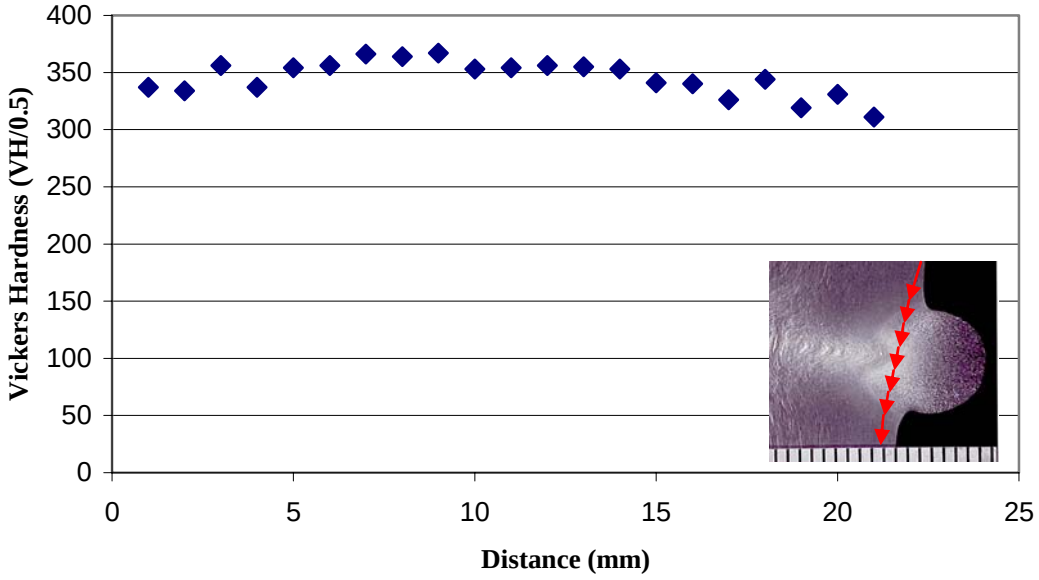

Figure 6.16 Hardness values of the cross section of the Ti6Al4V specimen.

The Vickers hardness values taken around the local bulge area of the Ti6Al4V specimen is given in Figure 6.16. The values are recorded on a path that starts from the tip of the bulge and extends in the radial direction and parallel to the wall of the specimen. The hardness values do not show considerable variance on these paths.

6.4 Conclusion

The physical properties of the specimens depend directly on the heat treatment applied during manufacturing. Especially the critical points, at which it is likely to observe failure during service conditions, should be investigated. The microstructural investigation of the products is a useful tool in determining the strength of the product and detecting probable defects.

It is observed in the investigation of the locally heated and formed specimens that the microstructure shows differences around the bulge region. On the neighborhood of the local bulge the grain size is reduced due to heating and the subsequent rapid cooling. However, there is no considerable variation of the hardness values since water or oil quenching is not applied to the workpieces.

In further applications of local heating in forming, the product quality should be tested in the microstructural level. The yield stress values should be deduced by available techniques. The frequency of heating and cooling rate can be adjusted such that required amount of material can be hardened in order to meet the desired product properties.

CHAPTER 7

NUMERICAL ANALYSIS OF INDUCTION HEATING PROCESS

7.1 Introduction

The electromagnetic field created around a current carrying coil and the corresponding current generation on the neighboring metal substances can be simulated by means of finite element analysis (FEA). The governing equations of the electromagnetic field analysis are given in Section 3.5. The amount of heat generation on the workpiece due to current flow can also be calculated by this method. In this study, rate of heat generation on the workpiece is calculated by using the software ANSYS 7.0. The issues of numerical modeling and the results of the simulations are demonstrated in this section.

7.2 General Aspects of the Analysis

In the numerical analysis of induction heating, the current carrying conductor, the workpiece that is affected by the electromagnetic field and the surrounding air are modeled. In case of local heating the heat generation within the workpiece is not axisymmetric. Therefore, a 3D model is constructed to simulate the electromagnetic field and the corresponding heat generation.

In the experiments, an alternating current passing through a coil causes heat generation in the surrounding conductors. This situation can be simulated by carrying out a *harmonic analysis*. This means that the current applied has a sinusoidal nature with a certain frequency (ω) and amplitude. The data obtained such as the heat generation rate, induced current distribution, etc. are out-of-phase with the input source loads and therefore they are complex in nature. Two sets of solutions are provided at the end of an analysis. The results are calculated and stored in terms of real and imaginary components, that describe a measurable field at the $t=0$ and $\omega t=-90$ degrees, respectively. The symbol t indicates the time and ω denotes frequency of the alternating current.

7.2.1 Modeling and Meshing

The actual coil and workpiece is shown in Figure 7.1(a). In the numeric model, the coil is represented as two concentric circles Figure 7.1(b). Considering the model, the heating patterns on the workpiece will be symmetrical with respect to the horizontal and vertical planes passing through the center of the concentric coils. Therefore, it is sufficient to calculate the electromagnetic field and the corresponding heat generation only for one quarter of the coil-workpiece set up Figure 7.1(c).

In the simulations, only one quarter of the set up is used. The variations of distribution of heat generation in the experiments, due to the minor geometrical irregularities of the actual coil are neglected. There is not a considerable deviation of the calculated results from actual distribution of heat generation. The computational effort is minimized since the total number of elements required is decreased by 75% in the quarter model.

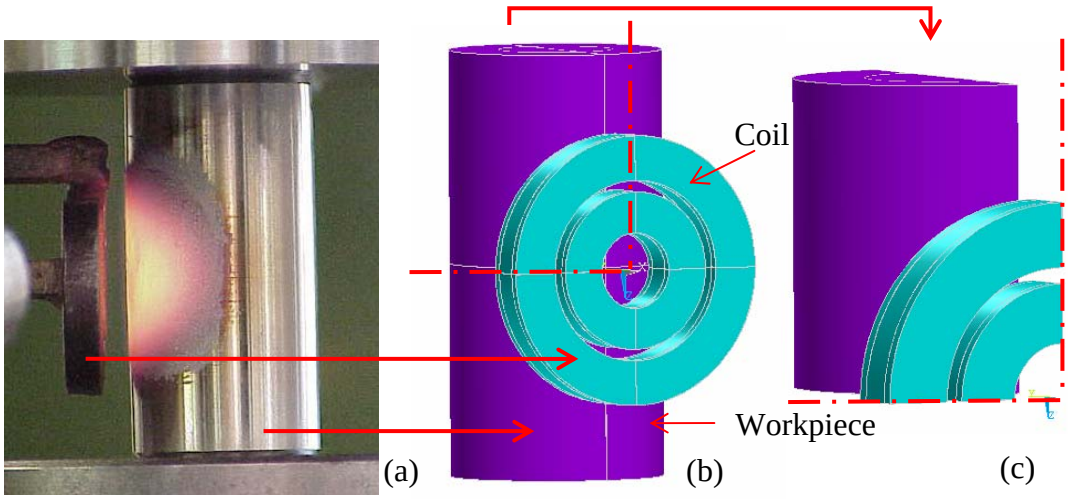

Figure 7.1 (a) The coil and workpiece. (b) The idealized geometry of the coil and workpiece. (c) The quarter of the model that is used in the calculations.

The meshed bodies are presented in Figure 7.2(a). The surrounding air is modeled as a rectangular prism that circumscribes the coil and the workpiece as seen in Figure 7.2(b). The dimensions of the prism are determined arbitrarily; however some constraints are regarded. The sizes should be large enough for the magnetic field to be weak at the boundaries [35]. It is advised that the length of the prism should be at least 2 times larger than the maximum dimension of the workpiece [23]. The height of the prism is determined as 38 mm, which is two times the maximum coil diameter (19 mm). The total width of the air column is 43 mm, which provides sufficient space around the coil. This value is also more than twice the radius of the workpiece. The critical dimensions of the model are given in Figure 7.2(b).

The coil and the workpiece are meshed by using hexahedral elements. Due to the geometry of the model, it is impractical to mesh the air with hexahedral elements. Therefore, tetrahedral elements are preferred in meshing the air sections. The two types of elements are compatible with each other. Utilization of tetrahedral elements together with hexahedral elements is a widespread application and has many successful examples in literature [36].

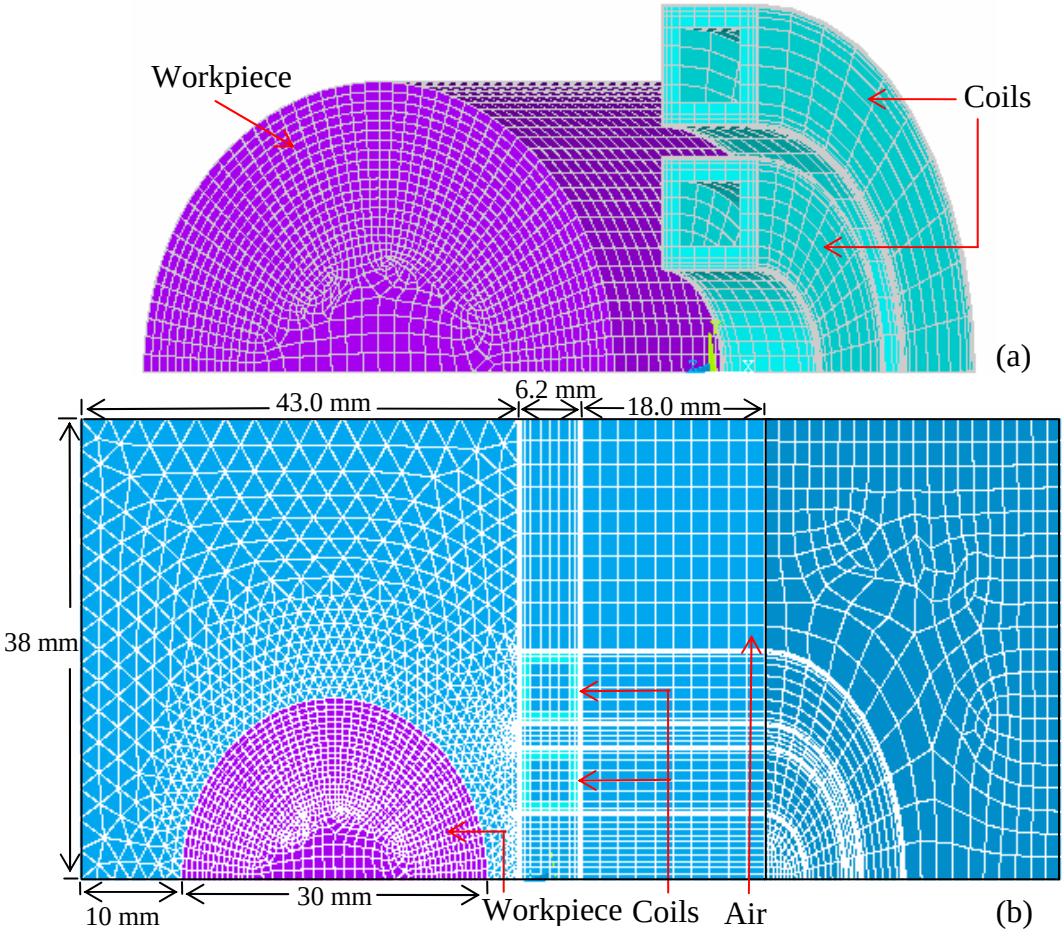

Figure 7.2. The numerical model used in electromagnetic field calculations. (a) The coil and workpiece (b) The entire model.

As seen in Figure 7.3(a), the real coil has a helical shape and the number of turns is 2. In the model, however, two concentric circular coils are used in place of the helical coil (Figure 7.3(b)). Those models of the coils have the same dimensions on average as their counterparts on the real coil. It is proposed that if same amount of current passes through each of the two circular coils, the actual heating case is adequately simulated. The advantage of the idealized coil geometry is that it provides ease of drawing and meshing and the symmetry conditions become applicable.

During heating the coil is also heated. Excessive heat is moved away by means of water flowing inside the coil. As seen in Figure 7.3(c), the water channels are

modeled; however, cooling is not simulated since coil temperature is not critical in this study. On the other side, the coil geometry is preserved in order to obtain the actual current distribution on the cross sectional area of the coil.

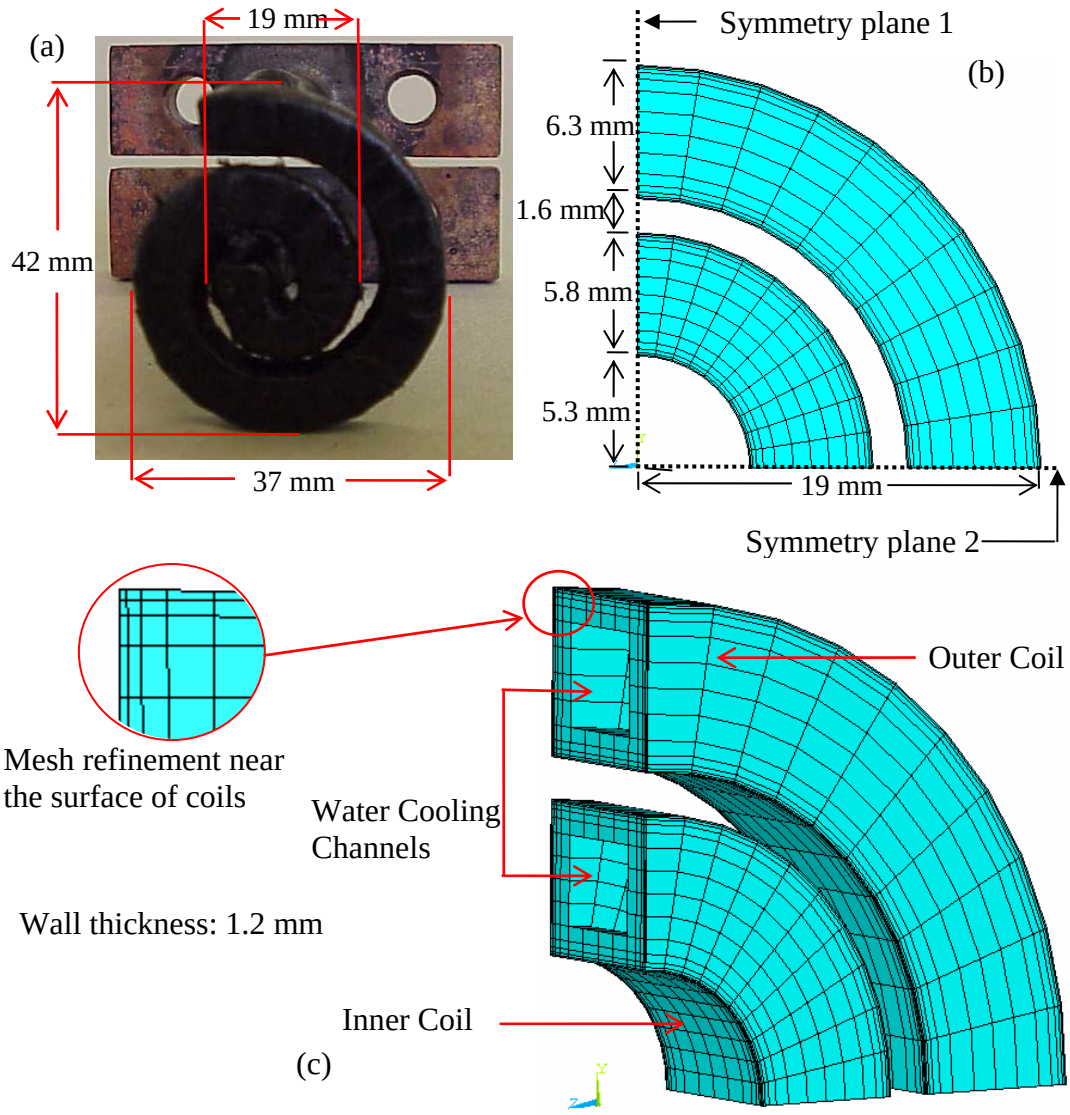

Figure 7.3 (a) The helical induction coil. (b) The idealized coil geometry (c) Details of the model.

The most important parameter of numerical models for electromagnetic field simulation is the edge length of the elements in the neighborhood of the conductor surfaces, in the direction of surface normal. In other words, the width of the elements near the surface has a crucial importance in reliability of the results. The

edge length must be smaller than the skin depth calculated for a certain application. As indicated in Section 3.4.1, the majority of the current will be induced within the skin depth in the workpiece. Also, the current distribution within the coil is mainly determined by the skin depth calculated for the coil. Therefore, if the edge length of an element in the direction of surface normal exceeds the skin depth value in the neighborhood of the specimen surface, incorrect results are obtained. It is advised that the minimum edge length of the surface elements should stay below the skin depth value calculated for a certain specimen.

7.2.2 Selection of Element Type

The element type used in the simulations is named as “SOLID117” in ANSYS 7.0 (Figure 7.4). It is capable of modeling three-dimensional magnetic fields and is defined by 20 nodes. The pyramid option in Figure 7.4 is used as a transition element between the hexahedral and tetrahedral elements. It has 12 edge-flux degree of freedom, one at each midside node.

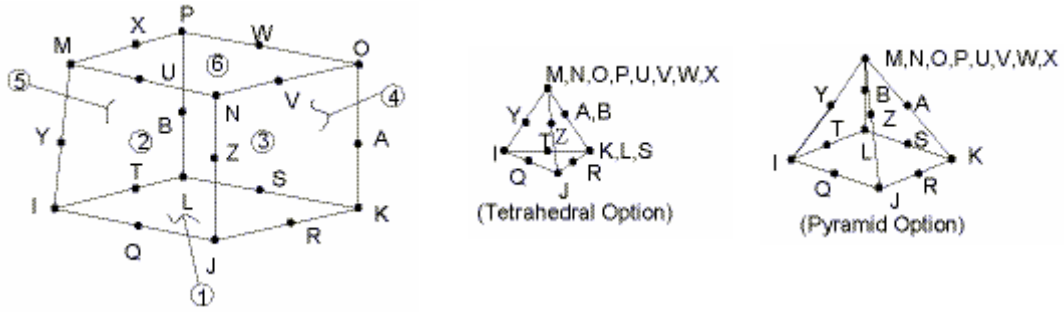

Figure 7.4 The element used in electromagnetic calculations [23]**.**

The edge-flux degree of freedom is the integral of the tangential component of the vector potential along the element edge. Physically, if the values of the flux are summed around a closed loop formed by the edges, the flux passing through the closed loop is obtained. The edge-flux is expressed as units of Weber (Volt-s) in

the MKS system. Electric scalar potential volt degree of freedom may be added at the corner nodes in harmonic and dynamic analyses. For the nodes of coil and workpiece, volt degree of freedom is defined since the current flow and the heat generation is simulated. However, for the nodes of surrounding air it is not defined. SOLID117 is based on the edge-flux formulation, and can be used in the low-frequency magnetic field analyses [23].

7.2.3 Boundary Conditions

Boundary conditions applied on the surface nodes of the model are illustrated in Figure 7.5. On the areas of the workpiece that are coinciding with the symmetry planes, the volt degree of freedom of the nodes is set to zero. This condition indicates that there is no net build up of potential within the body. For the coil, nodes in the cross sectional areas, which are on one of the symmetry planes, are selected and their volt degree of freedom are assigned to zero. The total coil current is applied on a single node on the cross sectional areas, which coincide with the *other* symmetry plane. The volt degree of freedoms of all the nodes on each of these areas are coupled. Coupling degrees of freedom into a set causes the results calculated for one member of the set to be the same for all members of the set. Therefore, in the simulations, there will be no potential difference on those areas. The constraints applied to the coil, simulate a short-circuit condition with a net current flow from a current source generator. The surroundings do not affect the net current [23].

The edge-flux degree of freedom of all the nodes on the external surface of the numerical model, including coil, workpiece and air, are set to zero. This condition satisfies the parallel orientation of the magnetic flux lines to those surfaces, which is the case in reality.

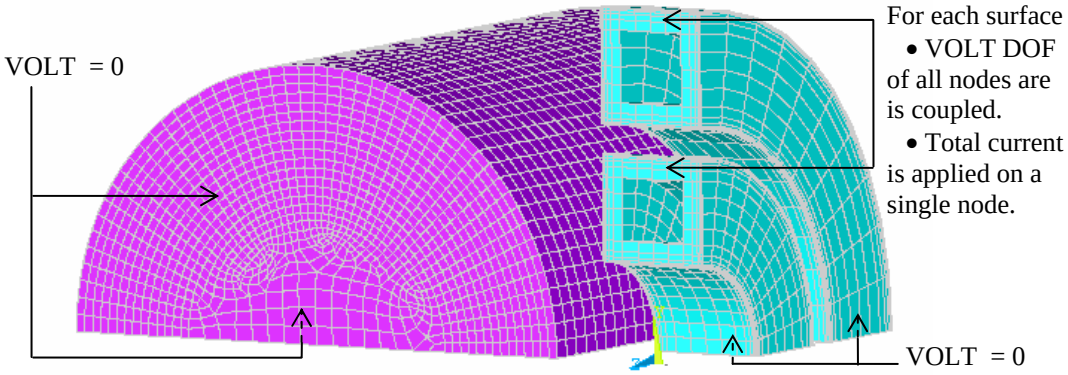

Figure 7.5 The boundary conditions on the symmetry planes.

7.2.4 Material Properties

The material properties needed for the electromagnetic analysis are the magnetic permeability and the electrical resistivity. These values remain constant during an analysis. The magnetic permeability and electrical resistivity values of 16MnCr5, X5CrNi18 9 and Ti6Al4V, which are used in the simulations, are presented in Table 7.1. X5CrNi18 9 and Ti6Al4V are non ferromagnetic materials; therefore they have a relative permeability that is very close to unity. On the other side, 16MnCr5 is a ferromagnetic material and its relative permeability is dependent on the magnetic field intensity and temperature. At temperatures above Curie temperature (about 750°C), the material becomes nonmagnetic. During the analysis, the heated volume has a temperature above the Curie temperature, in later stages of heating. Therefore, the relative permeability of 16MnCr5 is set to unity in the electromagnetic calculations. A more precise analysis of heat generation can be done by coupled electromagnetic analysis.

Table 7.1 The relative permeability and electrical resistivity at room temperature.

	16MnCr5 [37]	X5CrNi18 9 [27]	Ti6Al4V [38]
Electrical Resistivity (Ohm.m)	1.6×10^{-7}	7.2×10^{-7}	1.78×10^{-6}
Relative Magnetic Permeability	1	1.008	1.00005

7.3 Interpretation of the Results

7.3.1 Evaluation of Reliability of the Results

At the end of an analysis, the distribution and direction of some vector quantities like current density, magnetic field intensity (**H**), magnetic flux intensity (**B**) can be obtained as well as the scalar quantities like power generation rate. By evaluating distribution and magnitude of these quantities, the nature of the process is understood. However, before drawing conclusions on the process, the reliability of the results should be evaluated.

As explained before, the edge length of the elements near the conductors' surfaces is an important factor that determines the accuracy of the results. For the workpiece the depth of elements near the surface is 0.5 mm. The elements on the neighborhood of the coil surfaces vary on the cross sectional area of the coil (Figure 7.4(c)). The depths of the first two rows of elements are 0.056 mm and 0.099 mm, respectively. The skin depth values for each of the materials are given in Table 7.2 for the two frequency values used in the experiments. Considering the values in the table, for every case, there is at least one element within the skin depth. From this point of view, the model is satisfactory in simulating the induction heating process.

Table 7.2 The skin depth values

	Material	**Frequency (Hz)**	**Skin Depth (mm)**
Coil	Copper	7800	0.236
	Copper	10500	0.204
Workpiece	X5CrNi18 9	7800	1.523
	X5CrNi18 9	10500	1.313
	Ti6Al4V	7800	2.404
	Ti6Al4V	10500	2.072
	16MnCr5	7800	0.721
	16MnCr5	10500	0.621

In Figure 7.6 the current density distributions on the coil and the workpiece are presented. In order to provide ease of visualization, the coil and workpiece are drawn separately. The direction of the vectors, indicate the direction of current flow. As seen in Figure 7.6(a), those lines are perpendicular to the cross sectional area of the coil on the symmetry plane, and they remain perpendicular to coil's cross area at every point along the coil. The current flow is concentrated near the outer surface of the coils due to the skin effect. However, in the inside of the surface of the coils, current flow is observed in the reverse direction. This is induced as a reaction to the magnetic field created around the coil. The magnitude of the flow is at most about 15% of the maximum value of current density.

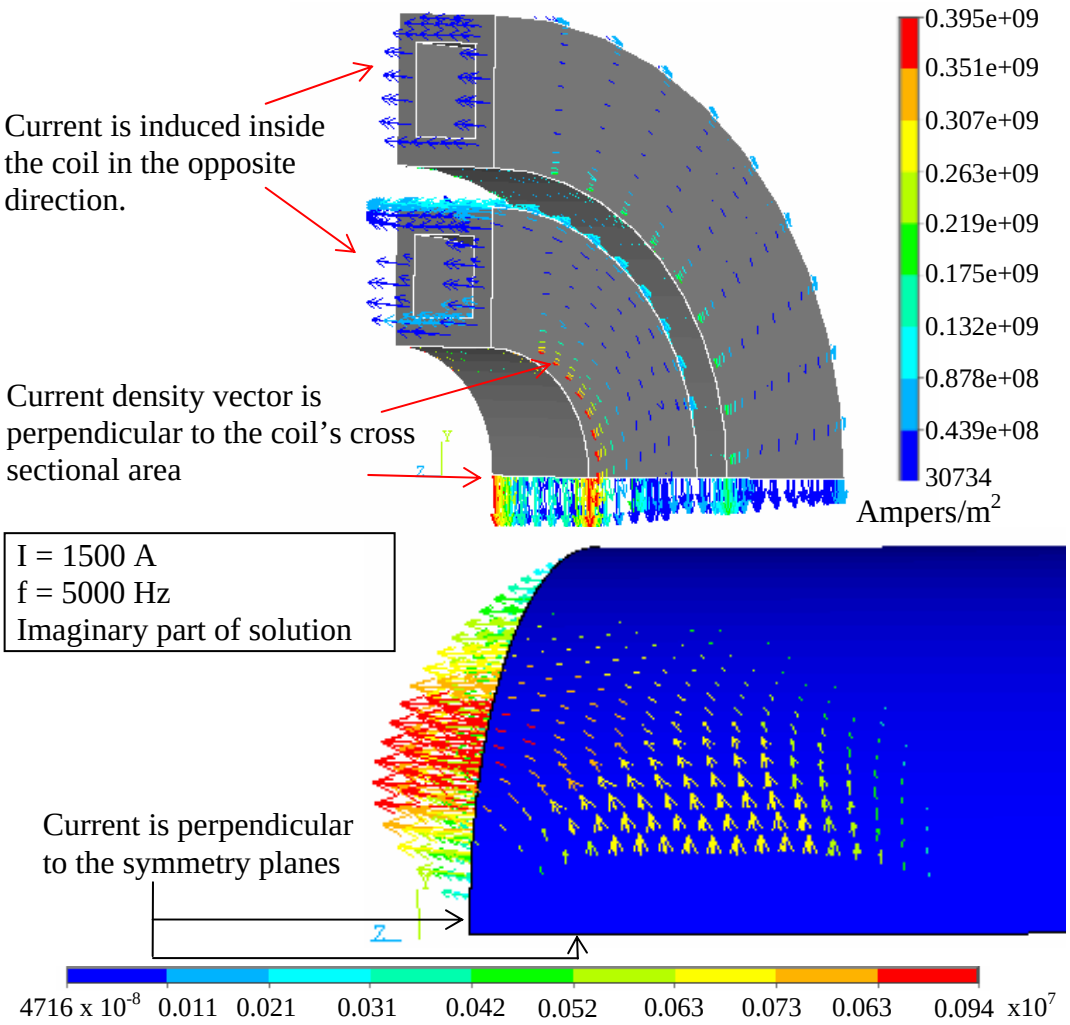

Figure 7.6 (a) Distribution of current density on the coil. (b) Induced current density distribution on the workpiece.

When the current density distribution on the workpiece surface is investigated in Figure 7.6(b), it is seen that the path of current flow resembles the path of coil current. However, the directions of the current density vectors are opposite to that of the applied current. Addressing to the fact that the current flow is induced in the neighboring conductions in order to *oppose* the effect of the created magnetic field, the current density distribution on the workpiece is as expected.

The dimensions of the air block around the set up should be large enough such that the magnetic field is weak on the surface of the block. It is necessary for the boundary condition applied on the outer surface of the air block, which indicates that the magnetic flux is parallel to the surface, to be valid. The value of the magnetic field density (**B**) on the edge surfaces of the prism describing the surrounding air does not exceed about 3% of the maximum value of **B** near the coil. It is proved that the parallel flux condition on the surface nodes of the air is valid since the field intensity is weak in these regions. Therefore, the size of the air block is sufficient for this application. Also, the magnetic field lines are observed as closed paths that are perpendicular to the current flow. As a result, the model is adequate in reflecting the nature of the electromagnetic field.

The observations on the results constitute a brief comparison of the calculations with the theoretical issues. The consistency of the numerical simulations with the experiments is analyzed by considering the heat generation within the workpiece.

The heat generation rate per unit volume of the workpiece is shown in Figure 7.7(a). When the whole of the workpiece is considered, it appears that the maximum heat generation zones are located around a ring on the surface. This ring-shape is also observed in the experiments (Figure 7.7(b)). In the earlier stages of heating an orange colored ring appears on the surface. The rate of temperature increase is relatively high on the portions of maximum heat generation. However, as time proceeds, this shape becomes invisible since the neighboring zones turn

also to orange color due to temperature increase and the temperature distribution on the relatively hot surface area becomes more homogeneous due to conduction.

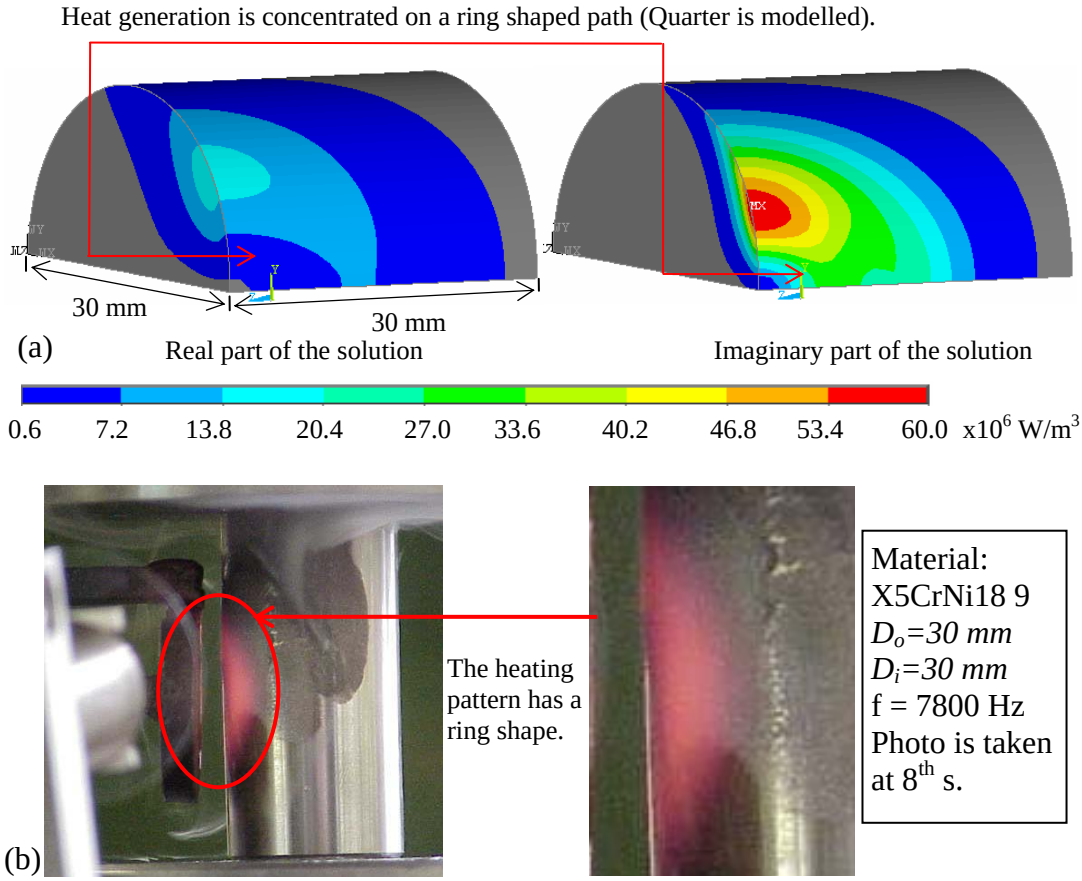

Figure 7.7 (a) Ring shape observed in the earlier stages of heating. (b) The calculated values of heat generation rate per unit volume (JHEAT) on the workpiece surface.

7.3.2 Utilization of Results in the Overall Analysis of Local Heating

In this study, the main benefits of the electromagnetic analysis are describing the nature of the induction heating process and obtaining the distribution of heat generation rate on the workpiece. The results are utilized in the thermo-mechanical simulation of the process, which is explained in detail in Chapter 8. In those simulations, heat generation rate is assigned to the elements in the model.

The correctness of these simulations is verified by comparing the actual and calculated values of temperature at a certain point. The pattern of heat generation is preserved as calculated by the electromagnetic field simulations; however the magnitude of the heat applied to the model is modified to obtain the real temperature history at the point. The discrepancies between the assumed and actual values of current, the heat loss due to radiation, change of convection coefficient at elevated temperatures and temperature depended change of electrical resistivity of the material are taken into consideration by modifying the heat generation rate. In Figure 7.8, the temperature data taken from a predetermined point is presented. In this analysis the heat generation rate values are multiplied by 28 at every point in the workpiece. The actual and calculated values of temperature are in good agreement. In order to reflect the effects of convection, an average convection coefficient of 350 W/m^2K is used in the analysis. Briefly, the ratio of heat generation rate at a specific point to the overall value is obtained by the electromagnetic analysis; however the real values of net heat generation rate can only be obtained after modifications done regarding the actual temperature data.

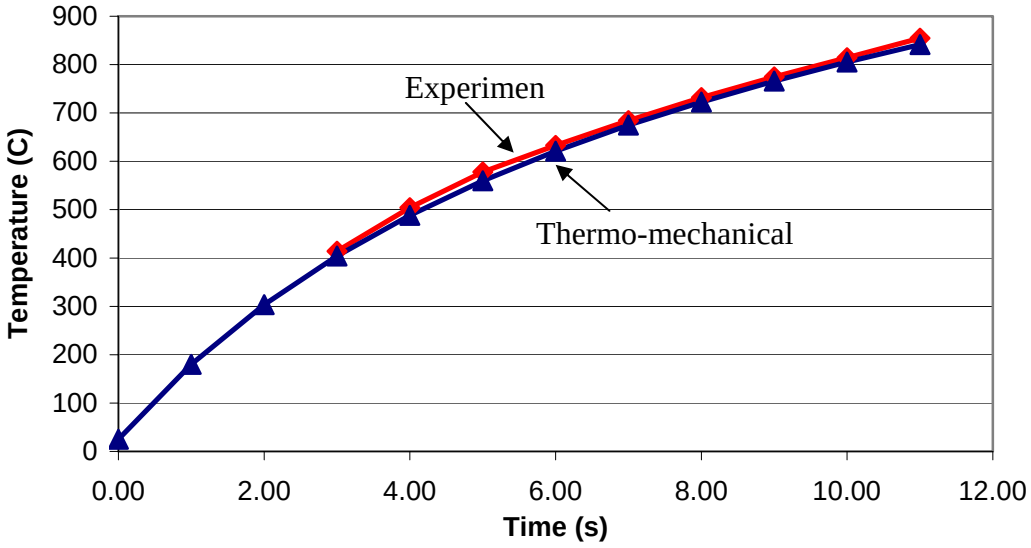

Figure 7.8 The temperature distribution at the end of the heating stage of a thermo-mechanical analysis. Heat generation values at obtained from the electromagnetic analysis is multiplied by a coefficient of 28.

The absolute values of heat generation rate per unit volume are expected to reflect realistic values. However, there are two main reasons why the coincidence of the values from numerical simulation and experimental data cannot be ensured. First, the heat generation data cannot be recorded during the experiments. The only data obtained is the temperature of a single point during heating. Second, it is not possible to measure the actual value of current on the induction coil with the available equipment. Therefore, an average value is assigned to the coil model in the simulations.

In each of the calculations, constant values are used for relative permeability and electrical resistivity. However, there is a continuous change of temperature during the heating stage and also a temperature difference within the body at a certain instant of time. The values of the two parameters change during heating and this situation is not reflected in the simulations. X5CrNi18 9 and Ti6Al4V are non ferromagnetic magnetic materials. Therefore, the heating pattern does not vary due to change of magnetic permeability for those materials. On the other side, electrical resistivity increases with increasing temperature. The change of heat generation within the workpiece due to the variation of electrical resistivity is neglected in the thermo mechanical simulations.

The magnitude of current passing through the coil has a direct effect on heat generation on the workpiece. As explained in Section 3.2, heat is generated proportional to I^2R, where I is the magnitude of current in the conductor and R is the resistance of the material. It is expected that the amplitude of the induced current is directly proportional to the coil current. Therefore the coil current should not effect the distribution of heat generation; it should only determine the amount of heat generation at any point on the workpiece. This situation is proved by the computer simulations. The results of two analyses are compared (Figure 7.9). In one of the analyses the current frequency is 7800 Hz and amplitude is 1500 A. In the other analysis, frequency is kept constant whereas the amplitude is increased to 4500 A. The heat generation rate data is taken from an arbitrary path on the

workpiece that starts from the midplane on the workpiece and extends in the direction of the length. The heat generation rates are presented in the Figure 7.9. The ratio of heat generation rate is indicated on the graph. As seen clearly, at every point on the path, the ratio of heat generation in the second simulation to that of first simulation is 9.

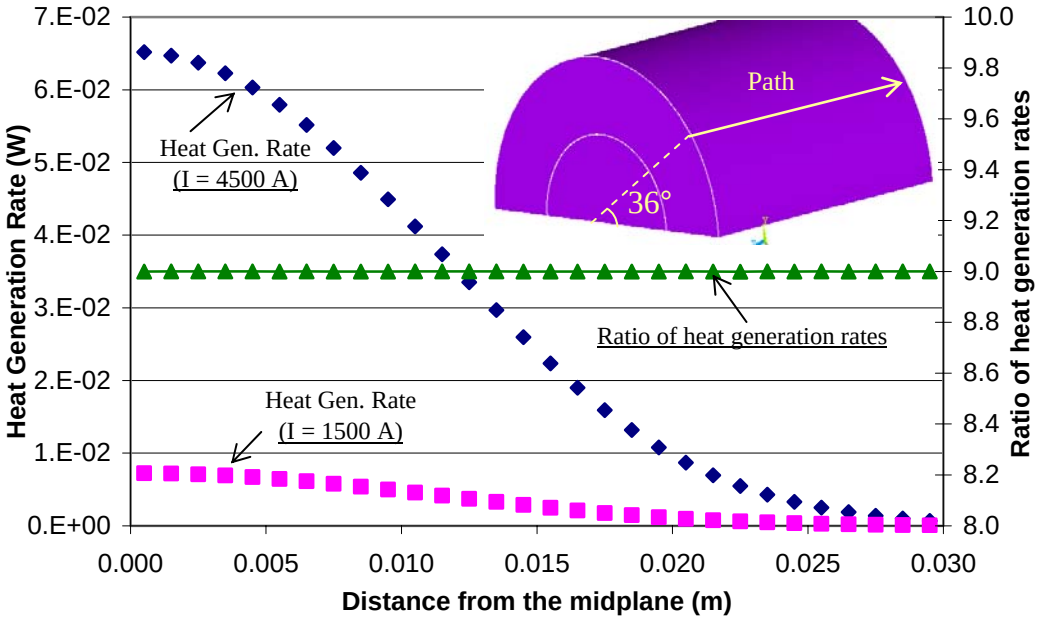

Figure 7.9 Comparison heat generation rates for different values of current.

Increase of amplitude of coil current results in a corresponding increase of heat generation rate, which proportional to the square of the increase in current at each point on the workpiece. Also, the overall heat generation rates in case of 1500 A and 4500 A are 24.24 W and 218.2 W, respectively. The second value is exactly 9 times the first one. These results indicate that relative distribution of heat generation remains unchanged if the amplitude of current is varied. Therefore, it is acceptable to calibrate the magnitude of current during the thermal analysis of heating, by changing the magnitude of heat generation rate, at each point of the workpiece, at the same ratio.

7.3.3 Summary of the Results

Two different frequency values used in the experiments are 7800 Hz and 10500 Hz. An average value of 1500 A is assigned to both of the coils. The heat generation rates obtained for these values and for the two different materials are given in Figures 7.10-7.15.

The results indicate that the increase of frequency results in a higher rate of heat generation on the surface area. The skin depth is decreased; therefore a higher percentage of the heat is generated near the surface area. It is also observed that the overall heat generation in the workpiece is increases at high frequencies.

The amount of heat generation near the surface increases with decreasing skin depth. Since the skin depth is directly proportional to resistivity, in the materials with lower resistivity values, higher heat generation rate is expected on the surface if the relative permeability values are the same. When the heat generation rate values on the surface of the workpieces in Figures 7.10, 7.12 and 7.14 is observed, it is seen that the maximum value occurs in the 16MnCr5 specimen, which has the minimum electrical resistivity.

In the X5CrNi18 9 workpiece, the total heat generation rate in the workpiece is higher compared to the other materials. The overall heat generation on the workpiece is dependent on the resistance of the material and resistance is directly proportional to electrical resistivity of the material. Therefore the overall heat generation rate is expected to increase with increasing electrical resistivity. However, in cases of high resistivity, the skin depth also increases. The eddy currents generated in the workpiece will flow through a wider volume compared to a material with lower resistivity. The total resistance of the workpiece, which is inversely proportional to the area on the conductor, decreases. This results in a corresponding decrease of the total heat generation rate.

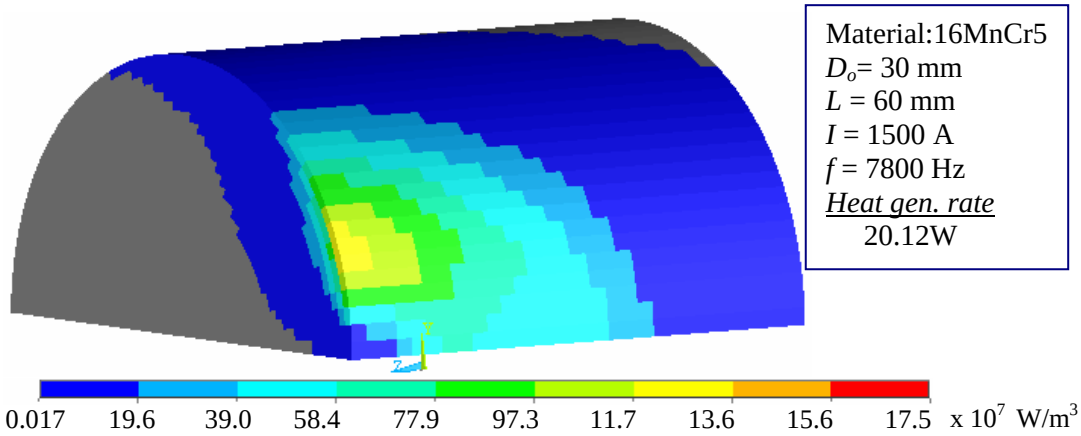

Figure 7.10 Heat generation rate on the 16MnCr5 workpiece (f = 7800 Hz)

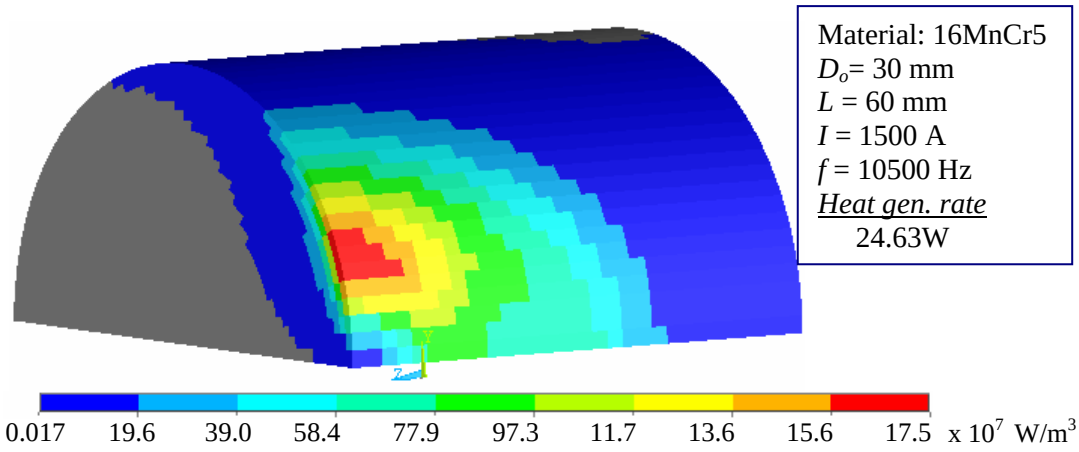

Figure 7.11 Heat generation rate on the 16MnCr5 workpiece (f = 10500 Hz)

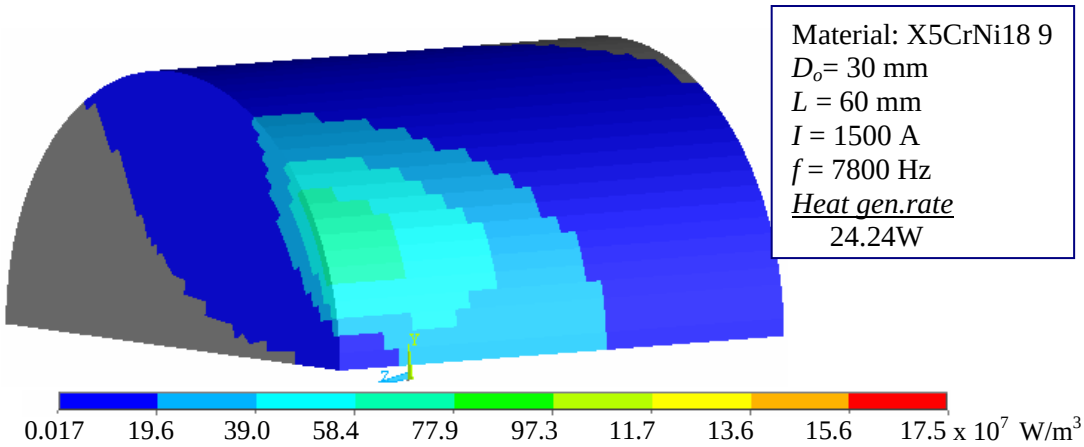

Figure 7.12 Heat generation rate on the X5CrNi18 9 workpiece (f = 7800 Hz)

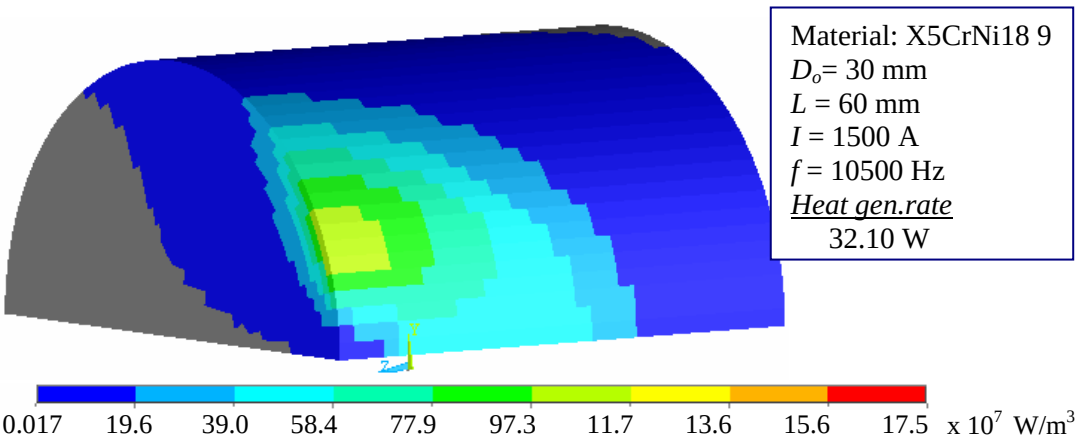

Figure 7.13 Heat generation rate on the X5CrNi18 9 workpiece (f = 10500 Hz)

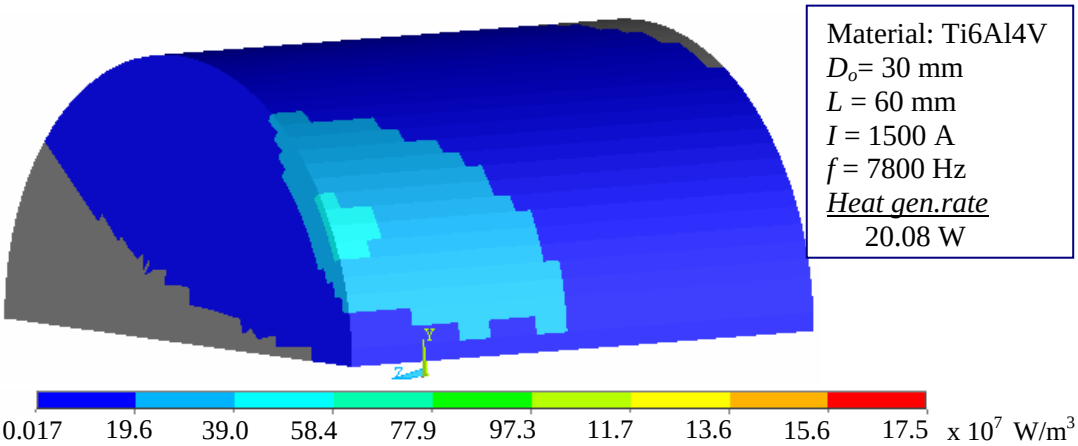

Figure 7.14 Heat generation rate on the Ti6Al4V workpiece (f = 7800 Hz)

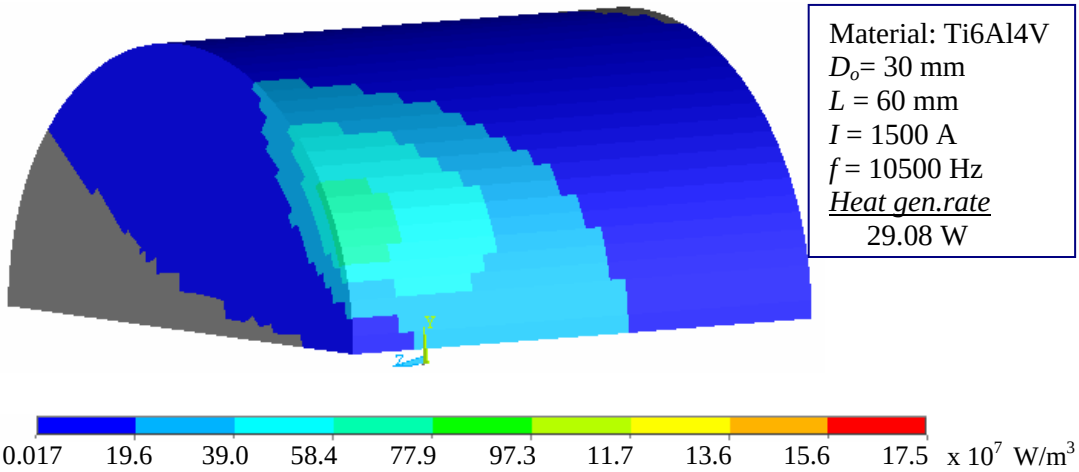

Figure 7.15 Heat generation rate on the Ti6Al4V workpiece (f = 10500 Hz)

The results presented above constitute a summary of the heating cases investigated in the experiments. Those values are used in the heating stage of the thermo mechanical analysis.

7.4 Conclusion

The induction heating process is simulated by means of a virtual model of the workpiece and the coil. The discrepancies between the actual values of heat generation rate and the result of electromagnetic analysis originate mainly from the assumptions on the amplitude of applied current. It is also due to variation of temperature dependent material properties, i.e. relative magnetic permeability and electrical resistivity, during experiments. However, in the current approach, the *amount* of heat generation rate is regulated in the later stages of the overall analysis, i.e. thermo-mechanical modeling, and the *distribution* of heat generation rate is considered as the main contribution of the electromagnetic field calculations to the study. It has been shown that the amplitude of current do not have any effect on the pattern of heat generation. The changes in the heating characteristic due to variation of the material properties are compensated by the regulating the heat in thermo-mechanical modeling. As a result, the relative heat generation pattern will be preserved in the next stage, namely the thermo-mechanical analysis, and thermal boundary conditions will be applied accordingly.

CHAPTER 8

THERMO-MECHANICAL ANALYSIS OF THE HEATING AND FREE FORMING PROCESS

8.1 Introduction

The finite element method is utilized in the numerical simulation of the local heating and free forming process. The simulations are designed in accordance with the experiments. Once the efficiency of the simulations in reflecting the actual process is proved, the effects of some process parameters are investigated. In this chapter, the modeling strategy, comparisons of the numerical calculations with the experiments and the effects of some process parameters are presented.

8.2 Numerical Analysis Parameters

The heating and upsetting processes are simulated in two different successive calculation steps, namely load cases. In the heating load case, the temperature distribution within the workpiece is calculated at the end of a certain time interval. In the second load case, the punch moves with a velocity of 3.7 mm/s and performs the free forming process. The relative residuals and displacements, the definitions of which are given by Eq. (4.28) and Eq. (4.30), are selected as the convergence criteria. The convergence tolerance is set to 0.05. Remeshing is performed during the free forming process, since the elements on the local bulge region are distorted excessively. In the analysis of thin walled hollow workpieces, for which the ratio of

inner diameter to outer diameter is 0.73, remeshing operation could not be performed in a reasonable time by the software. Therefore, this option is not activated in analysis of thin walled workpieces.

8.2.1 Material Properties

The analyses are carried out for three different materials, namely 16MnCr5, Ti6Al4V and X5CrNi18 9. The material properties used in the analyses are given in Section 5.3. The physical properties of 16MnCr5 and X5CrNi18 9 are temperature dependent except Poisson's ratio and mass density. For Ti6Al4V, all the physical properties except the thermal conductivity are constant during the analysis.

8.2.2 Determination of the Friction Coefficient

The friction coefficient on the contact surface between the die and workpiece is determined experimentally by ring compression test. In the ring compression test, hollow specimens are formed gradually to ½ of its initial length under compressive forces. Inner diameter, outer diameter and length values are recorded in each step and the values are compared to the results obtained from the numerical simulation of the compression test for different values of friction coefficient. The calculated and experimentally determined dimensions of 16MnCr5 specimens for some values of friction coefficient are presented in Figure 8.1. It is found that a friction coefficient of 0.06 and relative sliding velocity of 1 are appropriate for simulation of friction on the contact surfaces. The tests with X5CrNi18 9 specimens have given the same results. The Ti6Al4V specimens are not suitable for ring compression test since they are more brittle than the steel specimens at room temperature. The same friction coefficient is used in simulations of titanium alloy specimens.

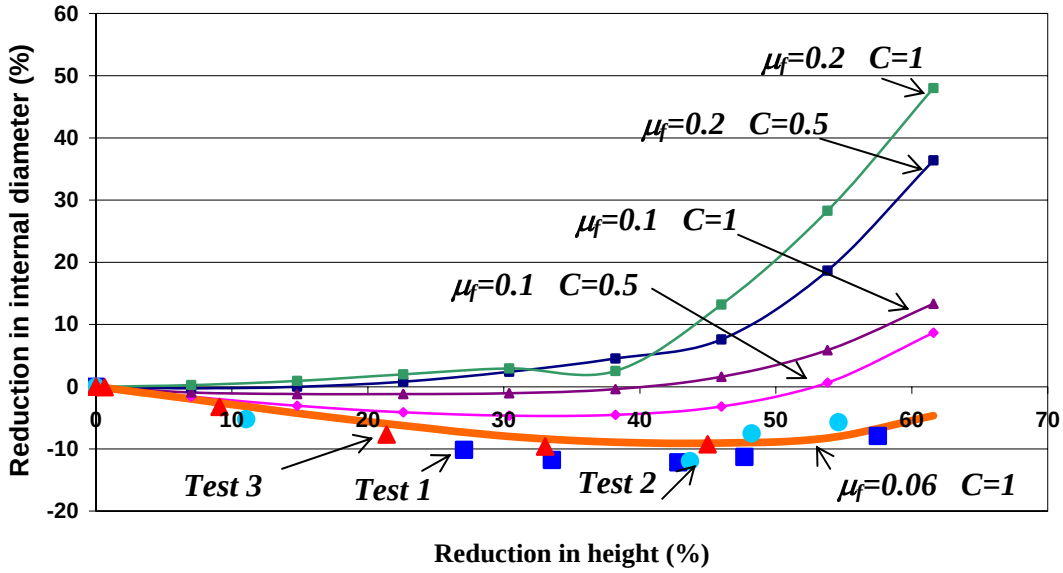

Figure 8.1 The friction calibration curves for 16MnCr5 specimens.

8.3 Criteria for Comparison of the Numerical Results with the Experiments

In order to prove the reliability of the numerical simulations, the results of the numerical calculations are compared with the experiments regarding the temperature data recorded during the experiments and the shape of the product.

In the first step of analysis, the temperature reading of the pyrometer is compared to the calculated values. The temperature data is taken by means of a pyrometer, which is focused to a single predetermined point on the surface. The location of the point is shown in Figure 4.4. The corresponding location of the point on the finite element mesh is shown in Figure 8.2. The temperature values in Figure 8.2 are taken from an analysis of hollow stainless steel specimen, at the end of 61 s of heating. In the ideal case, the temperature data taken from point P_1 is expected to fit to the experimental temperature curve, in a successful simulation. However, it is seen in the simulations that in an analysis, in which the temperature at P_1 fits perfectly to the experimental data, the final shape of the workpiece does fit to the shape of the actual product. Furthermore, analyses with lower or higher

temperature values at P_1, gives better solutions. This situation arises from the nature of the pyrometer and experimental errors. The pyrometer head takes the records temperature on the area of the workpiece that is enclosed by its pivot laser beam. Therefore, the temperature data on the neighboring nodes should also be checked.

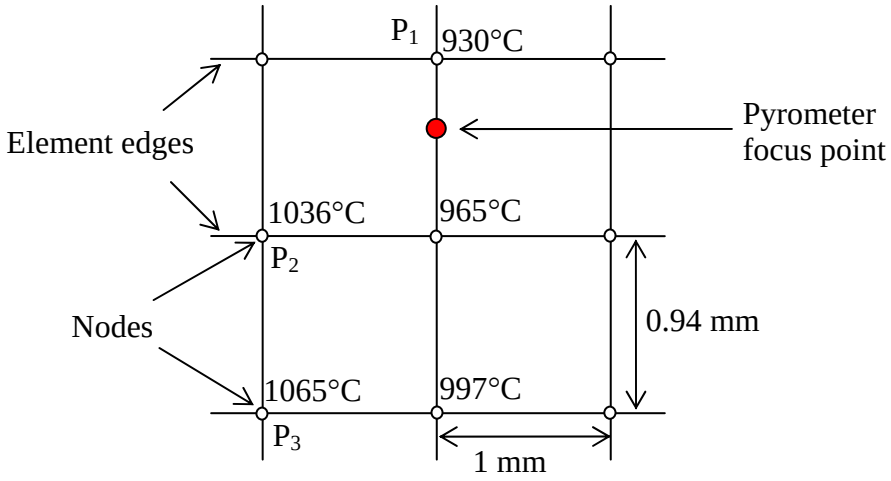

Figure 8.2 The nodes on the surface of the workpiece in the neighborhood of the pyrometer focus point.

On the other side, the experimental errors may occur as acquiring the temperature data. As seen in Figure 8.2, about 60°C of temperature change may occur within a 1 mm distance. Therefore, a slight tilt of the pyrometer head may cause considerable shift of the temperature curve from its assumed value. Although the position of the pyrometer head is checked during the experiments, the temperature of the other nodes in the neighborhood of the focus point should also be compared with the experimental data in case of poor simulation of the final shape of the workpiece.

The accuracy of the numerical simulations is evaluated by comparing certain dimensions together with the general shape of the workpiece and the flow lines on the cross sectional area at the end of the simulations. In Figure 8.3, a typical cross sectional view of a locally heated and formed specimen is shown schematically.

The inner and outer diameters after deformations are denoted as D_i and D_o. The bulge on the heated area represented on the right-hand side and its height and width are described by w_2 and w_3, respectively. The distance between the tip of the bulge and the rear side is w_1. The dimensional check is done regarding these critical dimensions.

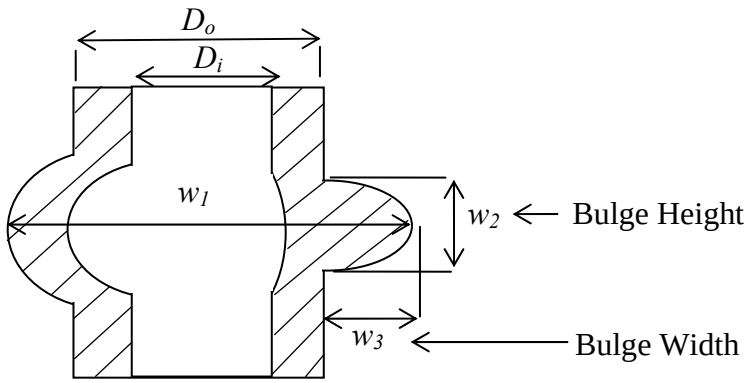

Figure 8.3 A schematic representation of the products and their critical dimensions.

8.4 Preliminary Studies

In this section, the general strategy of modeling the experiments, the assumptions done during modeling and the boundary conditions applied to the model are explained. The analysis parameters are presented.

8.4.1 Geometrical Modeling of the Workpiece

The models of the experiment specimens are created in 3D space, since the boundary conditions are not suitable to reduce it to a 2D axisymmetric model. However, the distribution of heat generation and the geometry of the workpiece are symmetrical with respect to the two perpendicular planes passing through the center of the workpiece as explained in Section 7.2.1. This provides the opportunity to

simulate the process by using a model of one quarter of the actual specimen. The model of the workpiece and the symmetry planes are shown in (Figure 8.4). The *symmetry plane 1* is parallel to the longitudinal axis of the specimen and passes through the point on the workpiece surface that lies opposite to the center of the helical coil. The *symmetry plane 2* is parallel to the circular cross section of the workpiece and divides the workpiece to two equal pieces along its longitudinal axis. There is no heat flux or displacement in the direction perpendicular to the symmetry planes [20].

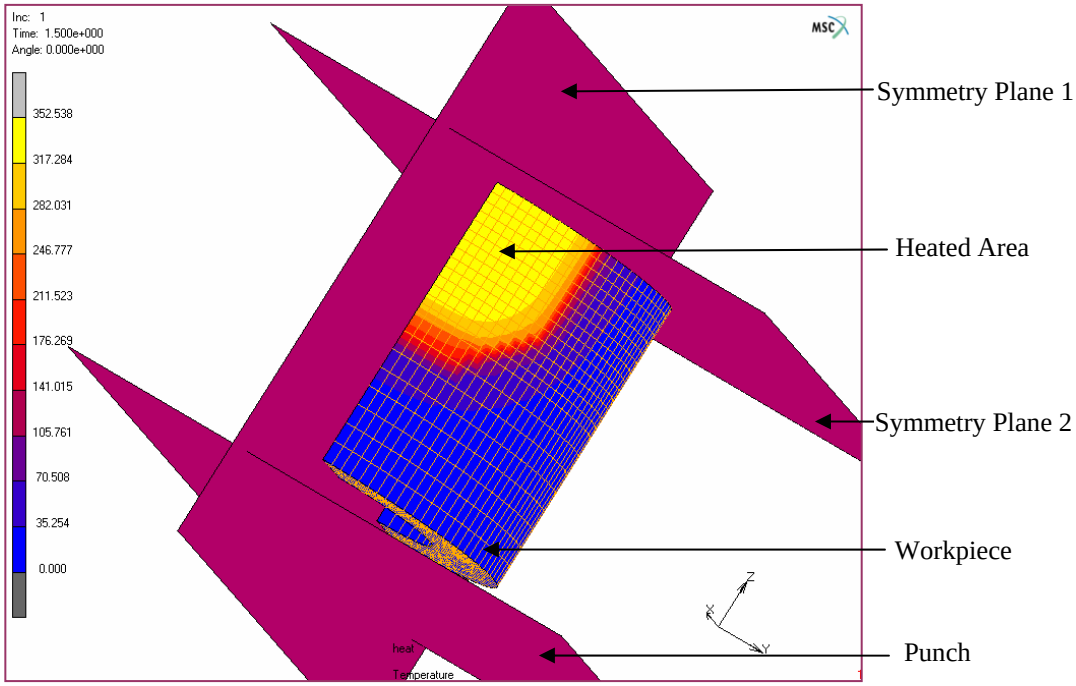

Figure 8.4 Numerical model of a hollow experiment specimen.

8.4.2 Preliminary Simulation of Heating

In induction heating process, the heat is generated within the workpiece and majority of the heat generation is concentrated near the part of the surface area opposite the induction heating coil. Depending on the geometry of the coil and the workpiece, the heat generation pattern may be non homogeneous on the surface of the workpiece. The first method proposed for the numerical simulation of the

process is to apply the heat energy as a surface flux that is distributed evenly on a certain part on the surface of the material. The energy generation inside the workpiece and the uneven distribution of heat generation on the surface are discarded in this approach. The nodes, to which the heat energy is applied as a boundary condition, are shown in Figure 8.5. The circular hot area observed in the experiments is modeled as a polygon. The small dots on the finite element mesh represent the nodes with thermal boundary conditions. The heat energy applied to the nodes on the symmetry planes and the single node that lies on the intersection of the two symmetry planes is set to one half and one quarter of the internal nodes, respectively.

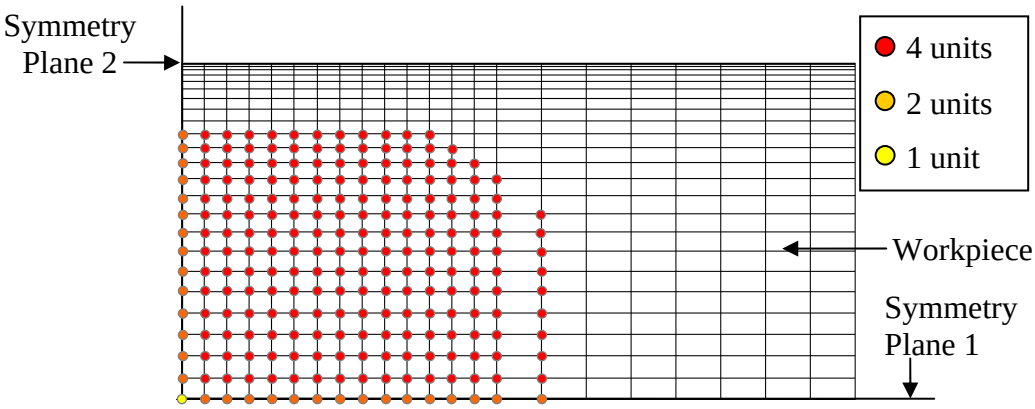

Figure 8.5 Schematic representation of the nodes, to which heat energy is applied.

The heat generation in the workpiece and losses due to convection and radiation cannot be determined during the experiment. The values of heat energy applied to the model are determined regarding the actual temperature distribution on the surface of the workpiece. Therefore, the flux values to be used in the simulations are determined after several trials by finite element models.

The temperature data obtained for a hollow stainless specimen after successive heating trials are given in Figure 8.6. It is seen in the experiments that in stainless steel specimens, after 1000^{o}C, the slope of the temperature vs. time graph decreases. Applying constant heat energy during heating is not sufficient to reflect

the actual heating process. The temperature data obtained from the simulations does not show such a behavior as seen in the simulations labeled as *Simulation 1,2* and *3* in Figure 8.6. In order to simulate the real situation, the heat flux value is multiplied by a correction factor. The factor determines the percentage of the entered energy value to be given to the workpiece at a specific instant of time. In other words, the heat energy applied to the model can be varied during the heating process by this method. The dominated effects of heat losses due to radiation and convection in the later stages of heating are reflected by this way. In *Simulation 4* in Figure 8.6, this method is used. The relatively sudden changes in the temperature curve in the simulations correspond to the instants, where the correction factor changes.

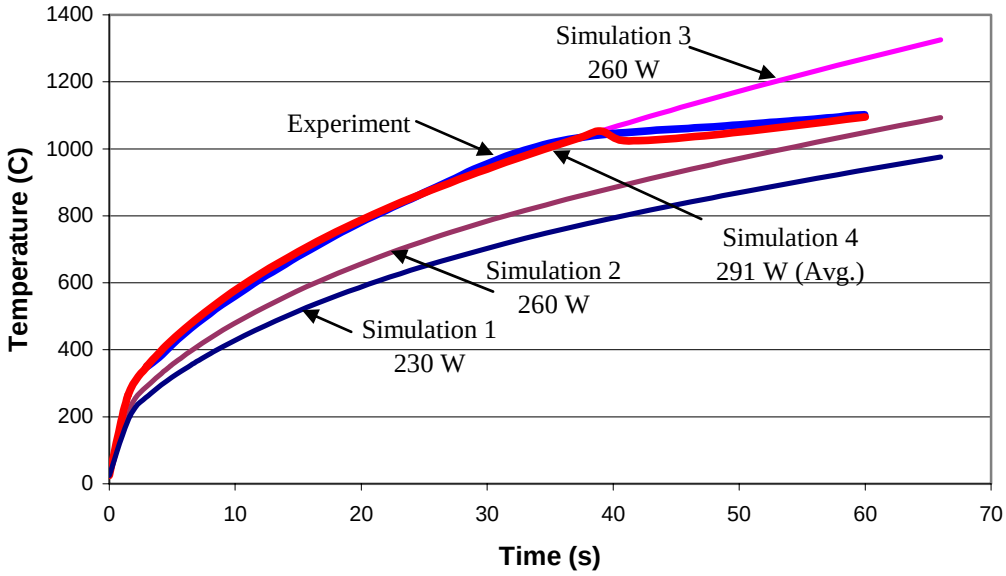

Figure 8.6 Comparison of experimental temperature data with the simulations.

In Figure 8.7, the temperature curves for *Experiments 46* and for its successful simulation are presented. The value heat flux drops to 73% of its initial value at the 40th second of heating. Although some instant changes occur, which are not realistic, they do not have a significant effect on the final result. By this method, a better fit to the temperature curve can be obtained.

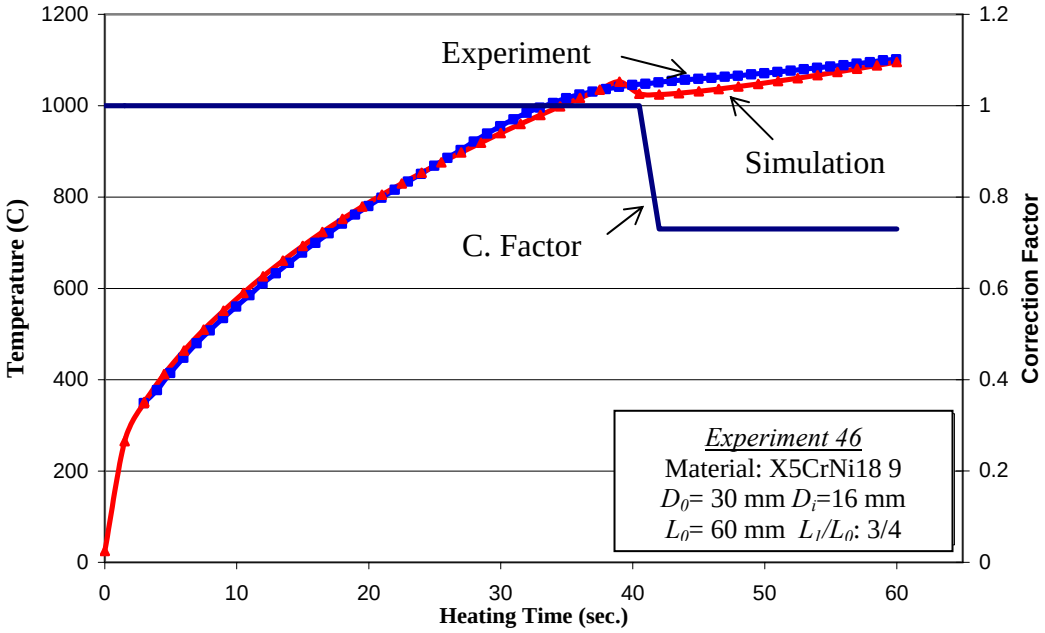

Figure 8.7 Comparison of experimental temperature data with simulations for *Experiment 46*.

8.4.3 Preliminary Results

The actual specimen obtained in *Experiment 46* and its numeric simulation are shown in Figure 8.8. The general shape of the experiment specimen is successfully calculated in the simulations.

Figure 8.8 The actual of product in *Experiment 46* and its numeric model.

The dimensions taken from the experiment specimen and computer model after simulation of *Experiment 46* are given in Table 8.1. The error for each dimension does not exceed 1 mm. When the probable errors in reading the dimensions are considered, the results are satisfying.

Table 8.1 Comparison of product dimensions with the numerical results for *Experiment 46*.

Dimensions (mm)							
Initial workpiece dimensions		D_o	D_i	L	Material: X5CrNi_18_9 Pyrometer reading (max): 1100°C		
		30	16	60			
		D_{o1}	D_{i1}	L	w_1	w_2	w_3
Final Dimensions	**Experiment**	32.9	15.3	30.0	50.9	11.5	9.0
	Simulation	33.5	15.7	30.0	49.6	11.1	8.0

A better idea can be gained about the flow of material, buckling behavior of the walls, barreling and formation of special features such as bulges, etc. after the inspection of the flow lines on the cross sectional area of the experiment specimen that is cut through the plane of symmetry. In Figure 8.9, a detailed photograph of the upper half of the cross sectional area is presented, which is completed on the lower side, with the computer simulation of the same experiment. In order to have an effective illustration of the dimensional differences, the two pictures are resized such that the lengths of the workpieces are the same in both.

The general shape and direction of the flow lines are the same both in the experiment and the simulation results. The simulations justify an important situation observed in the experiments. In Figure 8.9, in the part denoted as 1(a), the top surface of the material, which is previously in contact with the die, starts to separate from the die surface. The same situation is also seen in part 1(b), in the snapshot of the computer simulation. However, there are some differences on some critical points on the workpiece. The height of the local bulge is smaller in the simulations. In the region labeled as 1 in Figure 8.9(a), there is a slight difference

in the shape and size of the inner bulge. The height of the bulge is larger in the real specimen and the shape is not smooth as it is in the simulation results. The largest error is at the rear side of the specimen where buckling occurs.

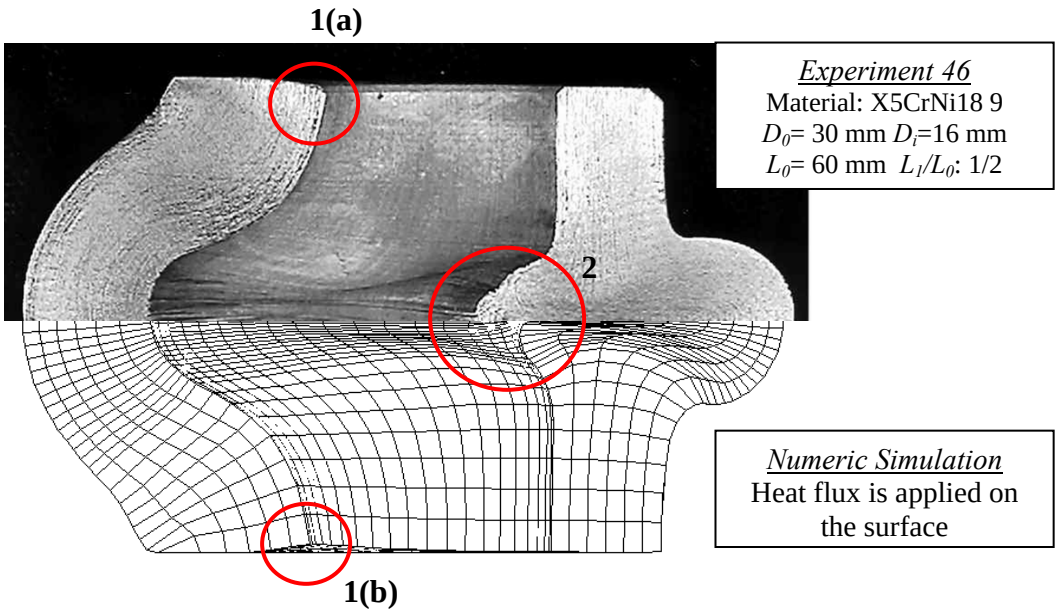

Figure 8.9 Comparison of the flow lines on the actual specimen (*Experiment 46*) with the result obtained by simulation.

Another comparison of the numerical and experimental results is done on the product obtained in *Experiment 60*. The experiments *60* and *46* have the same heating conditions. The only difference between the two experiments is the relative height reduction, which is ½ for *Experiment 46* and ¾ for *Experiment 60*. Therefore, the results of *Experiment 60* can be considered as an intermediate step of E*xperiment 46*. The photograph of the etched cross section of the workpiece for *Experiment 60* is given together with the simulation result in Figure 8.10. The difference of the shape in experiment and simulation can be seen clearly on region 2. The secondary bulge, which is expected to appear on the inner surface of the heated wall, is not formed yet, even though there is a bulge in the real specimen. The difference in the wall thickness in region 1, which was noticeable in *Experiment 46*, is not large since the upsetting is terminated at an earlier step.

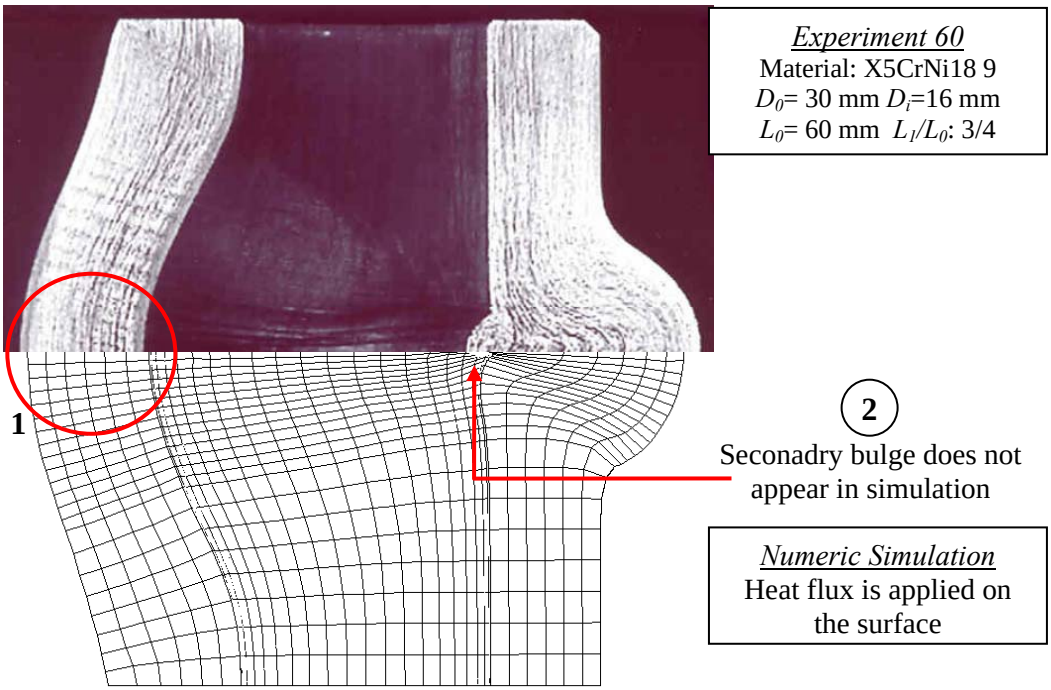

Figure 8.10 Comparison of the flow lines on the actual specimen (*Experiment 60*) with the result obtained by simulation.

The critical dimensions of the product obtained in *Experiment 60* are given in Table 8.2. The largest deviation of the numerical results from the experiments is on the bulge dimensions. The maximum difference between the tow sets of solutions are below 1 mm.

Table 8.2 Comparison of product dimensions with the numerical results for *Experiment 60*.

Dimensions (mm)							
Initial workpiece dimensions		D_o	D_i	L	Material: X5CrNi_18_9 Pyrometer reading (max): 1100°C		
		30	16	60			
		D_{o1}	D_{i1}	L	w_1	w_2	w_3
Final Dimensions	**Experiment**	30.9	15.5	43.0	43.2	15.0	6.2
	Simulation	31.7	16.1	43.0	42.3	15.2	5.4

It is observed in the experiments that the temperature distribution on the bulge area determines the mode of deformation during free forming. Therefore the most

critical part of modeling is the modeling of heating process. Simulation of the induction heating process by a local homogeneous surface heating case gives results that are in accordance with the experiments. However, this approach is not satisfactory in representing the actual heating case. In cases, where the skin depth is comparable to the diameter of the specimen, heat flux on the surface cannot represent the actual situation. Therefore, for a better analysis of the process, heat generation pattern within the workpiece, that is obtained by the electromagnetic field calculations are used for heating.

8.5 Improved Simulation of the Process

Simulation of the process is improved by altering the thermal boundary conditions. The heat generation pattern on the surface and inside the workpiece, which is calculated in the electromagnetic analysis, is applied to the thermo-mechanical model. The advanced numerical model of the process is shown in Figure 8.11

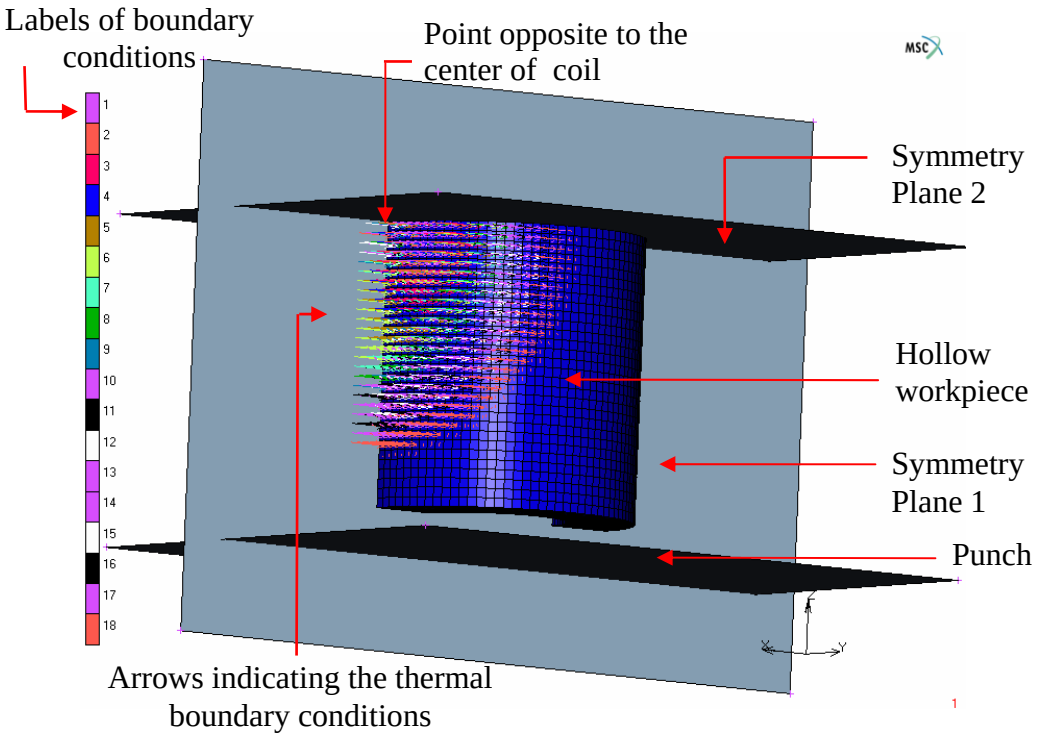

Figure 8.11 The improved numerical model of the heating and upsetting process.

One quarter of the workpiece is modeled by using symmetry planes. The boundary conditions labeled by colors in Figure 8.11. The method of assigning the boundary conditions to the finite element model is explained in Section 8.5.1.

Three different geometries are used in the calculations. The solid cylinder and two hollow cylinders with different wall thickness values are shown in Figure 8.12. The mesh near the surface of the cylinders is similar to the mesh used in the electromagnetic calculations. This is necessary to adapt the thermal data obtained from those simulations to the thermo-mechanical analysis model.

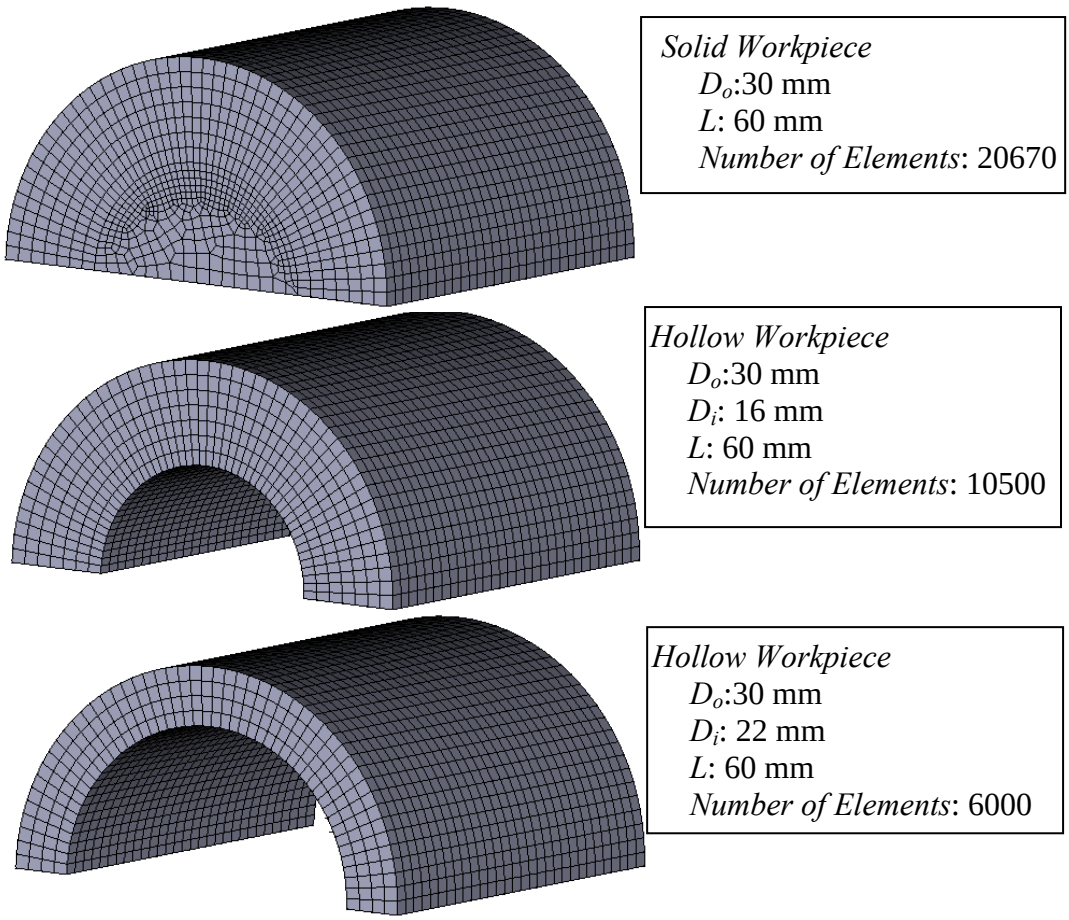

Figure 8.12 Different geometries used in the numerical simulations.

8.5.1 Determination of the Thermal Boundary Conditions

The heat that is absorbed by the specimen cannot be determined during the experiment. Also, with the available equipment, the true value of the current on the coil cannot be measured during the experiments. The first aim of the calculations is to determine the correct heat value to be applied as a boundary condition that will lead to the actual temperature distribution on the surface of the workpiece at the end of heating.

The helical geometry of the induction heating coil and relative orientations of the coil and workpiece results in a complex distribution of heat generation on the surface and along the wall of the workpiece. In the thermo-mechanical simulation of the process, the heat generation within the workpiece is simulated by applying the heat generation rate per unit volume as a boundary condition. The heat generation pattern created by the available induction heating coil is determined for the 3 types of materials for a coil current of 1500 A, by the electromagnetic field calculations. The details of electromagnetic simulations are given in Chapter 7. Once the spatial heat generation pattern within the material is obtained, the amount of heat generation is modified regarding the final temperature distribution on the workpiece.

The values of heat generation rate per unit volume are obtained for each element from the electromagnetic analysis of induction heating. However, it is not feasible to apply the exact values directly to all of the elements of the model due to the excessive modeling effort and high computational time. Therefore, average values are assigned to the elements. The elements are divided to 20 groups with respect to the value of heat generated within each of them. The determination of heat generation value for each group in a hollow stainless steel specimen is presented in Figure 8.13. The vertical axis of the graph is the value of heat generation per unit volume of elements. The values are not taken on a specific path but recorded for each of the elements that are sorted in a decreasing order with respect to the heat

generation in them. The horizontal axis indicates the ratio of the total heat generation in the elements that remain on the left of this point, to the total heat generation in the workpiece. The elements are divided into 20 groups such that 5% of the total energy is produced on the elements in each group. An average value is assigned to the elements in the group. 90% of the total heat is generated within about 2500-3000 elements depending on the material and frequency of the coil current. In order to decrease the computational time, the remaining 10% of the heat generation is neglected. Since this amount of heat is generated within 7500 elements in the hollow models and 20000 elements in the solid models, this assumption is very beneficial for decreasing the computational cost. Once the boundary conditions are determined for each element, they are rearranged and inserted in the input data file of the numerical model.

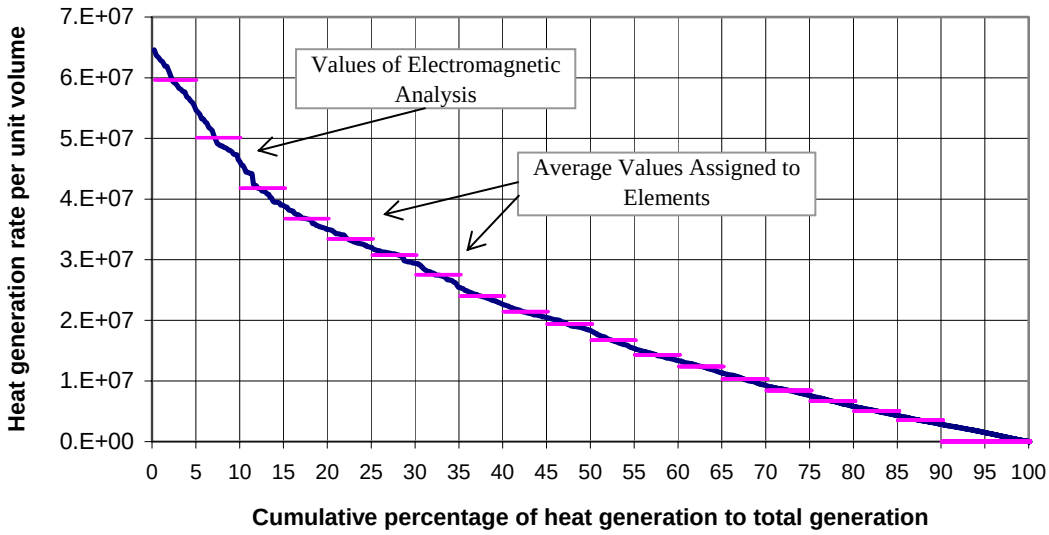

Figure 8.13 Determination of average heat generation rate

An initial condition of 25°C is applied to all of the elements. The convection heat transfer between the workpiece surface and the surrounding air is modeled by introducing a constant convection coefficient. The recommended value of convection coefficient is 350 $W/m^2.K$ for hot forging applications [20]. The software does not calculate the radiation heat transfer; therefore heat loss due to radiation is discarded.

8.5.2 Analysis of Forming Hollow Workpieces

The typical formations observed on the hollow workpieces are investigated on *Experiment 46* (Figure 8.14(a)). In the preliminary simulations, different heat generation values are assigned to the workpiece. The final shape obtained from the analysis that shows the best correspondence with the experiments is given in Figure 8.14(b). The final product shape is obtained successfully in the simulations.

Material: X5CrNi18 9

Initial dimensons
D_o = 30 mm L_0 = 60 mm

Free Forming Parameters
L_i / L_0 = 0.50

Heating Parameters
Avg. heat gen. rate: 425 W
Heating Time: 16 s

Figure 8.14 The comparison of the calculated shape and the actual shape of the product for *Experiment 46*.

A comparison of temperature data obtained from the simulations and the experiments is given in Figure 8.15. The maximum deviation of temperature at point P_1 from the experimental value is 14%. This value decreases to 4% at point P_3. The error is within acceptable tolerances.

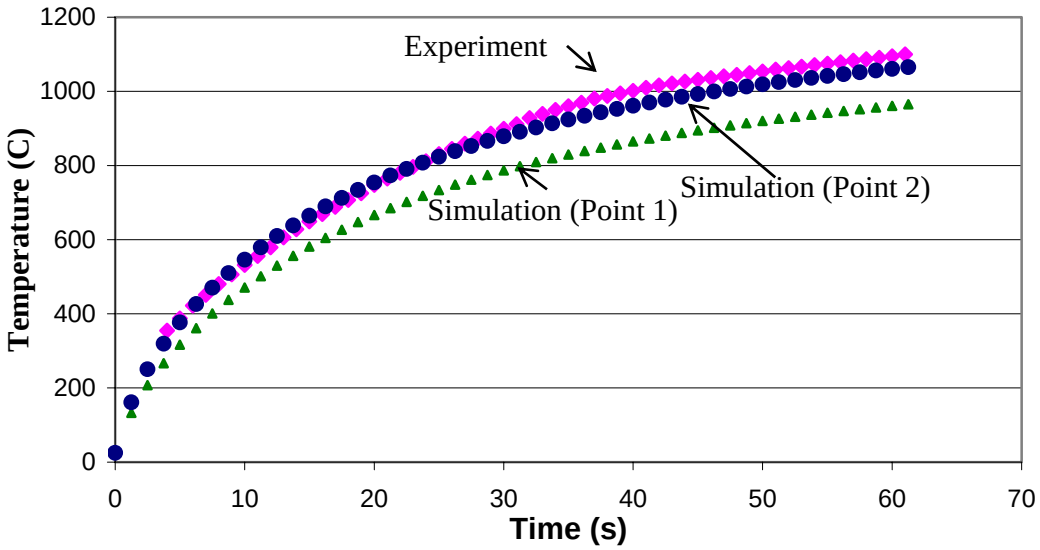

Figure 8.15 The comparison of the temperature curves obtained during the experiments and the simulations for *Experiment 46*.

A further investigation on the accuracy of the solution is done by comparing certain dimensions of the product. The dimensions taken from the experiment specimen and computer model of *Experiment 46* are given in Table 8.3. The error for the inner and outer diameters does not exceed 10%. This value increases for the bulge dimensions. The error on the height (w_2) and width (w_3) of the bulge are 20% and 28%, respectively.

Table 8.3 Comparison of product dimensions with the numerical results of modified model for *Experiment 46*.

Initial workpiece dimensions (mm)		D_o	D_i	L	Material: X5CrNi_18_9 Pyrometer reading (max): 1100°C		
		30	16	60			
		D_{o1}	D_{i1}	L	w_1	w_2	w_3
Final Dimensions (mm)	**Experiment**	33.0	15.3	30.0	50.6	10.8	8.7
	Simulation	34.0	16.9	30.0	47.9	8.6	6.3

The deformation is investigated by analyzing the plastic strain and shape of the local formations on the cross sectional area of the specimens. The cross sectional area of the specimen obtained from the numerical analysis of *Experiment 46* is

shown in Figure 8.16. The typical formations observed for the hollow specimens can be seen in the figure. On the heated zone, a local bulge is observed as expected. On the inner portion a secondary bulge is formed and the rear side of the specimen buckles under the compressive loads. The contour bands visualize the regions where there is relatively much deformation. The deformation is localized on the mid portion of the heated wall. From the beginning to the end of the process, the maximum equivalent strain is concentrated on this portion. The tip of the bulge goes through less deformation during the process when compared to the other parts in the same level, through the heated wall.

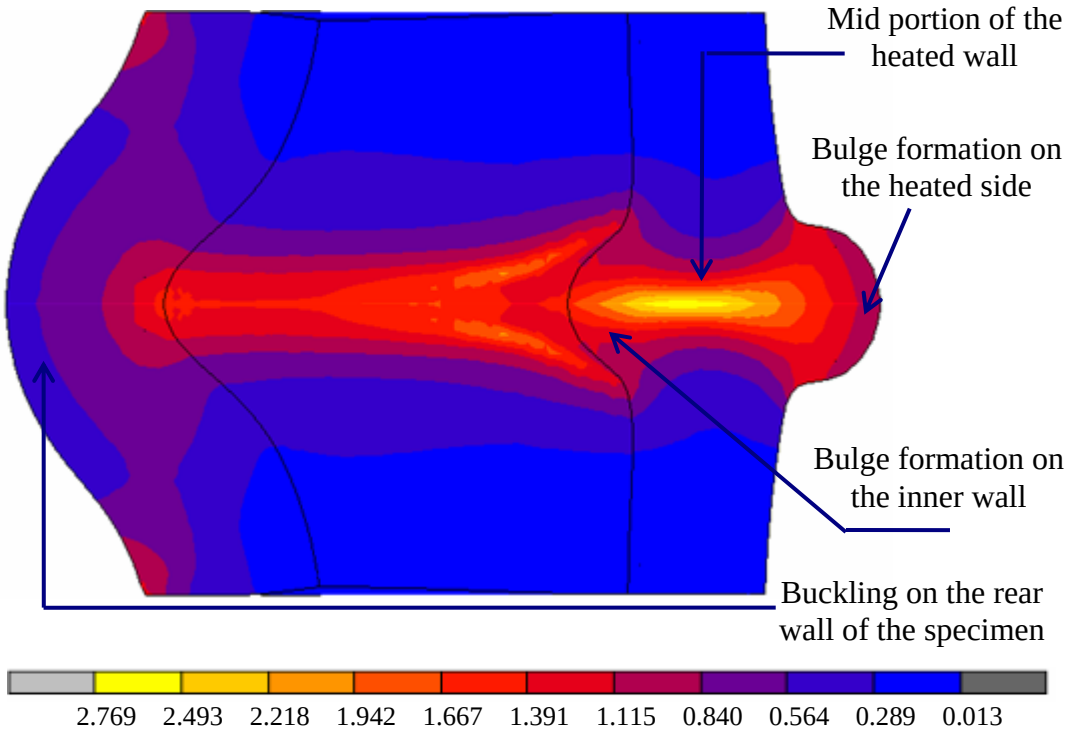

Figure 8.16 The total equivalent plastic strain distribution on the cross sectional area of the workpiece for *Experiment 46*.

In Figure 8.17(a), a detailed photograph of the cross sectional area is presented, and in Figure 8.17(b) the computer simulation of the same experiment shown. The general shape and direction of the flow lines are the same both in the experiment and the simulation results. However, there are some differences on some critical

points on the workpiece. There is a slight difference in the shape and size of the secondary bulge. A smoother shape is obtained in the simulations. The height and width of the bulge is larger in the real specimen.

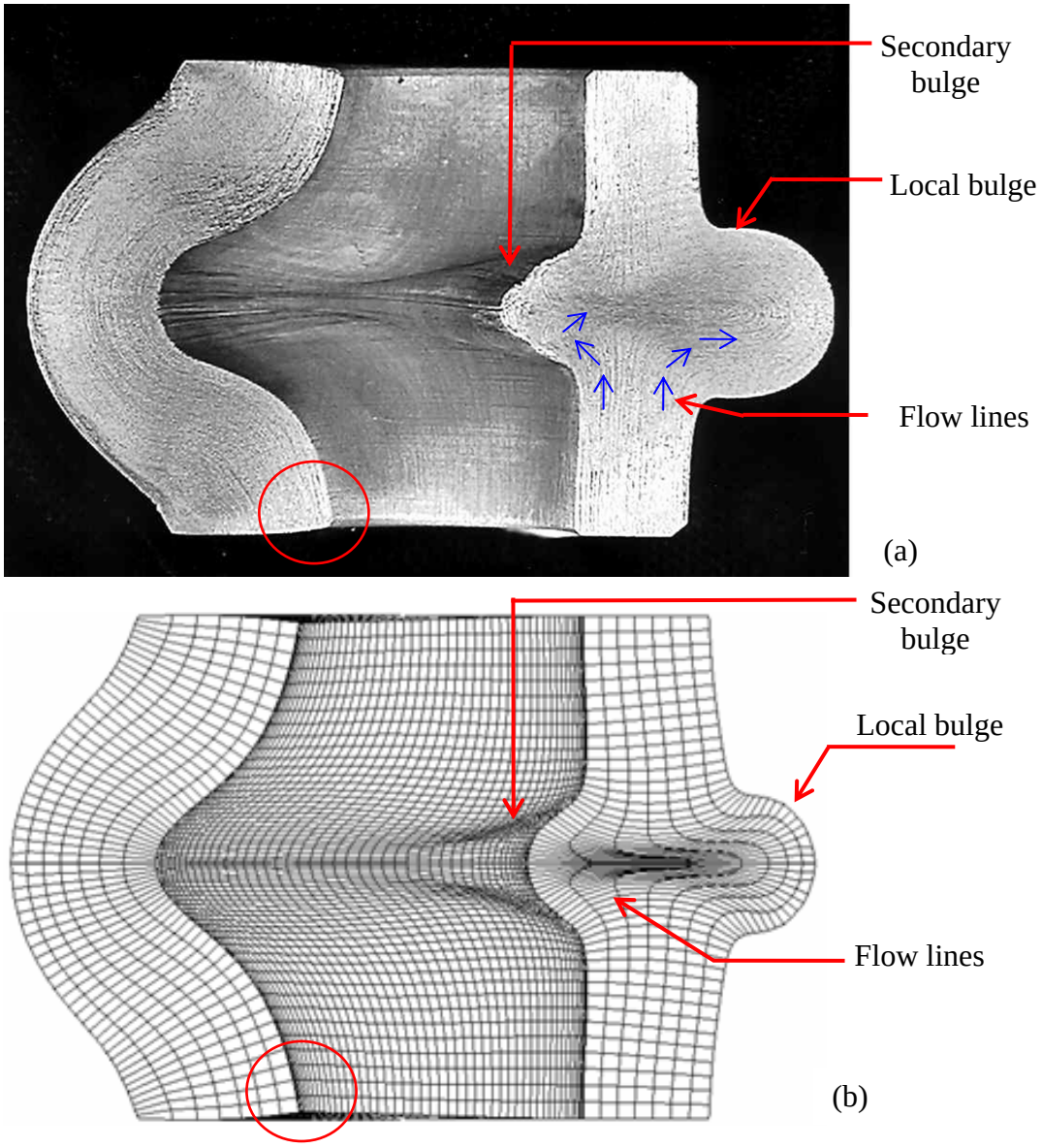

Figure 8.17 The flow lines on the cross section of the workpiece in *Experiment 46* (a) Actual workpiece (b) Result of modified simulation.

Besides the previously mentioned errors, the simulation of *Experiment 46* reflects the nature of the process. The simulations justify an important situation observed in the experiments. The direction of the flow lines near the inner surface of the

specimen wall are simulated well that they follow identical curved paths in both simulation and experiment results. In Figure 8.17(a), the portions showed in circles, which are previously in contact with the dies, start to separate from the die surface. The same situation is also seen in the computer simulation (Figure 8.17(b)). The buckling on the rear side of the specimen is observed in the experimental and calculated results, after a certain relative height reduction is reached.

The cross sectional view of *Experiment 60* and the results of its improved computer simulation are given in Figure 8.18. The secondary bulge formation is observed. The smooth shape of the bulge is obtained in the simulations. However, the most significant error is observed on the rear wall of the specimen.

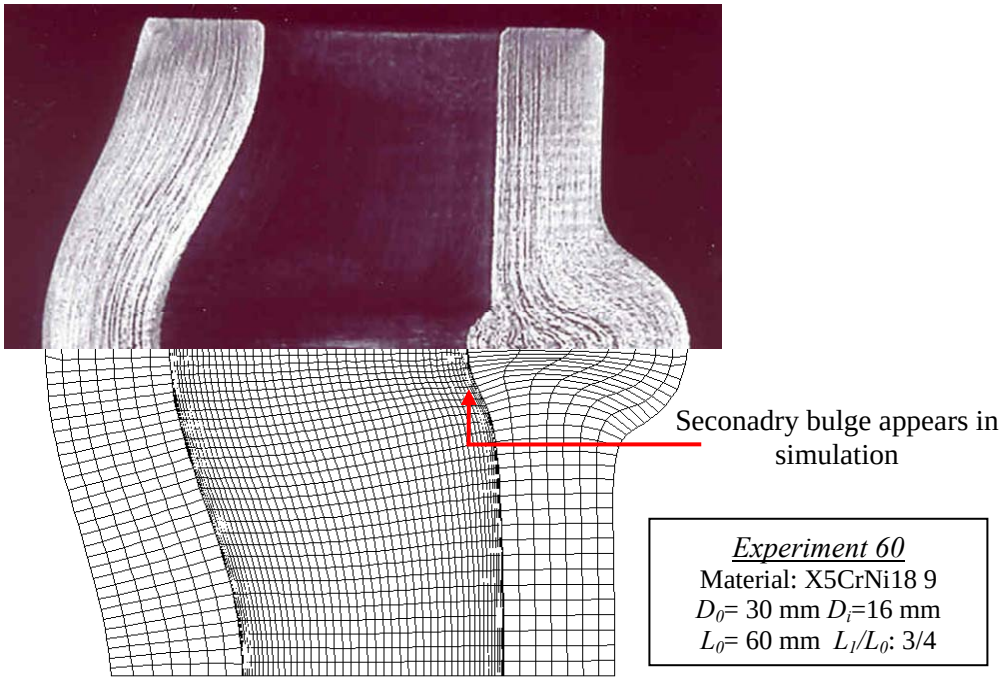

Figure 8.18 The flow lines on the cross section of the workpiece in *Experiment 60* (a) Actual workpiece (b) Result of modified simulation.

The calculated and actual dimensions of the product are given in Table 8.4. The maximum dimensional error is on the bulge width and it is about 25%. The bulge dimensions are under estimated in the calculations.

Table 8.4 Comparison of product dimensions with the numerical results of modified model for *Experiment 60*.

Initial workpiece dimensions (mm)		D_o	D_i	L	Material: X5CrNi18 9 Pyrometer reading (max): 1100°C		
		30	16	60			
		D_{o1}	D_{i1}	L	w_1	w_2	w_3
Final Dimensions (mm)	**Experiment**	30.9	15.5	43.0	43.2	15.0	6.2
	Simulation	32.2	16.7	43.0	41.0	13.0	4.6

Besides the dimensional errors, there are some points that the improved method gives better results than the preliminary calculations. The secondary bulge formation is observed only on the improved method. Also, the shape of the local primary bulge fits the actual specimen better.

8.5.3 Analysis of Forming Solid Workpieces

A Ti6Al4V specimen is selected to present the forming characteristics of the solid specimens in this process. The temperature data obtained from the simulation and experiment are shown in Figure 8.19. It is seen that the two curves fits very well to each other at point P_1.

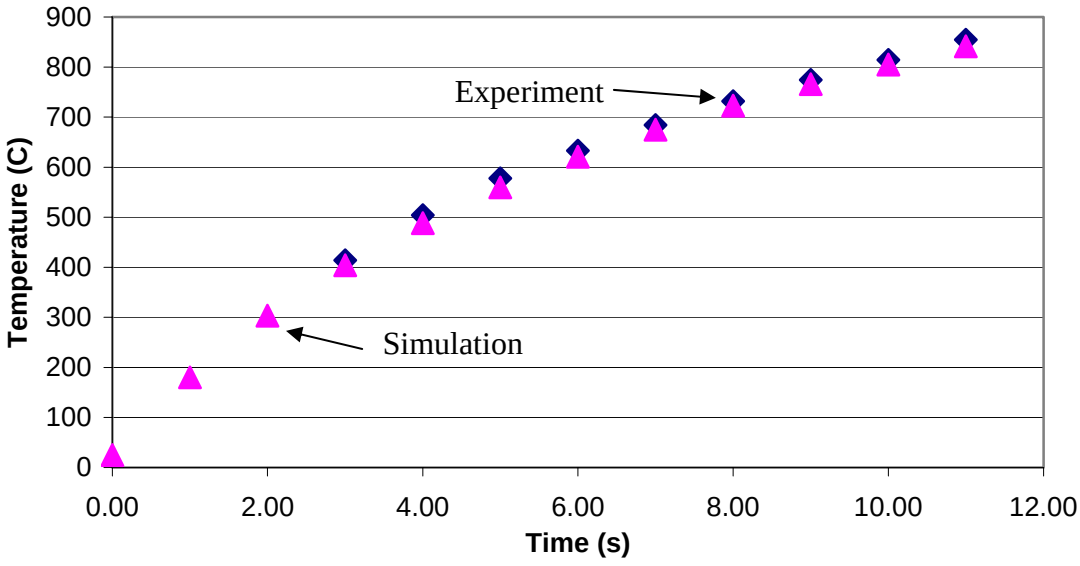

Figure 8.19 The comparison of the temperature curves obtained during the experiments and the simulations for *Experiment 140*.

The cross sectional view of a specific specimen, *Experiment 140*, is shown in Figure 8.20(a). The bulge formation of the locally heated solid workpiece is shown at the end of 0.75 length reduction. The simulation result shown in Figure 8.20(b) represents the analysis of the *Experiment 140.*

In the solid workpieces, buckling is observed on the back side of the specimens as on the hollow specimens. However the shape of the rear wall is not distorted as much as that of the hollow specimens. The direction of the flow lines on the bulge area is oriented identically in the experiment and simulation results. The flow lines are directed to the bulge area. Similar results are obtained for stainless steel and 16MnCr5 specimens.

Crack formation seen in Figure 8.20(a) is observed only in the Ti6Al4V specimens. In applications where the heat generation rate is high due to either high frequency or amplitude of the coil current, a high gradient occurs between the heated and the rear side of the specimens. As the bulge area reaches to high temperatures, the rear side may have a temperature around the room temperature. Cracks may occur due to the low formability of the titanium alloy in low temperatures.

A further comparison of simulations with the experiments is done by analyzing some critical dimensions. The calculated and measured values of some certain dimensions are given in Table 8.5. The final diameter of the specimen is almost exactly, obtained in the calculations. The error in the bulge height and width are 16% and 32%, respectively. However, due to the irregular shape of the bulge and measurement limitations it is probable that some errors are imposed in the measurement. Also, the boundaries of the bulge shape is not exact, therefore approximate values are recorded for these portions. The error in dimensions is within acceptable ranges.

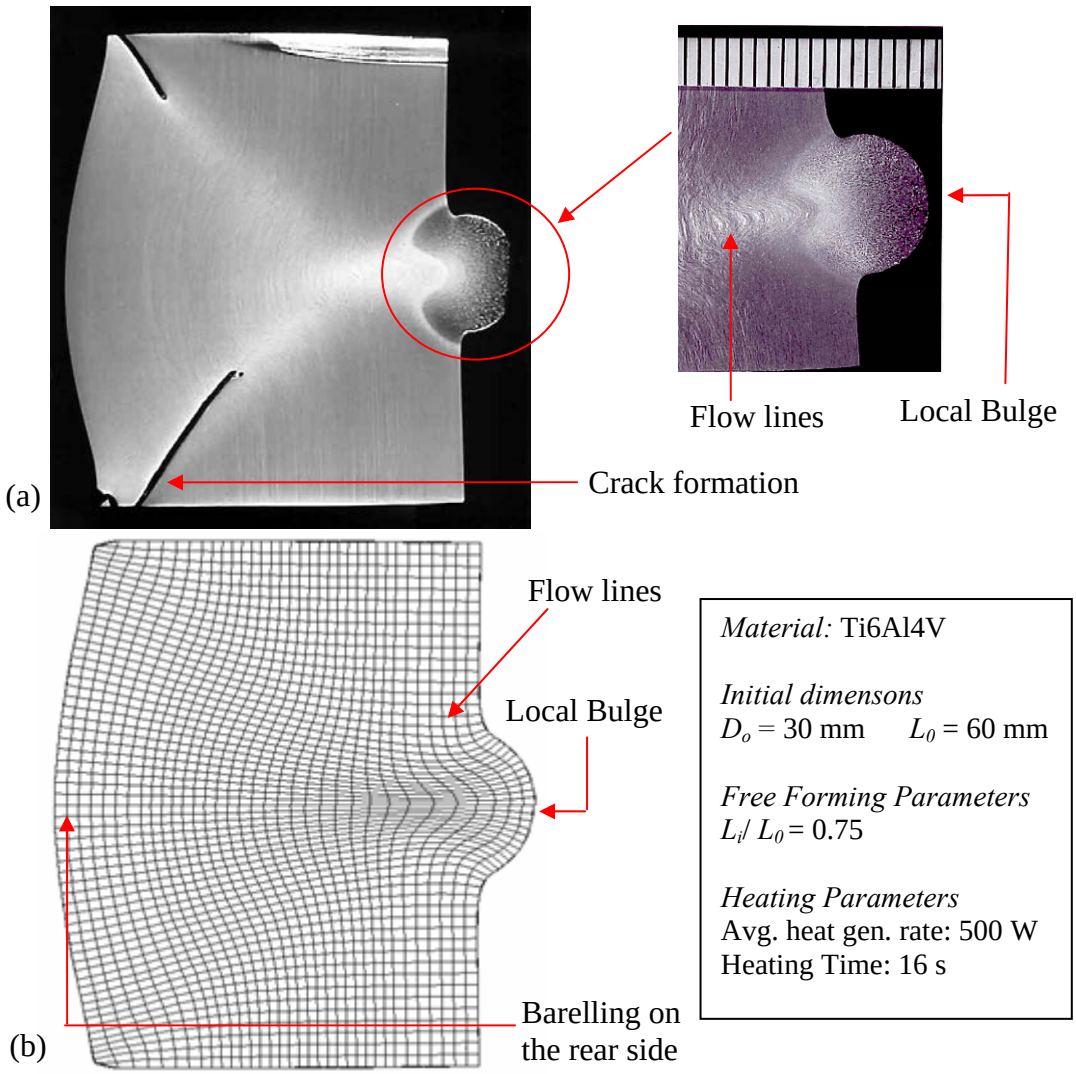

Figure 8.20 The final shape obtained from free forming of a locally induction heated solid workpiece.

Table 8.5 Comparison of product dimensions with the numerical results of modified model for *Experiment 140*.

Initial workpiece dimensions (mm)		**D_o**	**D_i**	**L**	Material: Ti6Al4V Pyrometer reading (max): 85C		
		30	-	60			
		D_{o1}	**D_{i1}**	**L**	**w_1**	**w_2**	**w_3**
Final Dimensions (mm)	**Experiment**	31.6	-	45.0	39.7	15.8	5.8
	Simulation	31.5	-	45.0	41.5	13.3	4.4

The comparison of the numerical and experimental results shows that the improved model of the process is capable of simulating the actual case. Regarding the dimensional errors at some locations on the workpiece, it may appear as if the preliminary simulation of the process is more effective. However, the improved simulation reflects the nature of the process more accurately; therefore, the effects of the process parameters are investigated using this technique.

8.6 Parameter Study

8.6.1 Effect of Heat Generation Rate

In induction heating, the distribution and magnitude of heat generation is dependent on the magnitude and frequency of the coil current, as discussed in Section 7.3.2. In this part, the effect of current magnitude on the temperature distribution and on the geometry of the product is investigated.

The shape of the local bulge on the heated wall of hollow specimens is sensitive to the heat generation rate. In Figure 8.21, the temperature values at point P_1 are presented for two different simulations.

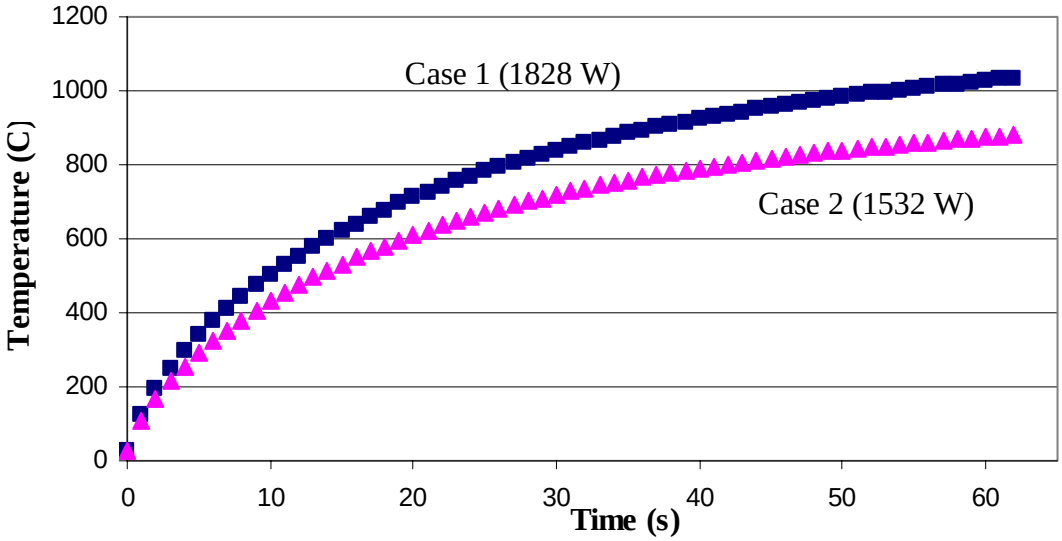

Figure 8.21 The temperature curves obtained from simulations.

Stainless steel (X5CrNi18 9) workpieces are analyzed with outer and inner diameters of 30 mm and 16 mm, respectively. In *Case 1*, the total average heat generation rate within the workpiece is 1532 W, whereas in *Case 2*, this value is 1828 W. The distribution of temperature is shown in Figure 8.22 for *Case 1* and *Case 2*.

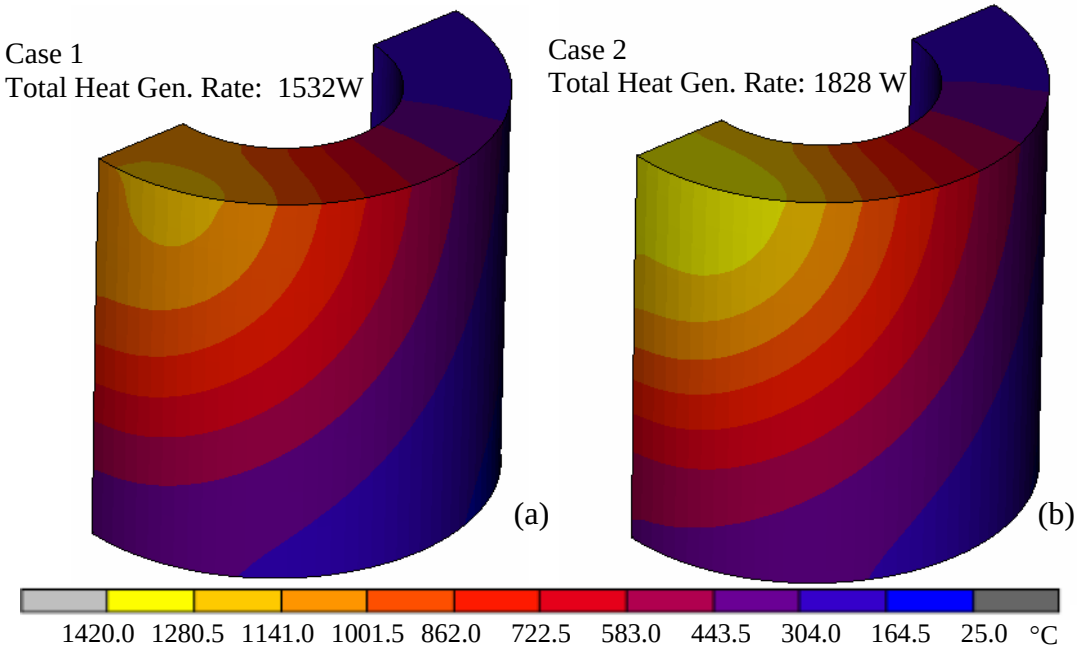

Figure 8.22 The temperature distribution on one quarter of the hollow model at the end of the heating stage. The heat generation rates are 1532 W (a) and 1828 W (b).

The effect of heat generation rate is investigated by analyzing the form of specimens and the flow lines at different stages of free forming. In Figure 8.23, the cross sectional views of the analyses *Case 1* and *Case 2* are given. The ratio of final workpiece length to initial length is 5/6 in Figure 8.23(a) and (b). The formation characteristics on the bulge area differ considerably from each other in the two cases. In *Case 1*, the formation of the hot bulge volume is deformed regularly under the compressive forces applied by the relatively cold side walls above and below the heated region. Material flows to both inner and outer side of the wall in different proportions due to the temperature difference. In *Case 2*, however, the relatively hot portion of the specimen wall is buckled under the loads. The secondary bulge is not observed at this stage. The material loses ability to

resist compressive forces as temperature increases. As the length of the column consisting of hot material increases, the heated wall tends to buckle.

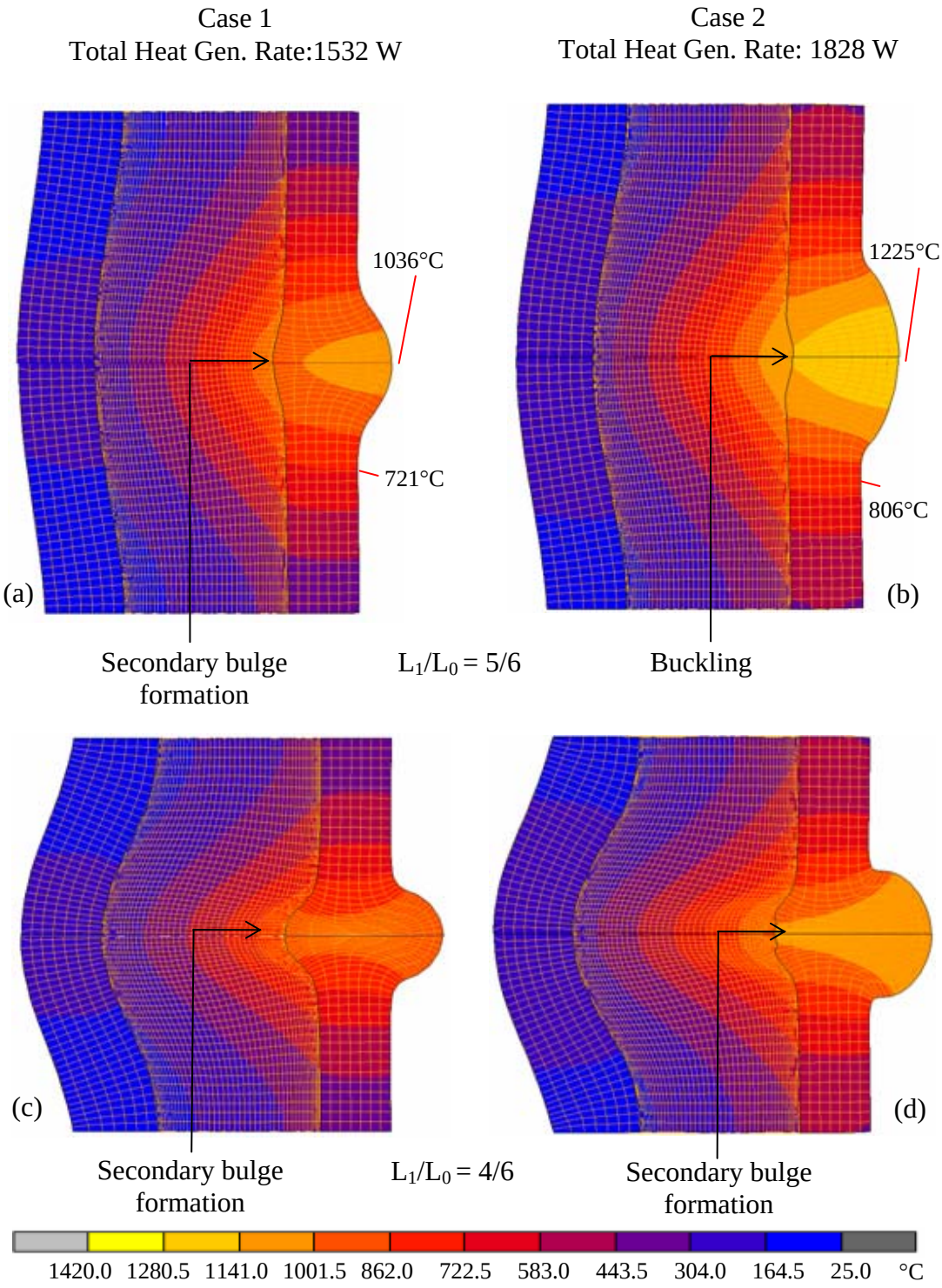

Figure 8.23 Comparison of product shapes for different heat generation rates.

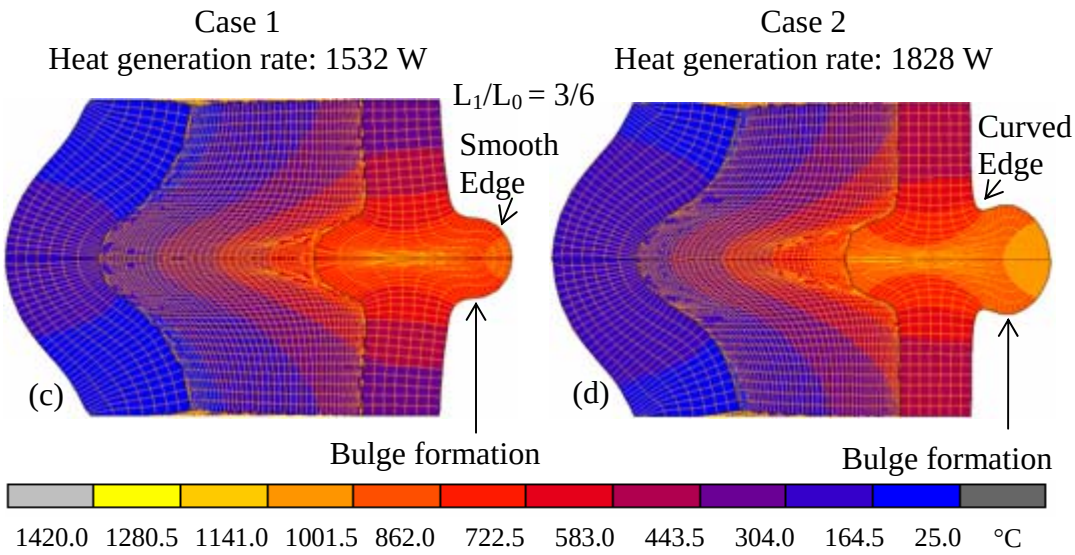

Figure 8.23 Comparison of product shapes for different heat generation rates within the workpiece (continued).

As the process proceeds, the temperature difference between the two sides of the heated wall decreases due to heat diffusion. In *Case 1,* the hot material continues to flow to both inner and outer side of the specimen wall (Figure 8.23(c)). In *Case 2*, the material starts to flow to the inside of the hollow specimen (Figure 8.23(d)). The inclined portions of the walls come into contact with each other and form the secondary bulge. The shapes of the products at the instant that the length of the workpiece reaches ½ of its initial value are given in Figure 8.23(e) and Figure 8.23(f). In *Case 1*, the bulges appearing on the inner and outer sides of the wall have regular shapes with smooth edges. The maximum temperature difference along the wall thickness at the midsection of the heated wall is about 78°C. As the difference decreases during the process, the difference between the amounts of material flowing in the opposite directions decreases. In *Case 2,* the maximum temperature difference is 143°C. The height and width of the bulge on the outer wall of the specimen is considerably larger than the secondary bulge. Also due to the excessive flow of material to the bulge zone and buckling of the heated wall in the initial stages of forming the edge of the bulge is curved as shown in Figure 8.23(f).

Another discrepancy observed between the two cases is that the walls of the workpiece above and below the heated volume at the end of 0.5 length reduction. In *Case 1*, the walls lose their vertical orientation at the last stages of forming. In *Case 2*, however, they remain vertical. Since the hot portion is soft during the process, the side walls above and below this portion moves like a rigid body, without going into deformation as much as in *Case 1*. In *Case 1* on the other side, the maximum value of temperature is considerably less, in the later stages of free forming, the deformation occurs along the entire length of the heated wall.

8.6.2 Effect of Frequency of the Coil Current

The frequency of the coil current has a direct effect on the distribution of heat generation rate within the workpiece. Increasing the coil frequency will decrease the skin depth as explained by Eq. 3.4. In other words, higher frequency values cause a higher proportion of the total heat to be generated near the surface of the workpiece. The effect of current frequency on the temperature distribution and on the shape of the product is investigated on Ti6Al4V specimens. In *Case 1*, the frequency is 7800 Hz whereas in *Case 2* it is 10500 Hz. The values of heat generation rate per unit volume are obtained by the electromagnetic simulations for the given frequencies and 1500 A of current. The values are corrected by a coefficient of 28 in order to reflect the temperature distribution identical to the experiments.

The temperature distribution at the end of 20 s is given for the two cases in Figure 8.24. It has been observed in the electromagnetic simulations that if the frequency is increased, the total heat generation rate is also increased. Furthermore, due to the skin effect, the heat generation is more concentrated near the surface for the high frequency case. Therefore, the temperature on the surface reaches to higher values in *Case 1* than in *Case 2*.

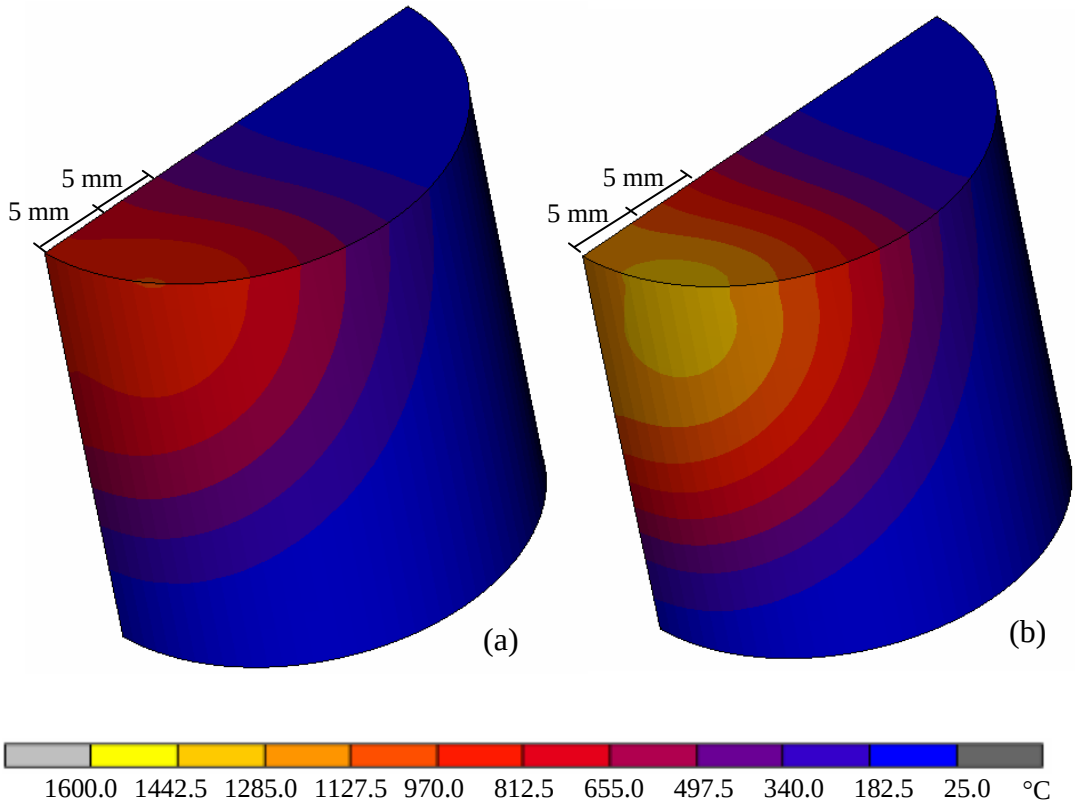

Figure 8.24 The temperature distribution on one quarter of the workpieces for a frequency of (a) 7800 Hz and (b) 10500 Hz

The formed specimens, for which the ratio of final length to initial length is ¾, are presented in Figure 8.25. The width of the local bulge is larger for *Case 2*, in which the frequency is 10500 Hz. Higher temperature in the heated zone leads to more material flow into the bulge. Although the height of the local bulge is almost the same for the two cases, the width is about 25% larger in the high frequency case than in the low frequency case. In practical application, the arrangement of frequency is simple in an induction heating machine within a certain range. Therefore, frequency arrangement is a useful way of obtaining the desired product shape.

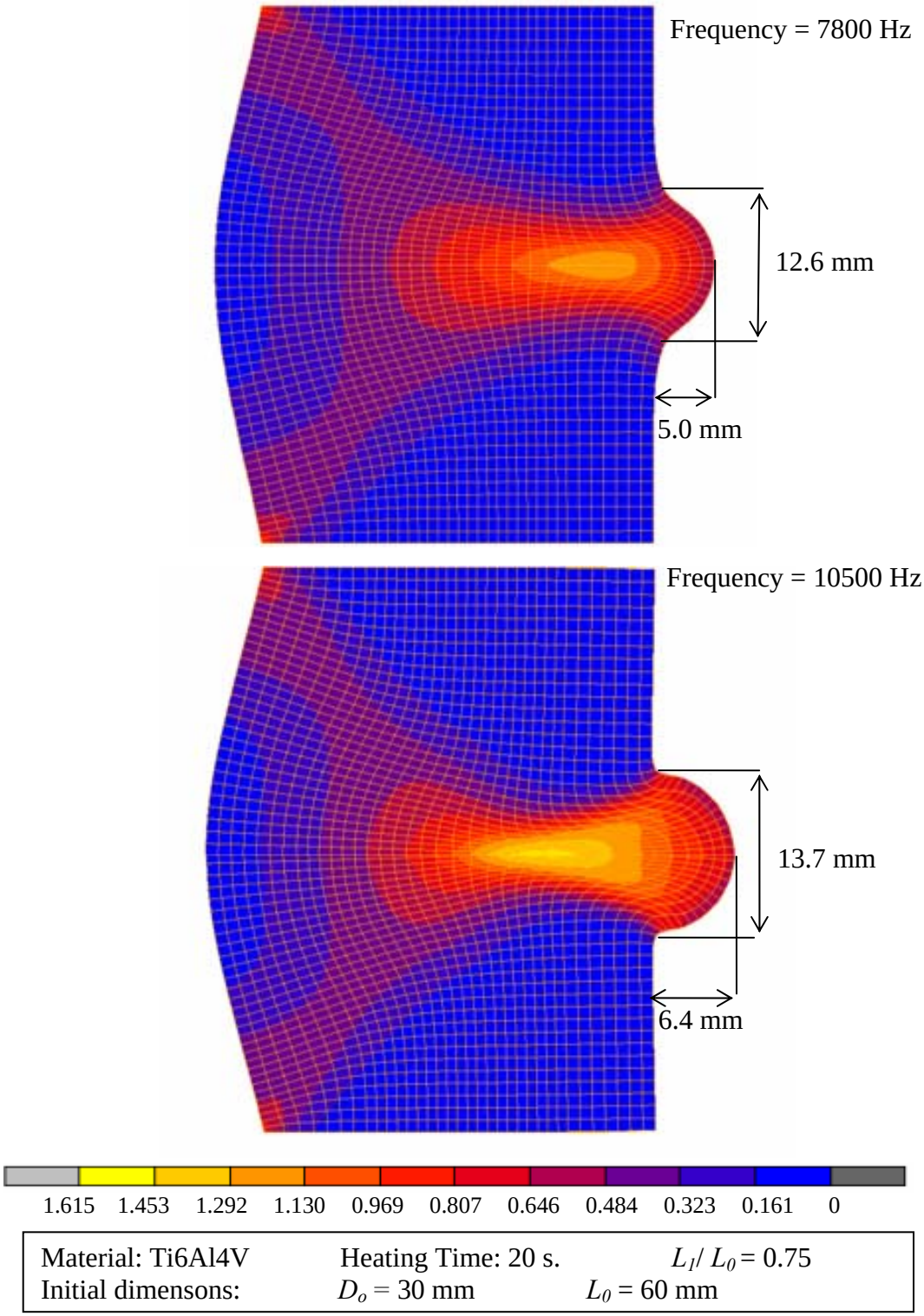

Figure 8.25 The total equivalent strain distribution on one quarter of the workpieces for a frequency of (a) 7800 Hz and (b) 10500 Hz

8.6.3 Effect of Geometry

The wall thickness of the hollow specimens is one of the main parameters that determine the deformation characteristics under compressive loads after local heating. The deformations of two hollow specimens, which are identically heated and formed, are presented in this section. In *Case 1*, the ratio of the inner diameter to outer diameter is 0.73 whereas in *Case 2* it is 0.53. The heat generation data is obtained for 7800 Hz of frequency and 1500 A of current. The heat generation rate is corrected by a factor of 20 in both cases. The temperature distribution at the end of 27 s is given in Figure 8.26.

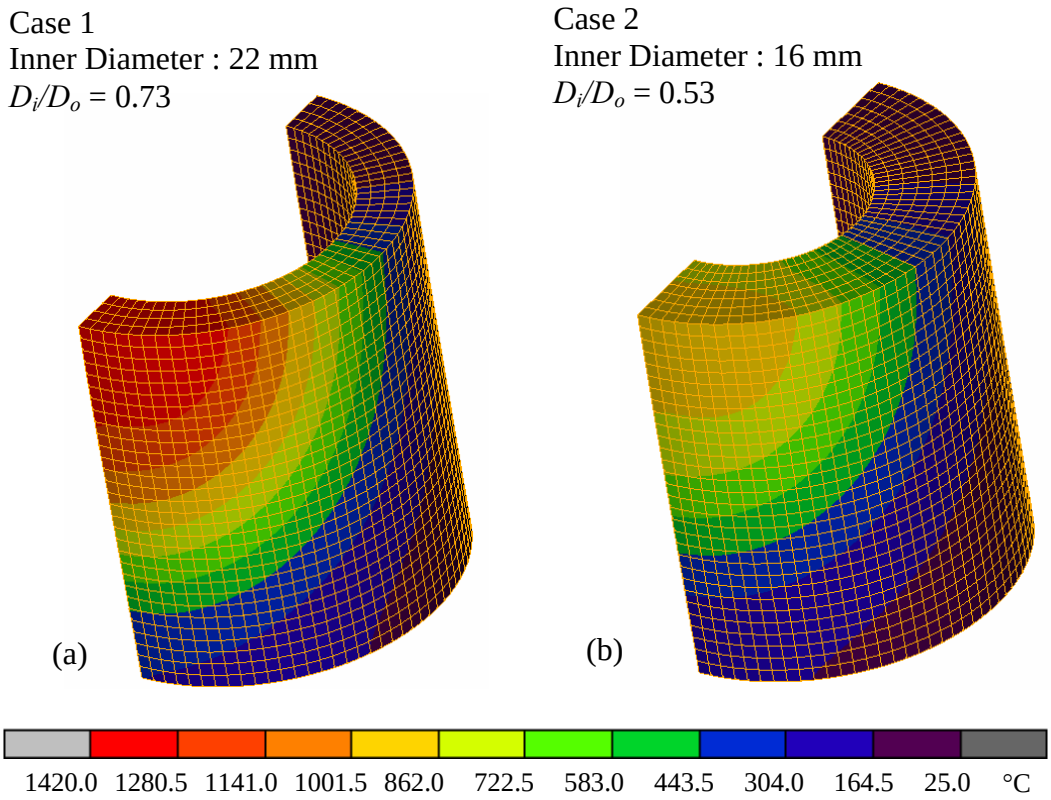

Figure 8.26 The temperature distribution in hollow specimens with ratio of inner diameter to outer diameter of (a) 0.73 and (b) 0.53.

The total heat generation in the thin walled cylinder (*Case 1*) and thick walled cylinder (*Case 2*) are 1810 W and 1530 W, respectively. Therefore, higher

temperatures are obtained in *Case 2* when identical heating processes are applied. The cross sectional views of the formed specimens are presented in Figure 8.27. The punch speed is 3.7 mm/s in both cases. In *Case 1*, the workpiece tends to buckle under the compressive loads. In the beginning of the forming process, the heated wall of the workpiece buckles (Figure 8.27(a)). The heated wall folds over itself as the forming process proceeds (Figure 8.27(c)). The side walls above and below the heated volume retain their vertical orientation. The percentage change of thickness of the side walls is 6% after 50% length reduction.

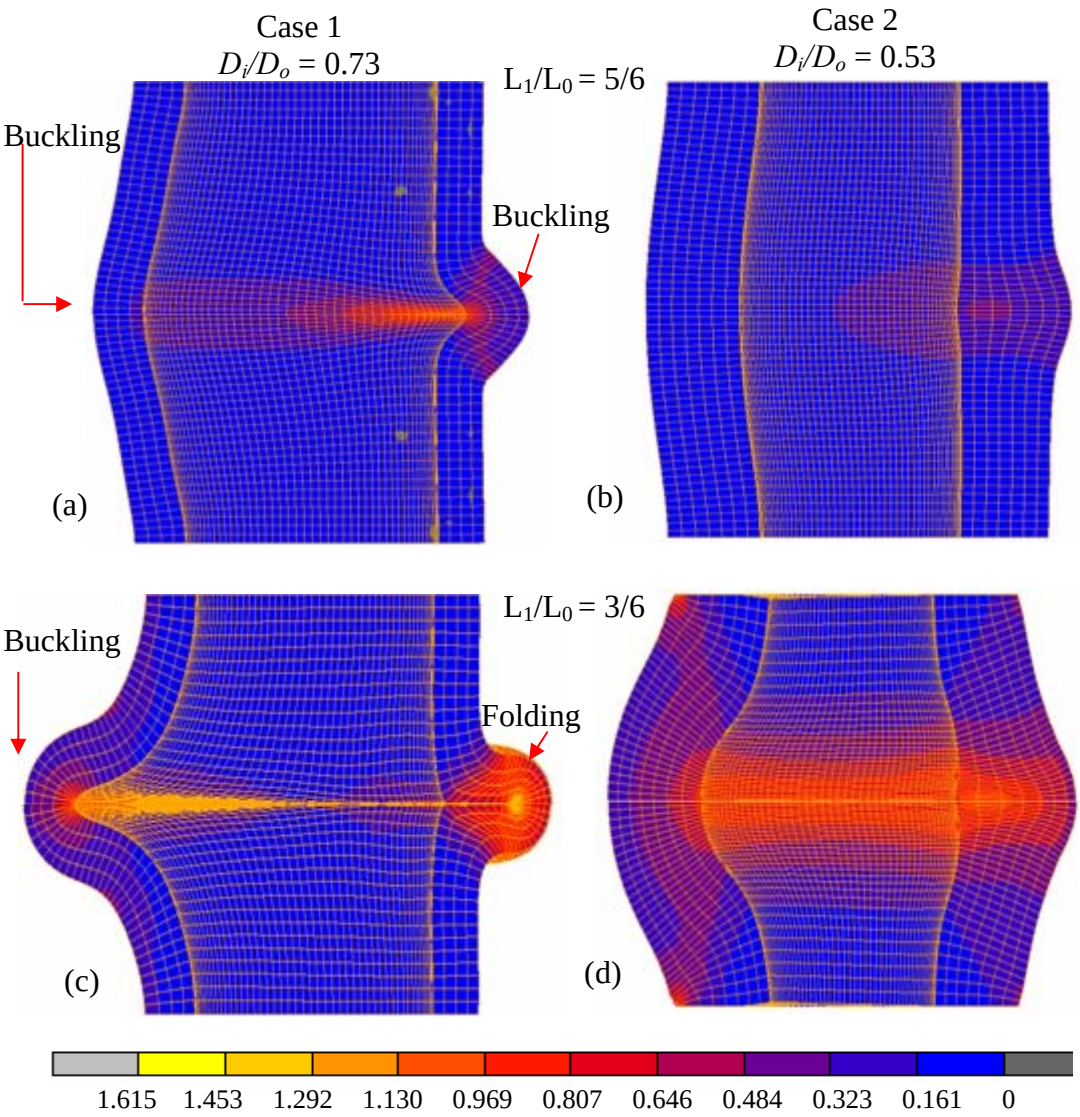

Figure 8.27 The total equivalent strain distribution on one quarter of the workpieces for a ratio of inner to outer diameter of (a) 0.73 and (b) 0.53.

On the other side, in *Case 2*, in which the wall thickness of the specimen is 7 mm, buckling is not observed on the heated volume at the first stages of forming (Figure 8.27(b)). The two main reasons of this situation are lower temperature values and the higher resistance of the material to compressive loads due to the thicker walls. The product obtained from the thick walled specimen is shown in Figure 8.27(d). The local bulge is not formed, the deformation is relatively homogeneous.

The results obtained for *Case 1* is also compared with *Experiment 59*. The flow lines on the cross sectional view of the specimens are presented in Figure 8.28. In the figure, a detailed photograph of the upper half of the cross sectional area is presented, which is completed on the lower side, with the computer simulation of the same experiment. The flow lines, buckling and the folding of the walls are in accordance with the experiments. The shape of the rear walls of the specimen is distorted. A wavy formation due to buckling is seen along the wall of the specimens.

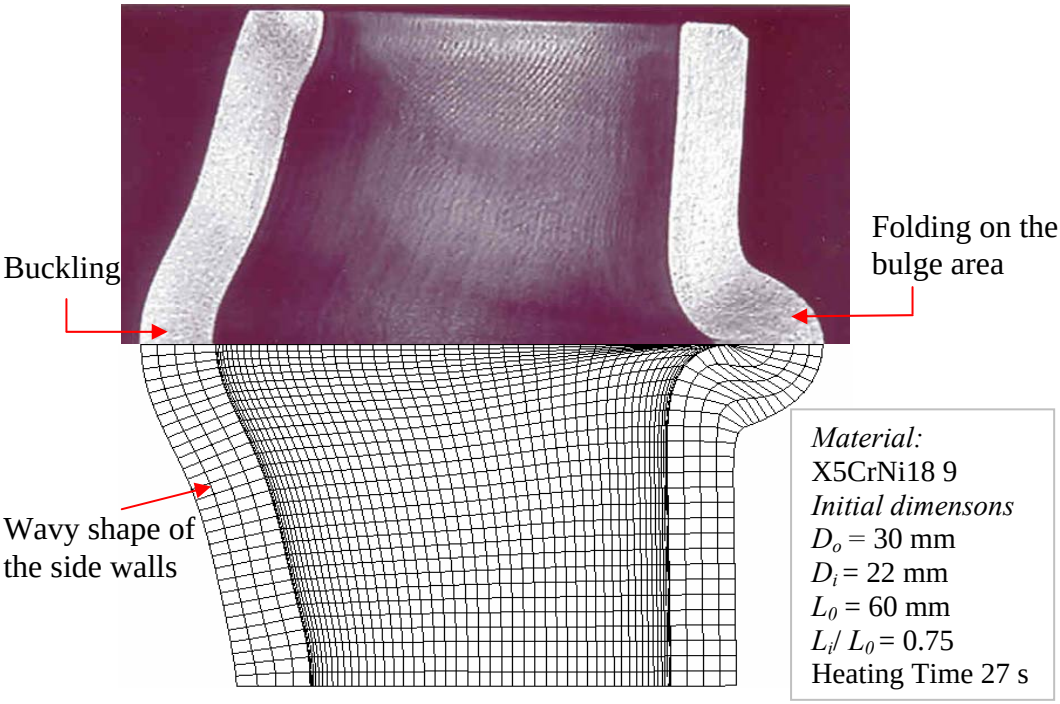

Figure 8.28 The comparison of the simulation results with the experiment for *Experiment 53*.

8.6.4 Effect of Punch Speed

The punch speed is an important parameter that affects the final shape of the product. The contribution of the punch speed to the overall process arises from the direct dependency of the process time on this parameter. As the punch speed is decreased the forming time increases. Therefore, heat diffusion within the workpiece is enabled and the temperature distribution becomes more homogeneous in low punch speed cases compared to high speed applications. The effect of this parameter is investigated on the products obtained by 3 different punch speeds. In Figure 8.29, the cross sectional views of the specimens, which are formed with punch speeds of 1.85 mm/s, 3.7 mm/s and 18.5 mm/s. In case of low speed forming (Figure 8.29(a)), the width of the local bulge is considerably smaller than that in case of higher forming speeds (Figure 8.29(b)-(c)). Since the temperature distribution becomes more homogeneous during forming at lower punch speeds, the deformation is not dominated on the bulge area as much as in cases with higher punch speeds. However, when the forming time is shorter, the high temperature gradient around the heated zone is preserved as it is at the end of the heating stage. Relatively hot volume of material flows in the outward direction, forming a bulge.

The punch force vs. displacement curves of the three processes mentioned above are presented in Figure 8.30. For the three cases, as the punch speed is increased, the total applied force decreases. This situation contradicts with the fact that flow stress of the material increases as the strain rate is increased. However, high formability of the material is retained during the process due to higher temperature values in the high punch speed cases. It compensates for the effect of high strain rate and in turn results in lower punch forces. However, it should be kept in mind that in applications, in which the maximum temperature at the end of heating stage is lower than the current case or the temperature gradient within the workpiece is higher such that the rear side of the workpiece have lower temperatures, the effect of temperature on flow stress may not compensate the effect of strain rates. Higher punch speeds may require higher forming forces in those cases.

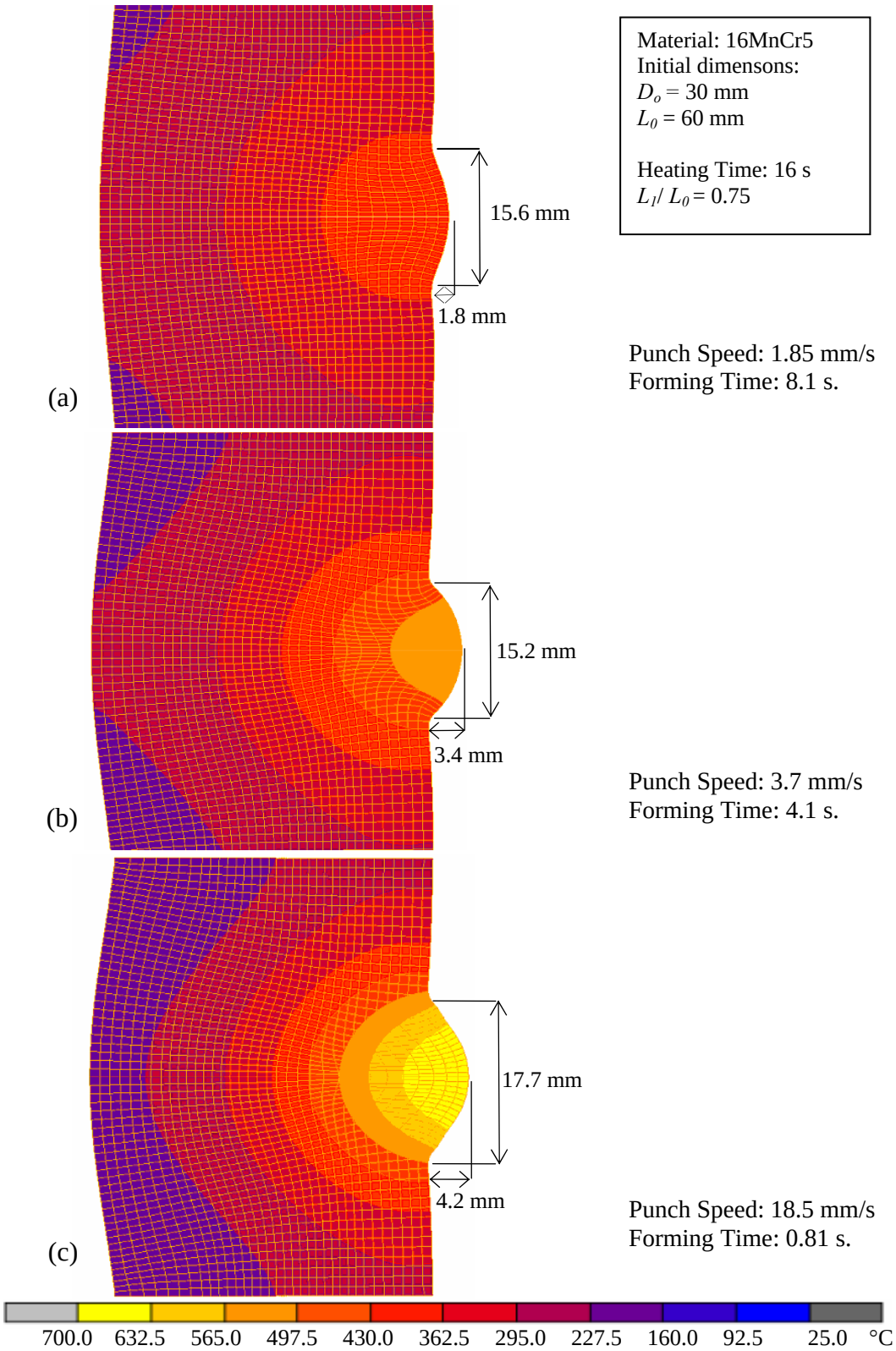

Figure 8.29 Temperature distributions at the end of forming for processes with different punch speeds.

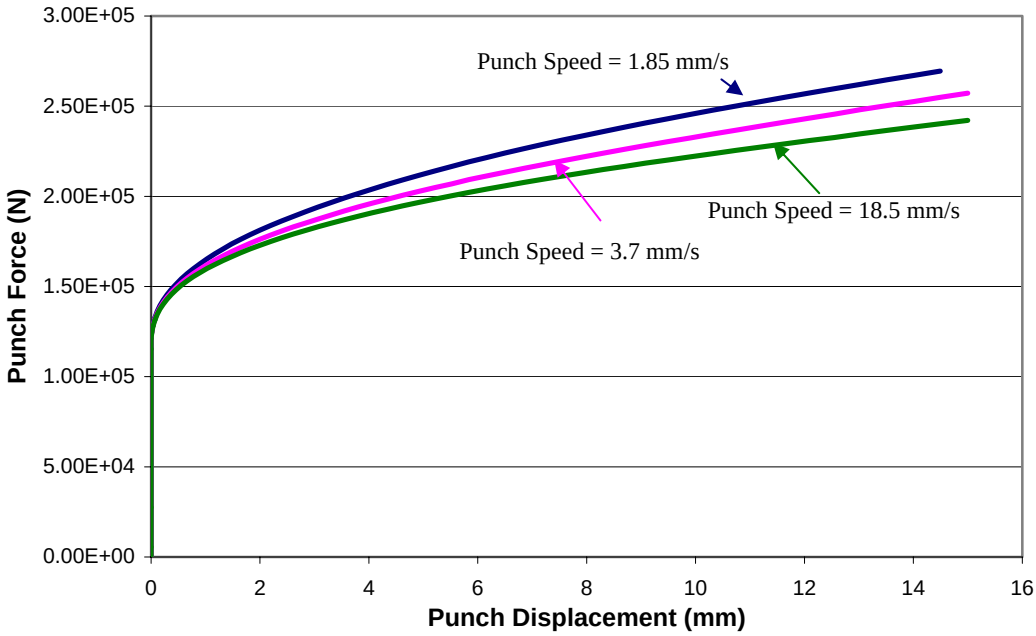

Figure 8.30 Effect of punch speed on the punch force required in free forming.

8.6.5 Effect of Material

It is a complicated procedure to compare response of different materials since materials have different sets of combinations of some properties. The thermal and mechanical properties of the material determine the mode of deformation.

The investigations on the process show that, the temperature distribution in the workpiece is one of the crucial parameters that determine the final shape of the product. Local deformations can be obtained if a temperature gradient is created between the surface and the inner portion of the workpiece, by a proper arrangement of the coil current and the duration of heating. Each of the properties like thermal conductivity, thermal diffusivity and material dependent process parameter skin depth has considerable effect on temperature. Furthermore, investigating the response of a material to the process parameter may not give adequate information about the response of other materials, which are not included in the study. Therefore, in this section, the temperature distribution within the

workpiece is formulated analytically and non dimensional parameters are derived, a certain value of which describes identical dimensionless temperature distributions in different materials.

In induction heating process, in which the heat generation rate on the surface of the specimen is homogeneous, the heat generation rate inside the solid is defined as a function of distance from the surface as

$$g(x) = g_0 e^{-\frac{x^2}{\delta^2}} \tag{8.1}$$

where, g_0 is the value of the rate of volumetric heat generation on the surface and δ is the skin depth. The heat diffusion equation for 1-D transient conduction is written as

$$\rho c \frac{\partial T}{\partial t} = k \frac{\partial^2 T}{\partial x^2} + g(x) \tag{8.2}$$

The heat loss due to radiation is neglected in the current analysis. The variables in Eq (8.2) can be rewritten in non dimensional form. The non dimensional distance is defined as

$$\bar{x} = \frac{x}{L} \tag{8.3}$$

where x is the distance from the surface of the specimen and L is the selected characteristic dimension of the specimen. The non dimensional time is

$$\tau = \frac{\alpha t}{L^2} \tag{8.4}$$

where, α is the thermal diffusivity of the material and t is the heating time. The non dimensional term for temperature is defined as

$$\theta = \frac{T - T_\infty}{\Delta T_{ref}} \tag{8.5}$$

where T_∞ is the ambient temperature and ΔT_{ref} is a reference temperature to be defined later in this text. Substituting Eqs. (8.3)-(8.5) to Eq (8.2) and rearranging the terms the following equation is obtained.

$$\frac{\partial \theta}{\partial \tau} = \frac{\partial^2 \theta}{\partial \bar{x}^2} + \frac{g_0 L^2}{k \Delta T_{ref}} e^{-\bar{x}^2 \left(\frac{L}{\delta}\right)^2} \tag{8.6}$$

In the current induction heating application, the specimen has a cylindrical shape and the spatial heat generation pattern is complex on the surface of the workpiece. However, the heating process can be approximated by assuming a plane wall on which the heat is generated on a ring shaped volume that extends from the surface to twice the skin depth of the material. This idealized distribution is shown schematically in Figure 8.31.

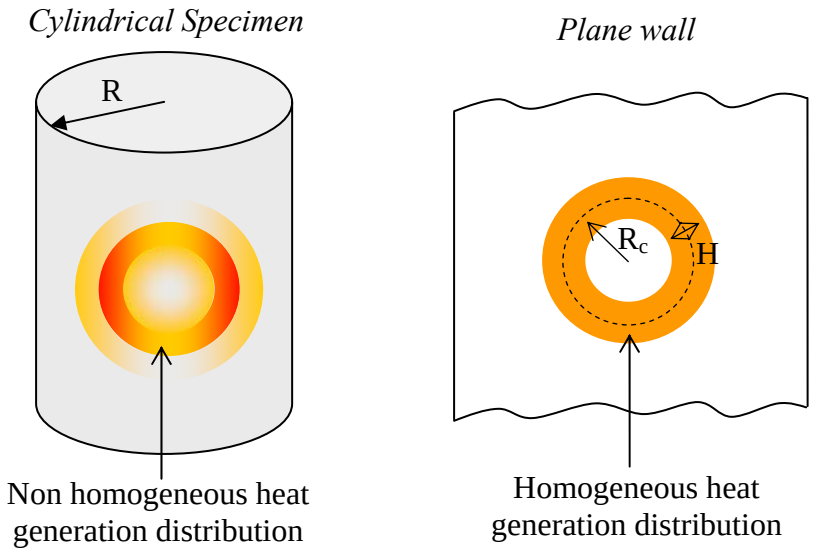

Figure 8.31 Schematic representation of the idealized heat generation distribution.

The reference temperature, ΔT_{ref}, is defined as the average temperature increase near the surface. It is defined regarding a lumped approach in determination of

energy balance. In the early stages of heating, the energy balance equation can be written as follows:

$$\bar{g}Vt = \rho c_p V \Delta T \tag{8.7}$$

where, $\bar{g}$ is the average heat generation near the surface, V is the volume, ρ is the density, c_p is the heat capacity. Eq. (7) can be rearranged as

$$\Delta T = \frac{L^2 \bar{g}}{k} . \frac{\alpha t}{L^2} \tag{8.8}$$

ΔT_{ref} is defined as the temperature at the instant when Fourier number, $\alpha t/L^2$, is 0.2.

$$\Delta T_{ref} = \frac{L^2 \bar{g}}{k} \tag{8.9}$$

Defining the reference temperature on a sufficiently small volume, the average heat generation may be approximated as the heat generation on the surface, g_0.

$$\Delta T_{ref} = \frac{L^2 g_0}{k} \tag{8.10}$$

On the other hand, the total heat generation can be calculated by integrating the heat generation function in induction heating over the idealized heat generation volume. Defining r as the radius of an infinitesimal ring, with a thickness dr, within the heat generation volume and x as the distance of a point from the surface of the plane wall, the total heat generation is written as

$$G_{total} = \int_{R_0 - 0.5H}^{R_0 + 0.5H} 2\pi r dr \int_0^{2\delta} g_0 e^{-\frac{x^2}{\delta^2}} dx \tag{8.11}$$

integration of which gives,

$$G_{total} = 2\pi erf(2) R_c H \delta g_0 \tag{8.12}$$

Substituting Eq.(8.12) in Eq.(8.10), the reference temperature is defined as a function of the heat generation on the surface as

$$\Delta T_{ref} = \frac{L^2 G_{total}}{(2\pi erf(2) R_0 H)\delta k} \tag{8.13}$$

The differential equation given by Eq.(8.6) can be rewritten as

$$\frac{\partial \theta}{\partial \tau} = \frac{\partial^2 \theta}{\partial \bar{x}^2} + e^{-\bar{x}^2\left(\frac{L}{\delta}\right)^2} \tag{8.14}$$

Eq.(8.14) states that defining the reference temperature as a function of the heat generation rate on the surface of the specimen, the dimensionless temperature distribution is independent of the material properties and the total heat applied to the material. It is a function of the parameter L/δ only. Therefore, a unique dimensionless temperature vs. dimensionless time curve is expected to represent the actual case regardless of the material and amount of heat generation for small time, when the diffusion of heat is restricted to a small domain in the neighborhood of the heat generation volume.

The effectiveness of the idealized model, which discards the curvature of the surface and the resulting non-homogeneous heat generation pattern, in reflecting the nature of the actual process is evaluated by means of numerical calculations. In these calculations, the reference temperatures are taken as the same for all three materials. Since the temperature dependence of the material properties is not taken into consideration in the derivation of the idealized model, they are also kept constant in the simulations, to enable comparison.

The dimensionless temperature (θ) values of the three material are plotted in Figure 8.32. The temperature data of two different points are given for each of the

materials. The location dented as *Point 1*, is the location where the maximum heat is generated on the surface. The other location, *Point 2*, is the point that lies opposite to the center of the coil and therefore is located on the middle of the heat generation volume.

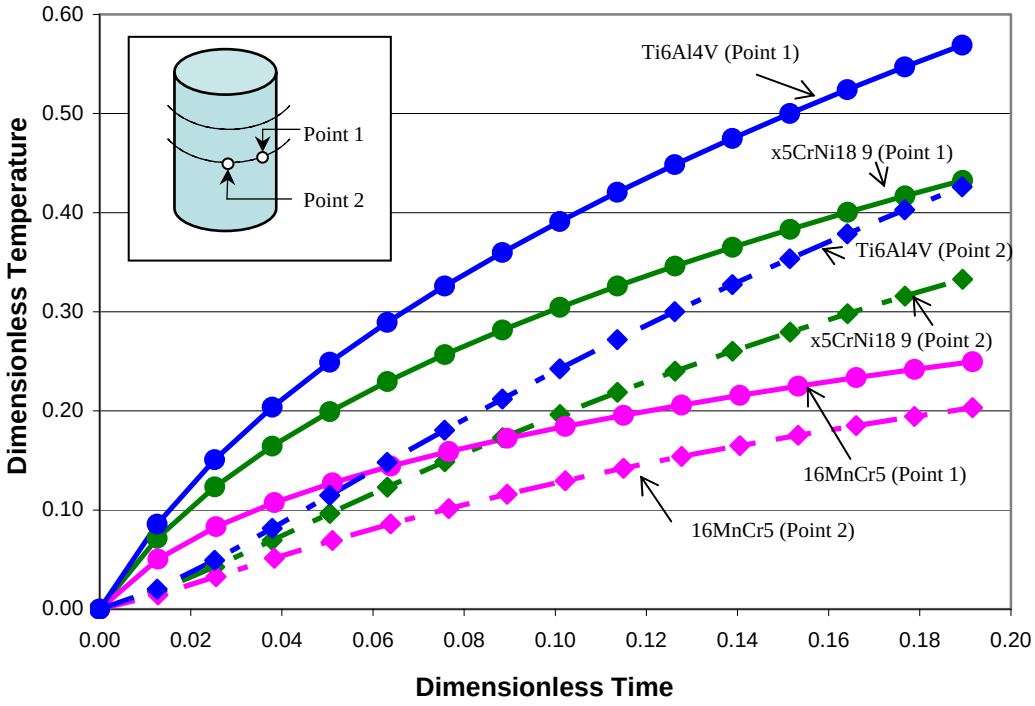

Figure 8.32 The dimensionless temperature vs. dimensionless time curves.

The dimensionless temperature curves of different materials at a certain point are expected to be coincident. However, in Figure 8.32, it is clearly seen that this situation is not realized in the numerical calculations. The probable reason of the deviation of the numerical results from the expected behavior is the capability of the virtual model in approximating the heat generation on the workpiece. In the thermo-mechanical model, the heat generation near the surface is approximated. In the electromagnetic analysis, the heat generation on the surface is equal to the generation on the center of the surface element. In the application of the heat generation values to the thermo mechanical model, the average of the two elements on the below the wall thickness of the specimen is applied to the surface element of the model. Therefore, the heat generation on the surface is less than the exact value.

The ratio of the numerical values of the surface heat generation to the exact values is given in Table 8.6.

Table 8.6 The ratio of heat generation in the elements to generation on surface.

	Ratio of heat generation in the 1st element in EMAG analysis to actual generation on the surface	Ratio of heat generation in 2nd the element in EMAG analysis to actual generation on the surface	Ratio of heat generation in the 1st element in thermal analysis to actual generation on surface
Ti6Al4V	0.989	0.907	0.948
X5CrNi18 9	0.973	0.785	0.879
16MnCr5	0.887	0.339	0.613

As seen in Table 8.6, for the Ti6Al4V specimen the heat generation on the surface is about 95% of the exact value. However, for 16MnCr5 specimen only 61% of the actual value is applied in the numerical calculations. Therefore, the reference temperature should be corrected for the evaluation of numerical simulations. Since the reference temperature is directly proportional to the heat generation on the surface, it is modified by multiplying its exact value with the average coefficient given in Table 8.6. The modified values of dimensionless temperature are given in Figure 8.33. The temperature curves approach to the analytical behavior as expected.

The dimensionless temperature values may better be evaluated by presenting the ratio of the dimensionless temperature values of two materials. Since the best approximation is obtained for Ti6Al4V the ratio of the other two materials to the Titanium alloy is presented in Figure 8.34. The comparison of dimensionless temperature is done on three different points. The location of *Point 1* and *Point 2* are explained above. The *Point 3* denotes the location on the heat generation volume, where the heat generation is least on the surface. As seen in the figure, the ratio of dimensionless temperature of X5CrNi18 9 specimen to that of Ti6Al4V is about 0.85. The temperature ratio of the 16MnCr5 specimen to the titanium alloy is about 0.75.

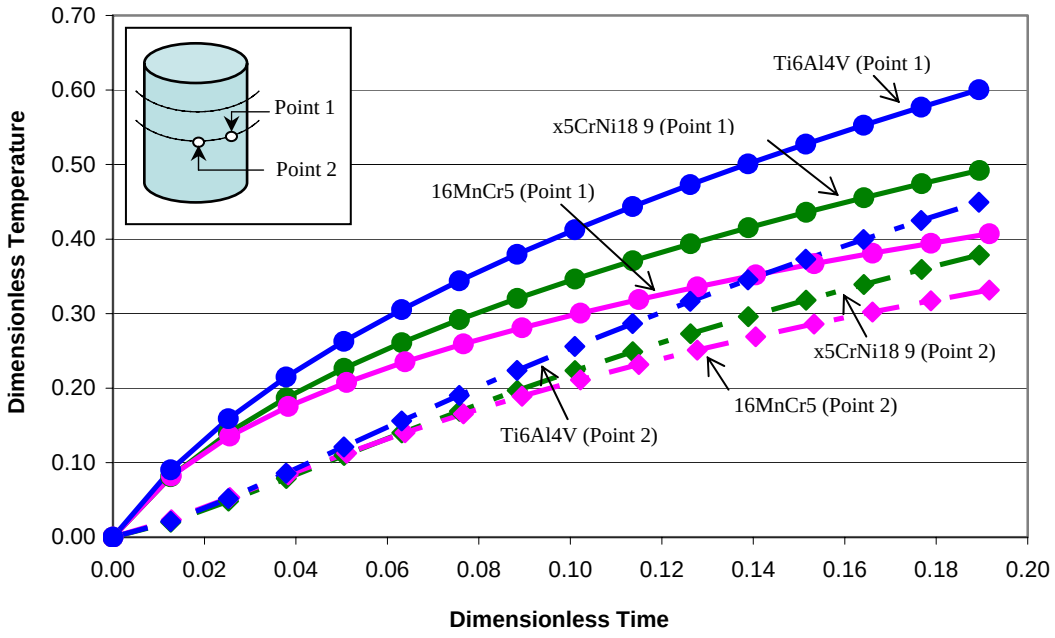

Figure 8.33 The dimensionless temperature vs. dimensionless time curves for modified reference temperature.

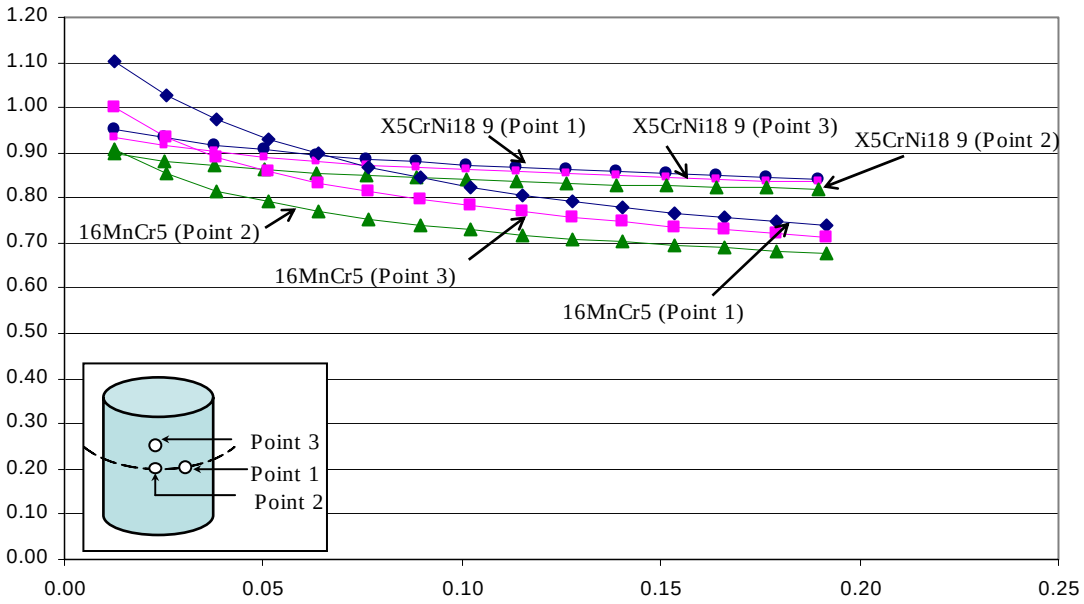

Figure 8.34 The ratio of dimensionless temperature of X5CrNi18 9 and 16MnCr5 to Ti6Al4V at different locations.

The maximum deviation of the dimensionless temperature curves obtained in the simulations from the expected result is about 25% for the materials investigated. On the other side, the dimensionless temperature curves have a consistent trend, such that the ratio of the values for two different materials is almost the same for different points on the surface. Therefore, they can be used in prediction of temperature distribution on the surface of different materials within an acceptable error range especially if the material constants are close to the current materials. Furthermore, they can be used in prediction of temperature distribution of the same materials in case of various combination of heating parameters.

The relative temperature values of the certain locations on the surface of the specimen are consistent for the selected materials. In Figure 8.35, the ratio of *Point 2* to *Point 3* and *Point 1* to *Point 3* are plotted for the three materials. The ratio of *Point 2* to *Point 3* denotes the maximum temperature difference on the surface of the material within the heat generation volume. The curves maximum difference is about 15% and observed between Ti6Al4V and 16MnCr5.

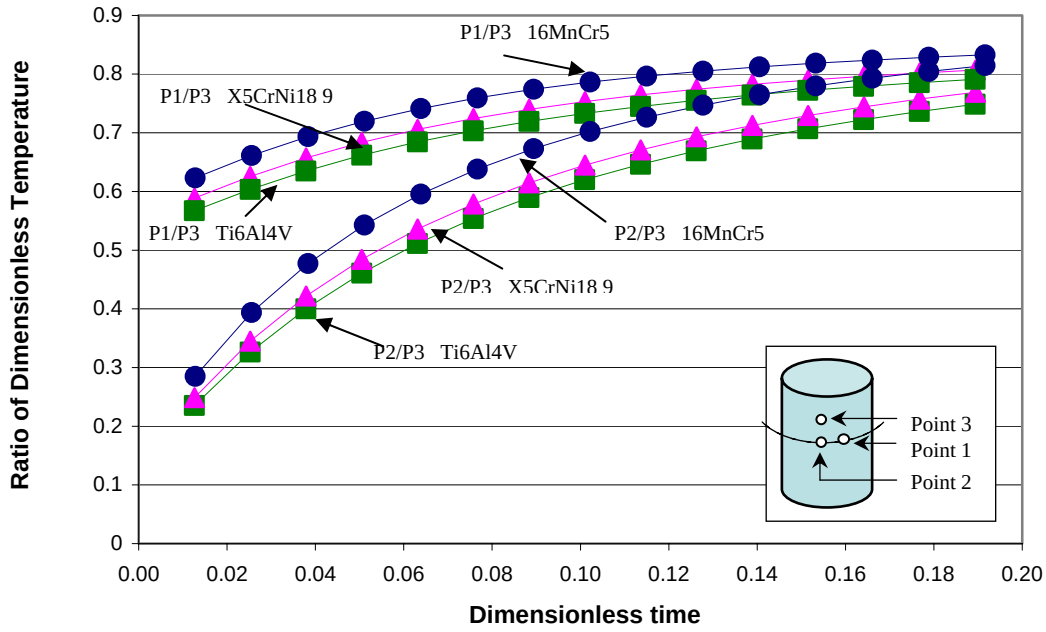

Figure 8.35 Comparison of surface temperature.

The effect of material properties on the process can be better visualized if a set of values of total heat generation and process time needed to obtain identical temperature distribution within the workpiece are compared. The set of data used in the calculations above are presented in Table 8.7. For equivalent temperature distribution on the workpieces 16MnCr5 should be heated by inducting a higher heat generation rate within a smaller time interval. Ti6Al4V requires larger time interval and smaller heat generation. This situation is directly related to the thermal properties of the materials. Higher thermal diffusivity of 16MnCr5 enhances heat conduction. A sufficiently steep temperature gradient can be obtained only if the process time is less compared to the other materials.

Table 8.7 The heat generation values and heating time for the materials.

Material	Heating Time (t)	Total Heat Generation Rate (W)
16MnCr5	3.4 s	1085 W
X5CrNi18 9	10.9 s	725 W
Ti6Al4V	15 s	573 W

The temperature distribution one of the major factors that determine the product shapes. If identical temperatures are obtained, the localization of material flow is determined by the sensitivity of the flow stress to temperature. If rapid changes are observed on the flow stress with temperature, local deformations are expected to be obtained. If identical bulge dimensions are desires on different materials, the time of the free forming process should also be arranged regarding their thermal properties, since the temperature distribution during forming determines the material flow.

8.7 Conclusion

In this section the reliability of the numerical model in representing the actual process is investigated. It is seen that the hollow and solid models are capable of

representing the formation characteristics of the specimens observed in the experiments. It is proved in the numerical simulations that some process parameters like the magnitude and frequency of the coil current, punch speed and the workpiece geometry have a crucial importance in the proposed process. Their effects are investigated on sample specimens.

Two approaches for simulating the heating process are proposed. In the preliminary studies, the heat generation is replaced by a constant heat flux on a limited area on the surface of the workpiece. The heat losses due to radiation and convection are taken into consideration by decreasing the heat flux during heating. This method is proved to be effective in certain cases since certain dimensions of the final product are close to the actual values. However, for some applications, unsatisfactory results are obtained. It is a very attractive method of simulation due to its simplicity; however, especially in cases, in which the skin depth is large, this approach may fail to reflect the actual case.

The improved simulation of the process, which regards the actual heat generation pattern, is successful. However, some errors are detected on the final dimension of the workpiece. The probable reasons of this situation are the assumptions about the thermal boundary conditions. In this case, the radiation effects, which are very dominant on the bulge area at the later stages of heating is discarded. Also, the convection coefficient is kept constant during the analysis. It is proved in Section 8.6.1 that the forming characteristics and the final shape of the workpiece are very sensitive to the temperature distribution around the bulge area. Therefore, neglecting the heat loss from the surface causes some errors.

Describing the process by using non dimensional parameters is beneficial to predict the temperature distribution of different materials without any calculation. Therefore, the heating process is formulated by using an ideal model of heating. The verification of the analytical equation is done by numerical calculations. However, for some materials deviation of the calculated result from the expected

result is observed. These are mainly related with the capability of the model to calculate the temperature on the surface area of the heated region. However, it is seen that the analytic model is adequate to provide comparison of different materials.

As a result, the author’s opinion is that the process is simulated successfully within some tolerance limits. The parameter investigation reflects the natural tendency of the process to changes in those parameters.

CHAPTER 9

DISCUSSIONS, CONCLUSIONS & FURTHER RECOMMENDATIONS

The aim of the study is to investigate the effects of local heating on the material flow during free forming and the final properties of the products. The material flow and the final shape of the products are investigated. The limits of the process, properties of the products, possible failure modes are presented. Axisymmetric cylindrical workpieces are used for investigation of the process.

The local heating and successive free forming process is analyzed by experimental studies and numerical calculations. The numerical calculations are carried out in accordance with the experiments and results are compared with the observations. The physics of deformation is analyzed and effects of certain parameters are determined by the computer simulations.

The temperature gradient within the workpiece created by local heating has a considerable effect on the material flow under compressive stress. In free forming applications, in which the workpiece has a constant temperature through its volume, the final shape is also axisymmetric, if there are no external effects that distort the shape of the product. Local heating, on the other hand, distorts the regular path of material flow in free forming. The high temperature portion of the material loses ability to resist the compressive forces and flows easier than the

lower temperature regions. In the solid specimens, around the heated region, the material itself acts as a barrier to the flow of soft material; therefore the material flow in this region is directed out of the surface of the cylinder and a local bulge is formed. On the hollow workpieces, a local bulge is formed on both sides of the heated wall, due to the absence of the material barrier. The secondary bulge on the inner wall of the hollow specimens is formed by in different ways. These are shown schematically in Figure 9.1 In some cases the heated volume of material compressed between the relatively cooler portions of the wall and flows in both directions from the very beginning of the process. The volume of material that flows in the two directions is proportional to the temperature gradient along the wall thickness. In the second case, the heated portion of the material is buckled under the compressive loads and bends in the beginning of the process. As the punch proceeds further, the heated wall folds on itself. Further height reduction causes formation of the secondary bulge. The buckling case is observed at relatively high temperatures. Folding of the side wall on itself may cause inclusion of some oxide layers within the local bulge.

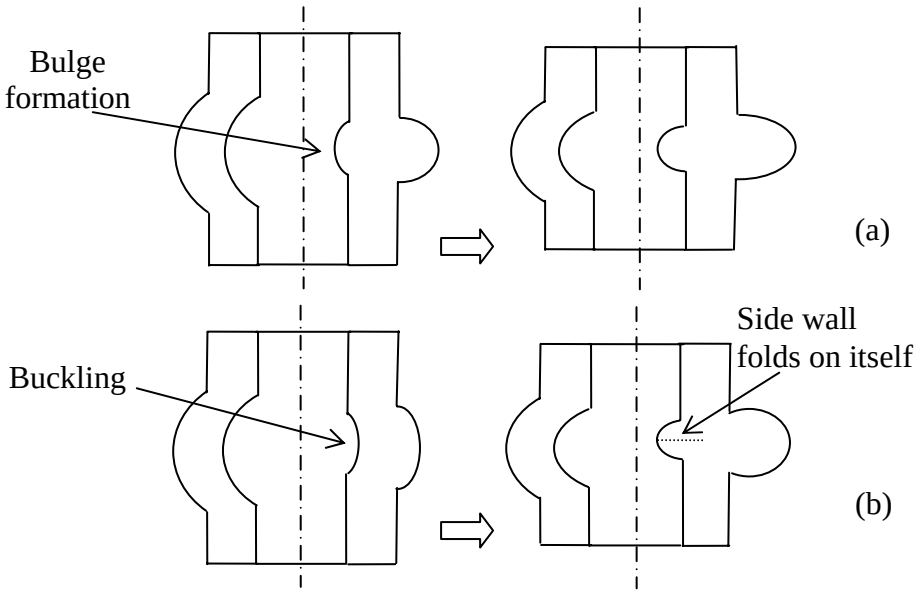

Figure 9.1 Schematic representation of bulge formation on hollow workpieces.

Two different methods for simulation of heating have been proposed in the study. In the first case, the heat generation within the workpiece is modeled as heat flux at the surface of the material that is applied on a certain region on the surface. The dominated effects of convection and radiation at elevated temperatures are simulated by decreasing the heat flux during heating. This method is simple and gives idea about the product of the process. However, in cases, where the skin depth of the workpiece is large and comparable to its dimensions, this technique gives poor results.

In the second method, the heat generation in the workpiece is calculated by electromagnetic calculations and the results are used in the thermo-mechanical analysis. In this process, the heat generation on the locations below the surface is taken into consideration. The results are satisfying, however some errors are observed. Regarding the sensitivity of the product shape on the temperature of the heated volume, it can be claimed that the errors are due to neglecting the radiation heat transfer and the enhanced convection at elevated temperatures. Assigning an average value as the convection coefficient may fail to reflect the actual temperature distribution. The author's opinion is that more accurate results can be obtained by careful analysis and effective simulation of the heat loss.

An assumption made in the simulation is the dependency of electrical resistivity and relative permeability on temperature. As the temperature is increase, the electrical resistivity also increases, which in turn effects the heat generation at a certain instant. The relative permeability of the materials has a similar effect. However, for X5CrNi18 9 and Ti6Al4V, it will have no effect since these are nonmagnetic and their relative permeability is unity. For 16MnCr5, the magnetic permeability changes with temperature and magnetic field. A more accurate simulation of heating can be achieved by carrying out a coupled electromagnetic-thermal analysis.

The effects of the process parameters are investigated by using the improved model, since the nature of the heating process is better reflected. Effects of the parameters on the bulge dimensions and the average surface temperature of the heated region are summarized in Table. 9.1. The tendency of the dimensional variations is investigated within the limitations of the experimental set up and available material. The effects of some parameters are not included in the table since a correlation is not clearly observed in the analyses.

Table 9.1 The relation between the process parameters and the temperature and bulge dimensions (D.P.: Directly proportional, I.P.: Inversely proportional).

		Avg. temperature on the heated surface	Width of the Local Bulge	Height of the Local Bulge
Heating	Coil Current	D.P.	D.P.	D.P
	Current Frequency	D.P	D.P.	D.P
	Heating Time	D.P	D.P.	D.P
Specimen Properties	Thermal Conductivity	I.P.	I.P.	D.P.
	Heat Capacity	D.P	D.P.	I.P.
	Wall Thickness	I.P.	-	-
Free Forming	Punch Speed	D.P	D.P.	-

The thermal properties of the workpiece material have a direct effect on the applicability of the process. The materials should be capable of preventing the heat diffusion within the workpiece and maintaining the high temperature gradients on the heated region during free forming. The thermal diffusivity of the material is the main parameter that effects heat diffusion. Materials with lower values of thermal diffusivity are more suitable for the process due to their superior ability in keeping the heat energy localized in a limited volume within the workpiece.

The main parameters of induction heating are the amplitude and frequency of the current in the coil. The heat generation rate within the workpiece is proportional to the value of square of the current magnitude. High current values are desirable in local heating, since required temperature values are obtained on the workpiece surface without leaving time for heat diffusion in the material. The numerical calculations have shown that the high frequency values are also desirable for free forming of locally heated specimens. Increase of frequency results in increase of the overall heat generation rate within the workpiece. Also, the majority of the total heat generation is concentrated on a narrower band below the surface of the workpiece. A higher temperature gradient can be created at high frequency values.

The punch speed is an important parameter that affects the final geometry of the products. The punch speed is the only parameter that determines the forming time. Since the spatial temperature pattern becomes homogeneous in time, low punch speed values are favorable for manufacturing local formations on the workpieces.

The workpieces with various dimensions are used in the study. Deformation characteristics of the hollow and solid specimens are investigated. Local bulge is obtained on all types of the workpieces. The other typical formation observed on the products is the barreled shape of the rear wall. Due to the localized temperature increase on the middle portion of the cylindrical specimens, this portion is weakened. The workpieces behave as a rod with a notch in place of the hot volume of material and buckles under the compressive load. The buckling behavior becomes more pronounced on the hollow geometries. The walls of the workpiece tend to fold on itself for low values of outer diameter to inner diameter ratio.

The buckling of the rear side of the specimens may be a problem in specific applications. Through the parameter study carried out by means of numerical calculations, it is observed that this type of formation cannot be eliminated for the workpiece geometries used in the analysis. An alternative method is to apply local heating in closed die forging operations. The material flow is restrained by means

of die and the desired product shapes can be achieved. In this case, the die costs may increase. The alteration in the process imposed by local heating is the reduced punch forces.

It is observed that the material flow in different materials show different characteristics if identical heating procedures are applied. The response of the material is determined by a set of material properties, which makes it hard to predict the behavior of other materials by using the available results of another material. Especially, the thermal properties have significant effect on the applicability of the process and the shape of the product, since the temperature distribution is one of the main parameter that enables local deformation. Therefore, it is useful to describe the heating process in terms of non dimensional parameters. In the analytical modeling, the heating pattern is idealized and differential equation is derived accordingly. The numerical verification of the method is done. Some deviations from the expected behavior are observed. These originate from the capability of the model to calculate the temperature on the surface area of the heated region. For 16MnCr5, which has a smaller skin depth in the process, the surface heat generation is underestimated due to the modeling assumptions. However, it is seen that the analytic model is able to provide a comparison between different materials and is useful in predicting the temperature distribution without numerical calculations. The model can be further improved by altering the numerical model, and including the effect of coil dimensions, workpiece dimensions and variable material properties.

As a result, the author’s opinion is that the study is adequate in analyzing the effects of local induction heating of the workpieces to free forming process. In this study, the probable effects of the parameters on the process are examined. The results and comments aim to give the reader an opinion and background information about free forming of locally induction heated specimens. This process idea is proposed to inspire the manufacturers and be modified for certain industrial applications.

REFERENCES

1. Tekkaya, A.E., *ME 453 Metal Forming Technology, Lecture Notes*. 2001: METU, Ankara.

2. Schuler Gmb, H., *Metal forming handbook*. 1998, Berlin ; London: Springer-Verlag. xx, 563 p.

3. Avitzur, B., *Handbook of metal-forming processes*. 1983, New York ; Chichester: Wiley. 1020p.

4. Avitzur, B., *Plastic working in the USA and related environmental issues.* Journal of Materials Processing Technology, 1996. **59**(3): p. 199-204.

5. Zlobina, M., S. Galunin, Y. Blinov, B. Nacke, A. Nikanorov, and H. Schülbe. *Numerical Modelling of Non-Linear Transverse Flux Heating Systems*. in *International Scientific Colloquium, Modelling for Electromagnetic Processing*. 2003.

6. Kim, W.B. and S.J. Na, *A Study on Residual-Stresses in Surface Hardening by High-Frequency Induction-Heating.* Surface & Coatings Technology, 1992. **52**(3): p. 281-288.

7. Yoshihara, S., H. Nishimura, H. Yamamoto, and K. Manabe, *Formability enhancement in magnesium alloy stamping using a local heating and cooling technique: circular cup deep drawing process.* Journal of Materials Processing Technology, 2003. **142**(3): p. 609-613.

8. Yu, G., K. Masubuchi, T. Maekawa, and N.M. Patrikalakis. *A Finite Element Model for Metal Forming by Laser Line Heating*. in *10th International*

Conference on Computer Applications in Shipbuilding, ICCAS '99. 1999. MIT, Cambridge: MIT Sea Grant Publication.

9. Hu, Z. and J.Q. Li, *Computer simulation of pipe-bending processes with small bending radius using local induction heating.* Journal of Materials Processing Technology, 1999. **91**(1-3): p. 75-79.

10. Merrygold, E. and F.H. Osman, *Forging of complex geometries with differential heating.* Journal of Materials Processing Technology, 1998. **80-1**: p. 179-183.

11. Kayatürk, K., A. Kurt, U. Weidig, K. Steinhoff, and A.E. Tekkaya. *Simultaneous Cold and Hot Forginig in a Single Forming Step - Principle, Possibilities and Limitations*. in *Slovenian Tool and Die Development Centre, 3rd International Conference on Industrial Tools.* 2001. Celje, Slovenia.

12. Kurt, A., *Simultaneous Hot and Cold Forging of Hollow Workpieces*, in *Department of Mechanical Engineering*. 2002, METU: Ankara. p. 163.

13. Erickson, C.J., *Handbook of electrical heating for industry*. 1995, New York: Institute of Electrical and Electronics Engineers. xxi, 629 p.

14. Rudnev, V., *Handbook of induction heating*. Manufacturing engineering and materials processing ; 61. 2003, New York: Marcel Dekker. xi, 777 p.

15. Cheng, D.K., *Fundamentals of engineering electromagnetics*. 1993, Reading, Mass.: Addison-Wesley Pub. Co. xv, 488 p.

16. Kraus, J.D., *Electromagnetics*. 4th ed. McGraw-Hill series in electrical engineering. Electromagnetics. 1992, New York: McGraw-Hill. xix, 847 p.

17. Callister, W.D., *Materials Science and Engineering : An Introduction*. 5th ed. 2000, New York: Wiley. xxi, 871 p.

18. Tekkaya, A.E., *ME 413 Introduction to Finite Element Analysis, Lecture Notes*. 2002.

19. Cook, R.D., *Concepts and applications of finite element analysis; a treatment of the finite element method as used for the analysis of displacement, strain, and stress*. 1974, New York,: Wiley. xvii, 402 p.

20. *MSC.Marc User Guide Volume A: Theory and User Information*.

21. Belytschko, T., W.K. Liu, and u, *Nonlinear finite elements for continua and structures*. 2000, Chichester ; New York: John Wiley. xvi, 650 p.

22. Tekkaya, A.E., *ME 581 Finite Element Analysis in Solid Mechanics, Lecture Notes*. 2003.

23. *Electromagnetic Field Analysis Guide*, in *ANSYS 7.0 Documentation*.

24. *Kottonau Pyrometrie, User's Manual*.

25. Material Specification Sheet: Saarstahl - 16MnCr5 *Retrived* 16.07.2004, *from* Saarstahl AG Web site: http://www.saarstahl.com/english/produkte/walzstahlsorten/PDFDokumente/7131_7139_16MnCr5_16MnCrS5.pdf

26. Steel Specs: Special, 16MnCr5, *Retrived* 16.07.2004, *from* UNSCO Web site: http://www.unsco.com/steel_specs/steel_spec_special_16MnCr5.htm

27. AISI Type 304 Stainless Steel, *Retrived* 03.12.2004, *from* MATWEB, Material Property Data Web site: http://www.matweb.com/SpecificMaterial.asp?bassnum=Q304A

28. Boyer, R.R., E.W. Collings, G. Welsch, and A.S.M. International, *Titanium alloys*. Materials properties handbook. 1994, Materials Park, Ohio: ASM International. xxii, 1176p.

29. Incropera Frank, P. and P. DeWitt David, *Fundamentals of heat and mass transfer*. 4th ed ed. 1996, New York ; Chichester: Wiley. xxiii, 886 p.

30. Hardenability of Steel, *Retrived* 28.01.2005, *from* Department of Materials Science and Metallurgy, University of Cambridge Web site: http://www.msm.cam.ac.uk/phase-trans/2000/practicals/AP3/AP3.html

31. Hot Rolling Strip Steels, *Retrived* 23.01.2005, *from* MATTER, Non-profit Consortium of UK Materials Science Departments Web site: http://www.matter.org.uk/steelmatter/forming/4_5.html

32. Keskin, İ. *Dünya Metal Standartları*. 1986, Ankara: On.Ar Ltd.

33. Topbaş, M.A., *Çelik ve Isıl İşlem El Kitabı*. 1998, İstanbul: Prestij Yayıncılık Basım Hizmetleri.

34. MMAT380 Lecture Notes, *Retrived* 28.01.2005, *from* The University of British Columbia, Metals & Materials Engineering Web site: http://www.mmat.ubc.ca/courses/mmat380/lectures/2004/Lecture%2018-Titanium(Complete).pdf

35. Chaboudez, C., S. Clain, R. Glardon, D. Mari, J. Rappaz, and M. Swierkosz, *Numerical modeling in induction heating for axisymmetric geometries.* IEEE Transactions on Magnetics, 1997. **33**(1): p. 739-745.

36. Sadeghipour, K., J.A. Dopkin, and K. Li, *A computer aided finite element experimental analysis of induction heating process of steel.* Computers in Industry, 1996. **28**(3): p. 195-205.

37. Steel EC80, *Retrived* 18.02.2005, *from* Metal Ravne Web site: http://www.sz-metal.si/selector/steels/EC80.html

38. Titanium Ti-6Al-4V (Grade 5) STA, *Retrived* 12.06.2003, *from* MATWEB, Material Property Data Web site: http://www.matweb.com/search/ Specific Material.asp?bassnum=MTP642

APPENDIX A

Table A.1 Summary of the experiments

No	Name	Induction Heating						Workpiece			Process	Result
		MF	Gear Ratio	Freq. (kHz)	Power (kW)	Max. T. (C)	Time (s)	Material	Do (mm)	Di (mm)	Length Ratio	
1	Exp 19	7	11:01	7.8	38	1303	15	Ti6Al4V	30	-	0.5	S
2	Exp 20	5	11:01	7.8	18	985	322	X5CrNi18 9	30	-	0.5	S
3	Exp 21	6	11:01	7.8	28	1050	98	X5CrNi18 9	30	-	0.5	S
4	Exp 22	7	11:01	7.8	40	1102	54	X5CrNi18 9	30	-	0.5	S
5	Exp 23	6	11:01	7.8	28	913	70	X5CrNi18 9	30	-	0.5	S
6	Exp 24	7	11:01	7.8	40	934	31	X5CrNi18 9	30	-	0.5	S
7	Exp 26	6	11:01	7.8	28	1119	27	X5CrNi18 9	30	22	0.5	CS
8	Exp 27	7	11:01	7.8	40	1092	12	X5CrNi18 9	30	22	0.5	CS
9	Exp 28	7	11:01	7.8	40	929	16	X5CrNi18 9	30	22	0.5	P
10	Exp 29	6	11:01	7.8	28	949	14	X5CrNi18 9	30	22	0.5	NP
11	Exp 30	7	11:01	7.8	40	948	18	X5CrNi18 9	30	22	0.5	P
12	Exp 32	7	11:01	7.8	40	961	11	X5CrNi18 9	30	22	0.5	P, CS
13	Exp 33	5	11:01	7.8	18	1097	97	X5CrNi18 9	30	20	0.5	S
14	Exp 34	6	11:01	7.8	28	1103	47	X5CrNi18 9	30	20	0.5	P
15	Exp 35	7	11:01	7.8	40	1107	20	X5CrNi18 9	30	20	0.5	P, CS
16	Exp 36	5	11:01	7.8	18	1081	127	X5CrNi18 9	30	18	0.5	P, CS
17	Exp 37	6	11:01	7.8	28	1107	46	X5CrNi18 9	30	18	0.5	P, CS
18	Exp 38	7	11:01	7.8	40	1103	36	X5CrNi18 9	30	18	0.5	P, CS
19	Exp 39	5	11:01	7.8	18	1050	193	X5CrNi18 9	30	16	0.5	CS, A
20	Exp 40	6	11:01	7.8	28	1102	58	X5CrNi18 9	30	16	0.5	P
21	Exp 41	7	11:01	7.8	40	1106	37	X5CrNi18 9	30	16	0.5	P,CS
22	Exp 42	6	11:01	7.8	28	1105	48	X5CrNi18 9	30	18	0.5	P,CS
23	Exp 43	7	11:01	7.8	40	1116	23	X5CrNi18 9	30	18	0.5	P,CS
24	Exp 44	6	11:01	7.8	28	1105	39	X5CrNi18 9	30	20	0.5	P
25	Exp 46	6	11:01	7.8	28	1103	58	X5CrNi18 9	30	16	0.5	S, P
26	Exp 47	7	11:01	7.8	40	1111	30	X5CrNi18 9	30	16	0.5	S
27	Exp 48	7	11:01	7.8	40	919	20	X5CrNi18 9	30	16	0.5	S, P
28	Exp 50	7	11:01	7.8	40	931	13	X5CrNi18 9	30	20	0.5	S

Table A.1 Summary of the experiments (Continued)

No	Name	Induction Heating						Workpiece			Process	Result
		MF	Gear Ratio	Freq. (kHz)	Power (kW)	Max. T. (C)	Time (s)	Material	Do (mm)	Di (mm)	Length Ratio	
29	Exp 51	6	11:01	7.8	28	1101	143	X5CrNi18 9	30	-	0.75	A
30	Exp 52	7	11:01	7.8	40	1104	68	X5CrNi18 9	30	-	0.75	S
31	Exp 53	7	11:01	7.8	40	1108	25	X5CrNi18 9	30	16	0.75	S
32	Exp 54	7	11:01	7.8	40	1114	19	X5CrNi18 9	30	18	0.75	S
33	Exp 55	6	11:01	7.8	28	1104	34	X5CrNi18 9	30	18	0.75	S
34	Exp 56	6.5	11:01	7.8	33	1113	26	X5CrNi18 9	30	18	0.75	S, CS
35	Exp 57	6	11:01	7.8	28	1108	30	X5CrNi18 9	30	20	0.75	CS
36	Exp 58	6	11:01	7.8	28	1108	29	X5CrNi18 9	30	20	0.75	S, CS
37	Exp 59	6	11:01	7.8	28	1113	24	X5CrNi18 9	30	22	0.75	S, CS
38	Exp 60	6	11:01	7.8	28	1102	59	X5CrNi18 9	30	16	0.75	S
39	Exp 61	7	11:01	7.8	40	1205	47	Ti6Al4V	30	-	0.75	A
40	Exp 62	7	11:01	7.8	40	1009	23	Ti6Al4V	30	-	0.75	S
41	Exp 63	7	11:01	7.8	40	861	18	Ti6Al4V	30	-	0.75	S
42	Exp 64	7	11:01	7.8	40	907	49	X5CrNi18 9	30	-	0.75	S
43	Exp 65	7	11:01	7.8	40	928	16	X5CrNi18 9	30	18	0.75	S
44	Exp 67	7	11:01	7.8	40	926	10	X5CrNi18 9	30	22	0.75	S
45	Exp 68	7	11:01	7.8	40	931	18	X5CrNi18 9	30	20	0.75	S
46	Exp 69	6	11:01	7.8	28	911	27	X5CrNi18 9	30	18	0.75	S
47	Exp 73	6	11:01	7.8	28	1003	46	X5CrNi18 9	41	-	0.5	S, NP
48	Exp 74	7	11:01	7.8	40	1004	61	X5CrNi18 9	41	-	0.5	S, NP
49	Exp 75	7	11:01	7.8	40	1106	37	X5CrNi18 9	51	-	0.5	NP
50	Exp 76	6.5	11:01	7.8	33	1103	62	X5CrNi18 9	51	-	0.5	NP
51	Exp 77	5.5	11:01	7.8	23	1052	64	X5CrNi18 9	51	-	0.5	NP
52	Exp 79	6	11:01	7.8	28	1002	120	16MnCr5	30	-	0.75	A
53	Exp 80	7	11:01	7.8	40	1010	70	16MnCr5	30	-	0.75	A
54	Exp 81	7	11:01	7.8	40	906	27	16MnCr5	30	-	0.75	S
55	Exp 82	7	11:01	7.8	40	810	21	16MnCr5	30	-	0.75	S
56	Exp 83	7	11:01	7.8	40	714	13	16MnCr5	30	-	0.75	S
57	Exp 84	7	11:01	7.8	40	716	12	16MnCr5	30	-	0.75	S
58	Exp 85	5	11:01	7.8	18	1075	109	16MnCr5	30	-	0.75	
59	Exp 86	6	11:01	7.8	28	1106	22	16MnCr5	30	-	0.75	CS
62	Exp 91	7	11:01	7.8	40	820	10	16MnCr5	30	-	0.75	CW
63	Exp 92	7	11:01	7.8	40	827	10	16MnCr5	30	-	0.75	
64	Exp 93	6	07:01	10.5	33	902	36	16MnCr5	30	-	0.75	A
65	Exp 94	5	07:01	10.5	22	850	186	16MnCr5	30	-	0.75	A
66	Exp 95	5	09:01	8.5	22	902	93	16MnCr5	30	-	0.75	A
67	Exp 99	6	11:01	7.8	28	1108	25	X5CrNi18 9	40	29	0.75	S,CS
68	Exp 100	6	11:01	7.8	28	919	13	X5CrNi18 9	40	29	0.75	S
69	Exp 101	7	11:01	7.8	40	1032	21	X5CrNi18 9	40	29	0.75	S

Table A.1 Summary of the experiments (Continued)

No	Name	Induction Heating						Workpiece			Process	Result
		MF	Gear Ratio	Freq. (kHz)	Power (kW)	Max. T. (C)	Time (s)	Material	Do (mm)	Di (mm)	Length Ratio	
70	Exp 102	6	11:01	7.8	28	1106	34	X5CrNi18 9	40	27	0.75	NP
71	Exp 103	6	11:01	7.8	28	1100	44	X5CrNi18 9	40	27	0.75	S
72	Exp 104	6	11:01	7.8	28	1103	62	X5CrNi18 9	40	24	0.75	S
73	Exp 105	6	11:01	7.8	28	1060	84	X5CrNi18 9	40	21	0.75	S
74	Exp 106	7	11:01	7.8	40	1108	30	X5CrNi18 9	40	21	0.75	S
75	Exp 107	7	11:01	7.8	40	1104	46	X5CrNi18 9	40	24	0.75	S
76	Exp 108	7	11:01	7.8	40	918	30	X5CrNi18 9	40	27	0.75	S
77	Exp 109	6	11:01	7.8	28	1106	37	X5CrNi18 9	50	37	0.75	S, P
78	Exp 110	6	11:01	7.8	28	1102	76	X5CrNi18 9	50	33	0.75	S, P
79	Exp 111	6	11:01	7.8	28	1100	72	X5CrNi18 9	50	30	0.75	S, P
80	Exp 112	6	11:01	7.8	28	1026	112	X5CrNi18 9	50	27	0.75	S
81	Exp 113	6	11:01	7.8	28	1105	39	X5CrNi18 9	60	44	0.75	S, NP
82	Exp 114	6	11:01	7.8	28	1104	54	X5CrNi18 9	60	40	0.75	S, NP
83	Exp 115	6	11:01	7.8	28	1101	107	X5CrNi18 9	60	36	0.75	NP
84	Exp 116	6	11:01	7.8	28	1001	85	X5CrNi18 9	60	32	0.75	NP
85	Exp 120	5	11:01	7.8	18	1103	68	16MnCr5	30	22	0.66	A
86	Exp 121	6	11:01	7.8	28	1105	32	16MnCr5	30	22	0.66	A, P
87	Exp 122	7	11:01	7.8	40	1123	17	16MnCr5	30	22	0.66	CS, P
88	Exp 123	6	11:01	7.8	28	922	20	16MnCr5	30	22	0.66	
89	Exp 124	7	11:01	7.8	40	943	10	16MnCr5	30	22	0.66	
90	Exp 125	5	11:01	7.8	18	1150	125	16MnCr5	30	18	0.66	S
91	Exp 126	6	11:01	7.8	28	1102	45	16MnCr5	30	18	0.66	S
92	Exp 127	7	11:01	7.8	40	1110	26	16MnCr5	30	18	0.66	S
93	Exp 128	6	11:01	7.8	28	1106	42	16MnCr5	30	18	0.75	S
94	Exp 129	7	11:01	7.8	40	1113	24	16MnCr5	30	18	0.75	S
95	Exp 130	6	11:01	7.8	28	909	23	16MnCr5	30	18	0.75	S
96	Exp 131	7	11:01	7.8	40	920	17	16MnCr5	30	18	0.75	S
97	Exp 132	6	11:01	7.8	28	1102	63	16MnCr5	30	16	0.75	S
98	Exp 133	5	11:01	7.8	18	1001	152	16MnCr5	30	16	0.75	S
99	Exp 134	7	11:01	7.8	40	1105	32	16MnCr5	30	16	0.75	S
100	Exp 135	6	11:01	7.8	28	909	32	16MnCr5	30	16	0.75	S
101	Exp 136	7	11:01	7.8	40	914	18	16MnCr5	30	16	0.75	S
102	Exp 137	7	11:01	7.8	40	815	15	16MnCr5	30	16	0.75	S
103	Exp 138	6	07:01	10.5	33	915	19	16MnCr5	30	16	0.75	S
104	Exp 139	7	07:01	10.5	41	925	11	16MnCr5	30	16	0.75	S
105	Exp 140	7	07:01	10.5	41	871	9	Ti6Al4V	30	-	0.75	S, IC
106	Exp 141	7	07:01	10.5	41	867	9	Ti6Al4V	30	-	0.75	S, IC
107	Exp 142	7	11:01	7.8	40	909	18	16MnCr5	30	-	0.75	S
108	Exp 143	7	11:01	7.8	40	907	18	16MnCr5	30	-	0.66	S

Table A.1 Summary of the experiments (Continued)

No	Name	Induction Heating						Workpiece			Process	Result
		MF	Gear Ratio	Freq. (kHz)	Power (kW)	Max. T. (C)	Time (s)	Material	Do (mm)	Di (mm)	Length Ratio	
109	Exp 144	7	11:01	7.8	40	911	30	X5CrNi18 9	30	-	0.75	S
110	Exp 146	7	11:01	7.8	40	876	16	Ti6Al4V	30	-	0.75	
111	Exp 147	7	11:01	7.8	40	1023	17	Ti6Al4V	30	-	0.75	S
112	Exp 148	7	11:01	7.8	40	1200	28	Ti6Al4V	30	-	0.75	
113	Exp 151	6	11:01	7.8	28	1108	16	16MnCr5	40	29	0.75	S
114	Exp 152	7	11:01	7.8	40	1116	11	16MnCr5	40	29	0.75	S
115	Exp 153	6	11:01	7.8	28	916	12	16MnCr5	40	29	0.75	S
116	Exp 154	7	11:01	7.8	40	921	7	16MnCr5	40	29	0.75	S
117	Exp 156	6	11:01	7.8	28	1109	25	16MnCr5	40	27	0.75	S
118	Exp 157	7	11:01	7.8	40	1133	11	16MnCr5	40	27	0.75	
119	Exp 158	6	11:01	7.8	28	900	12	16MnCr5	40	27	0.75	S, P
120	Exp 159	7	11:01	7.8	40	938	7	16MnCr5	40	27	0.75	S, P
121	Exp 160	6	11:01	7.8	28	1106	29	16MnCr5	40	24	0.75	S, P
122	Exp 161	7	11:01	7.8	40	1113	16	16MnCr5	40	24	0.75	S, P
123	Exp 162	6	11:01	7.8	28	908	16	16MnCr5	40	24	0.75	S, P
124	Exp 163	7	11:01	7.8	40	925	8	16MnCr5	40	24	0.75	S
125	Exp 164	6	11:01	7.8	28	1107	29	16MnCr5	40	24	7/8	S
126	Exp 165	6	11:01	7.8	28	1100	37	16MnCr5	40	21	0.75	S
127	Exp 166	7	11:01	7.8	40	1109	16	16MnCr5	40	21	0.75	S
128	Exp 167	6	11:01	7.8	28	910	17	16MnCr5	40	21	0.75	NS
129	Exp 168	7	11:01	7.8	40	934	10	16MnCr5	40	21	0.75	NS
130	Exp 172	7	11:01	7.8	40	1128	15	16MnCr5	50	37	0.75	S, P
131	Exp 174	7	11:01	7.8	40	922	12	16MnCr5	50	37	0.75	S, P
132	Exp 175	6	11:01	7.8	28	1104	61	16MnCr5	50	33	0.75	S, P
133	Exp 176	7	11:01	7.8	40	1114	24	16MnCr5	50	33	0.75	S
134	Exp 177	6	11:01	7.8	28	913	29	16MnCr5	50	33	0.75	S
135	Exp 178	7	11:01	7.8	40	921	13	16MnCr5	50	33	0.75	S, P
136	Exp 179	6	11:01	7.8	28	1103	65	16MnCr5	50	30	0.75	S, P
137	Exp 180	7	11:01	7.8	40	1107	27	16MnCr5	50	30	0.75	S, P
138	Exp 181	6	11:01	7.8	28	910	23	16MnCr5	50	30	0.75	NS
139	Exp 182	7	11:01	7.8	40	924	13	16MnCr5	50	30	0.75	S
140	Exp 183	6	07:01	10.5	33	1200	46	16MnCr5	50	30	0.75	S
141	Exp 184	6.5	07:01	10.5		1015	13	16MnCr5	50	27	0.75	S
142	Exp 185	6	11:01	7.8	28	1103	79	16MnCr5	50	27	0.75	S
143	Exp 186	7	11:01	7.8	40	1106	29	16MnCr5	50	27	0.75	S
144	Exp 187	6	11:01	7.8	28	906	29	16MnCr5	50	27	0.75	S
145	Exp 188	7	11:01	7.8	40	915	15	16MnCr5	50	27	0.75	S
146	Exp 189	6	07:01	10.5	33	1111	24	X5CrNi18 9	50	37	0.75	CS
147	Exp 190	6	07:01	10.5	33	1113	29	X5CrNi18 9	50	33	0.75	S

Table A.1 Summary of the experiments (Continued)

No	Name	Induction Heating						Workpiece			Process	Result
		MF	Gear Ratio	Freq. (kHz)	Power (kW)	Max. T. (C)	Time (s)	Material	Do (mm)	Di (mm)	Length Ratio	
148	Exp 191	6	07:01	10.5	33	1105	37	X5CrNi18 9	50	30	0.75	S
149	Exp 192	6	07:01	10.5	33	1107	42	X5CrNi18 9	50	27	0.75	S
150	Exp 194	6	09:01	8.6	21	1113	24	X5CrNi18 9	50	27	0.75	S
151	Exp 195	6	11:01	7.8	28	1132	33	16MnCr5	60	44	0.75	NP
152	Exp 196	6	11:01	7.8	28	1104	52	16MnCr5	60	40	0.75	NP,P
153	Exp 197	7	11:01	7.8	40	1100	1	16MnCr5	60	40	0.75	NP,P
154	Exp 198	6	11:01	7.8	28	900	1	16MnCr5	60	40	0.75	NP
155	Exp 199	7	11:01	7.8	40	900	16	16MnCr5	60	40	0.75	NP,P
156	Exp 200	7	11:01	7.8	40	1100	22	16MnCr5	60	44	0.75	NP,P
157	Exp 201	6	11:01	7.8	28	900	22	16MnCr5	60	44	0.75	NP,P
158	Exp 202	7	11:01	7.8	40	900	13	16MnCr5	60	44	0.75	NP,P
159	Exp 203	6	07:01	10.5	33	1000	23	16MnCr5	60	40	0.75	NP,P
160	Exp 204	6	07:01	10.5	33	1000	19	16MnCr5	60	44	0.75	NP
161	Exp 205	6	07:01	10.5	33	1000	20	16MnCr5	60	44	0.75	NP
162	Exp 206	6	07:01	10.5	33	1000	28	X5CrNi18 9	50	-	0.75	S
163	Exp 209	6.5	11:01	7.8	33	900	9	16MnCr5	30	22	0.75	S, P
164	Exp 210	6.5	11:01	7.8	33	900	11	16MnCr5	30	20	0.75	S
165	Exp 211	6.5	11:01	7.8	33	900	13	16MnCr5	30	18	0.75	S
166	Exp 212	6.5	11:01	7.8	33	900	13	16MnCr5	30	16	0.75	S
167	Exp 213	6.5	11:01	7.8	33	700	7	16MnCr5	30	22	0.75	S
168	Exp 214	6.5	11:01	7.8	33	700	8	16MnCr5	30	16	0.75	S, P

A : The bulge on the mid portion is axisymmetric.

CS : Crack on surface.

IC : Internal crack.

S : Satisfactory (A local bulge is obtained).

NP : The specimen is either not pressed or the punch speed is not constant in the process due to insufficient press force.

NS : Not satisfactory (Heaing conditions are insufficient to induce local bulge formation).

P : The workpiece walls penetrate into the local bulge.